Laura Resch, Dipl.-Ing., BSc

Atomic Defects and Processes in Structurally Complex Materials studied by Positron Annihilation Techniques

DOCTORAL THESIS

to achieve the university degree of
Doktorin der technischen Wissenschaften

submitted to

Graz University of Technology

Supervisor

Assoc.Prof. Dipl.-Phys. Dr.rer.nat., Wolfgang Sprengel
Institute of Materials Physics

Graz, September 2020

Abstract

Positron annihilation in a material is highly sensitive to all kinds of open volume defects and in some cases even to impurities in a crystal lattice. This makes techniques of positron annihilation spectroscopy an ideal tool for the study of atomic defects and processes in structurally complex materials, such as, e.g., different metallic alloy systems.

Within this work, the process of age hardening at elevated temperatures (artificial aging) of Al–Mg–Si alloys has been investigated in detail utilizing positron annihilation techniques. Despite its great relevance for applications, the formation of precipitates underlying the mechanism of age hardening is not yet fully understood. For a comprehensive study of the atomistic processes occurring during the whole precipitation sequence, three different techniques of positron annihilation spectroscopy have been applied: 1) *ex situ* positron annihilation lifetime spectroscopy 2) *ex situ* temperature-dependent positron lifetime spectroscopy and 3) *in situ* Doppler broadening spectroscopy. The variation of the positron lifetime depending on the artificial aging time revealed three main steps of the precipitation process, including initial clustering in the first seconds of aging up to the formation of semi-coherent precipitates after days of aging. By temperature-dependent positron lifetime spectroscopy the individual stages of precipitates could be distinguished with regard to their positron trapping behaviour. Furthermore, *in situ* Doppler broadening spectroscopy increased the measurement accuracy but also added another aspect to the interpretation of the previously measured positron lifetime data due to the different trapping behaviour of positrons at the applied high measurement temperatures.

These experimental results were extended by setting up and solving a diffusion-reaction model for positron trapping and annihilation at spherical and cylindrical extended defects. The solutions obtained were closed-form expressions for the major positron annihilation parameters, which were applied to the trapping and annihilation of positrons at precipitates occuring during age hardening.

In the new material class of concentrated solid-solution alloys, the concentration of quenched-in thermal vacancies was determined by positron annihilation lifetime spectroscopy measurements after quenching the samples from temperatures close to their onset of melting. Whereas alloys with three constituents in non-equimolar fractions (CrFeNi) and face-centered cubic (fcc) crystal structure exhibit vacancy concentrations of about 10^{-5}, the lifetime spectra of the four and five component fcc concentrated solid-solution alloys (CoCrFeNi, CoCrFeMnNi, AlCoCrFeNi) did not show a vacancy-specific positron lifetime. Hence, there is either a vanishingly small amount ($<10^{-6}$) of vacancies being generated at temperatures close to the onset of melting, or the generated vacancies are inherently unstable. However, both of these indications are completely unexpected for any ductile metallic material.

Kurzfassung

Positronen eignen sich zur Detektion jeglicher Art von Defekten, die freies offenes Volumen beinhalten; unter bestimmten Voraussetzungen kann man mit Hilfe von Positronen sogar Fremdatome im Kristallgitter detektieren. Die Methode der Positronen-Annihilations-Spektroskopie kann daher sehr zielführend eingesetzt werden, um atomare Defekte und Prozesse in strukturell komplexen Materialien, wie z.B. verschiedenen metallischen Legierungssystemen, zu untersuchen.

Im Rahmen dieser Dissertation wurde die sogenannte Warmauslagerung zur Härtung von Al–Mg–Si Legierungen mit Hilfe unterschiedlicher Methoden der Positronen-Annihilations-Spektroskopie im Detail untersucht. Obwohl die Technik der Warmauslagerung enorm relevant für verschiedenste Anwendungen ist, ist die zugrunde liegende Entstehung von Ausscheidungen in der Al Matrix noch nicht vollständig erforscht. Um die gesamte Sequenz unterschiedlicher Ausscheidungen und die damit verknüpften atomaren Prozesse umfassend zu untersuchen wurden drei verschiedene Methoden der Positronen-Annihilations-Spektroskopie angewandt: 1) *Ex situ* Positronen-Annihilations-Lebensdauer-Spektroskopie 2) temperaturabhängige *ex situ* Positronen-Annihilations-Lebensdauer-Spektroskopie 3) *In situ* Positronen-Dopplerverbreiterungsspektroskopie. Durch die Variation der Positronenlebensdauer in Abhängigkeit von der Zeit der Warmauslagerung konnte die Ausscheidungssequenz zeitlich in drei Schritte unterteilt werden. Diese umfassen die erste Clusterbildung von Atomen innerhalb der ersten Sekunden bis hin zur Bildung der semi-kohärenten Ausscheidungen nach einigen Tagen der Warmauslagerung. Durch die temperaturabhängigen *ex situ* Messungen der Positronenlebensdauer konnten außerdem verschiedene Phasen in

der Ausscheidungssequenz anhand eines veränderlichen Verhaltens beim Positroneneinfang unterschieden werden. Des Weiteren konnte durch die Anwendung von *in situ* Dopplerverbreiterungsspektroskopie nicht nur die Messgenauigkeit erhöht werden, sondern durch das veränderte Einfangverhalten von Positronen in Defekte bei den angewandten hohen Temperaturen während der Messung auch weitere Aspekte zur Interpretation der Daten erlangt werden.

In Erweiterung zu den experimentellen Ergebnissen dieser Arbeit wurde außerdem ein theoretisches Diffusions-Reaktions Modell für Einfang und Zerstrahlung von Positronen an ausgedehnten sphärischen oder zylindrischen Defekten aufgestellt und gelöst. Die Lösungen dieses Modells sind analytische Ausdrücke der wichtigsten Positronen-Annihilations-Parameter und wurden auf den Einfang und die Annihilation von Positronen in Ausscheidungen, die während der Warmauslagerung entstehen, angewandt.

In der neuen Materialklasse der sogenannten Hoch-Entropie Legierungen wurde die Konzentration der thermisch generierten Leerstellen mit Hilfe der Positronen-Annihilations-Lebensdauer-Spektroskopie bestimmt, nachdem die Proben von Temperaturen nahe ihres Schmelzpunkts rasch abgeschreckt wurden. Dabei wurde in Legierungen mit drei Komponenten in nicht-equimolaren Anteilen (CrFeNi) und kubisch-flächenzentrierter (kfz) Kristalstruktur eine Leerstellenkonzentration im Bereich 10^{-5} festgestellt. Die Lebensdauerspektren der vier- und fünfkomponentigen kfz Legierungen (CoCrFeNi, CoCrFeMnNi, AlCoCrFeNi) hingegen, zeigten keine leerstellenspezifische Lebensdauer. Folglich entsteht in den vier- und fünfkomponentigen Legierungen bei Temperaturen nahe des Schmelzpunkts entweder nur ein vernachlässigbarer Anteil an Leerstellen ($<10^{-6}$), oder die thermisch erzeugten Leerstellen sind inherent instabil, beides ist für ein duktiles, metallisches Material höchst ungewöhnlich.

Table of Contents

1 | Introduction

The characterization of atomic defects and atomistic processes in structurally complex materials plays a major role for the definition, prediction and manipulation of important material properties. The concentration of dislocations in a pure metal or the concentration of precipitates in an alloy, for example, can influence the hardness and plasticity of materials; the formation and migration of vacancies is related to bulk diffusion and the radiation tolerance of a material.

Positrons, being attracted to all kinds of open volume defects and in some cases even to impurities in a crystal lattice, are a sensitive and specific probe for the investigation of the above-mentioned effects [1]. As a highly mobile particle, the positron diffuses through the crystal lattice and searches for defects which can eventually capture it. When the positron annihilates within such a trap, information about the type of trap, but also about its concentration in the crystal lattice can be obtained from the positron-electron annihilation γ-rays. In this thesis, different techniques of positron annihilation spectroscopy have been applied to extensively study the atomistic processes occurring during age hardening of commercial aluminium (Al) alloys. Furthermore, the method has been applied to tackle a fundamental question concerning the rather new alloy type of concentrated solid-solution alloys, namely whether and to what extent vacancies can be thermally generated in these alloys.

The term 'age hardening' refers to the growth of a sequence of precipitates in the Al

matrix during prolonged storage at room temperature or at elevated temperatures. Precipitates serve to harden the material by hindering dislocation movement, which makes the process of age hardening industrially important. For the case of Al–Mg–Si alloys, which are investigated in this thesis, there is a generally agreed model of the precipitation sequence [2], but there are still open questions left. Especially the early clustering stages are difficult to access experimentally, hence the exact atomistic processes defining their growth and transformation into precipitates, which are later determinant for the hardening response, are not known with certainty. Furthermore, the whole precipitation sequence is a continuous process heavily influenced by previously applied heat treatments and the exact alloy compositions, which complicates a comprehensive study of this process especially for industrially applied, commercial Al alloys.

The experimental method of positron annihilation spectroscopy has already proven to be highly suitable for the study of the whole precipitation sequence in Al alloys [3]. Positrons are sensitive to vacancies, which are essential in the first clustering phases and during the whole process for the transport of solute atoms. Furthermore, the matrix-precipitate interfaces can act as attractive potential for positrons as they include misfit defects with open volumes. Additionally, positrons can be trapped in the bulk of precipitates, even if they do not include open volume defects, due to an increased positron affinity of the solute elements being typically used in Al alloys compared to the Al matrix [4, 5]. Already existing studies concerning the age hardening of light weight alloys mainly include results concerning precipitates occurring during room temperature storage (see, e.g., refs. [6,7]). The study of artificial aging applying positron annihilation spectroscopy is experimentally more complicated. During the long data acquisition times when using conventional laboratory sources, the samples are exposed to secondary natural aging. Hence, such results are only valid for artificial aging superimposed with natural aging, which makes it even more complicated to gather valuable information about the artificial aging process explicitly, in particular concerning the early clustering stages.

For the investigation of the atomistic processes in the Al–Mg–Si alloy during artificial aging explicitly, in this thesis, three different positron annihilation techniques have been applied: 1) *Ex situ* positron annihilation lifetime spectroscopy, 2) *ex situ* temperature-dependent lifetime spectroscopy and 3) *in situ* Doppler broadening spectroscopy. The results of the *ex situ* positron annihilation lifetime study are presented in section 4.1.1 and in ref. [8]. Samples of a commercial Al–Mg–Si alloy were individually prepared in well-defined artificial aging states and kept at low temperatures during the time of the spectra acquisition to prevent secondary natural aging. By comparing the variation of the positron lifetime to *in situ* high-precision dilatometry measurements during artificial aging, the precipitation sequence could be divided into three main steps. Furthermore, the application of temperature-dependent positron annihilation lifetime spectroscopy (see section 4.1.2, ref. [9]) showed that different stages of precipitates vary in their positron trapping behaviour. Clusters and small precipitates, occurring in the early stages of artificial aging, only weakly bind positrons and allow thermal detrapping. Larger precipitates, appearing after longer aging times, show higher positron binding energies and do not allow thermal detrapping anymore. The application of *in situ* Doppler broadening spectroscopy (see 4.1.3, [10]) did not only increase the measurement accuracy but also added another aspect to the interpretation of the previously measured positron lifetime data during artificial aging. The high temperatures applied during the measurement affect positron trapping in such a way that positrons annihilate predominantly in traps with high binding energies. In section 4.3 [11,12] an exact solution of a diffusion-reaction model for the trapping and annihilation of positrons at spherical extended defects is presented. This model can be expanded for positron trapping and annihilation at spherical or cylindrical precipitates and complements previous experimental studies presented in this thesis.

Besides light weight alloys which fulfill the typical conventional alloying scheme of a base element with minor additions of different solute elements, also a completely different, new class of alloys has been studied in this thesis. So-called concentrated solid-solution alloys, also referred to as high-entropy alloys, consist of multiple base elements in equimolar

fractions. Certain concentrated solid-solution alloys show desirable material properties such as high strength and ductility at high temperatures [13, 14] but also enhanced resistance to radiation [15, 16]. For the understanding of these properties the formation and migration behaviour of vacancies at high temperatures could play an important role. This aspect was considered in this thesis (see section 4.2, ref. [17]) as the concentration of thermally induced, quenched-in vacancies in concentrated solid-solution alloys was determined by the means of positron annihilation lifetime spectroscopy.

Before dealing with these issues, in chapter 2, the basics of positron annihilation spectroscopy will be briefly introduced and an overview about the current state of research concerning the material classes of light weight alloys (focusing on Al–Mg–Si alloys), and concentrated solid-solution alloys (focusing on CoCrFeMnNi-alloys) will be given. The experimental techniques and details on the samples investigated are described in chapter 3. In chapter 4 the results are presented by incorporating the respective publications with a preamble preceding each publication. The results will then be summarized and discussed in the final chapter 5.

2 | Basics: Positrons and materials

In this chapter, the most important basics concerning the method of positron annihilation spectroscopy and the investigated material classes of light weight alloys and concentrated solid-solution alloys are introduced. An overview of the current state of research will be given with a focus on the application of positron annihilation spectroscopy for the study of defects and phase transformations in the investigated material classes, or to be more explicit for the study of precipitation processes in light weight alloys and the study of vacancy-type defects in concentrated solid-solution alloys.

2.1   Positrons

The positron is the antiparticle of the electron and, as such, a fermionic, elementary particle. It has the same spin and (within experimental limits) the same mass as the electron, but exhibits the opposite charge and magnetic moment. The existence of positrons and anti-matter in general was first predicted by Dirac in 1928 as an explanation for negative energy eigenvalues of particles at rest [18]. In 1932, Carl David Anderson observed indications for an unknown particle in cloud chamber photographs of cosmic rays [19]; the experimental proof for the existence of positrons was found.

2.1.1   Positrons in solids

Positrons entering a solid are slowed down to thermal energies within several picoseconds [1] by inelastic scattering with conduction electrons at higher kinetic energies followed by inelastic phonon scattering at lower kinetic energies [20]. The implantation profile $\bar{P}(z)$ of positrons in a material to a depth z depends on the maximum positron energy E_{max} [MeV] and the mass density ρ [g cm^{-3}] of the sample [21]

$$\bar{P}(z) = \exp\{-\alpha z\} \qquad \text{with} \qquad \alpha = 17 \cdot \frac{\rho}{E_{max}^{1.43}}. \tag{2.1}$$

After being thermalised, positrons diffuse through the material until they annihilate with an electron. The mean positron diffusion length L_+ is given by [22]

$$L_+ = \sqrt{6D\tau_1} \tag{2.2}$$

with D the material specific diffusion coefficient and the lifetime component τ_1 (see also equation (2.6)). For metals, typical positron diffusion lengths are significantly shorter than the mean implantation depths reached by positrons emitted from radioactive sources. For this reason, these positrons are an ideal tool for bulk investigations. Positrons diffusing through a defect free crystal lattice are repelled by the positively charged atomic nuclei through Coulomb interactions and thus experience the highest position probability in the interstitial regions. From this defect-free bulk state positrons will eventually annihilate with electrons from the surrounding medium with an annihilation rate λ, which is the inverse of the positron lifetime τ in the bulk of the material and directly proportional to the overlap of the positron $n_+(\mathbf{r})$ and the electron density function $n_-(\mathbf{r})$ [23]:

$$\lambda = \frac{1}{\tau} = \pi r_0^2 c \int n_+(\mathbf{r}) n_-(\mathbf{r}) \gamma[n_-(\mathbf{r})] \, d\mathbf{r}. \tag{2.3}$$

Where r_0 is the classical electron radius, c the speed of light and $\mathbf{r}$ is the position vector. The term $\gamma[n_-(\mathbf{r})]$ describes the enhancement effect which is the increase of the electron density due to the Coulomb attraction between a positron and an electron. The annihilation of an electron-positron pair from the delocalized bulk state is a relativistic process where the masses of the corresponding particles are converted into electromagnetic energy according to $E = m_0 c^2$, with m_0 the rest mass of the electron/positron and c the speed of light. The electron-positron annihilation under the emission of one γ-ray is only possible in the presence of a third body absorbing the recoil momentum and occurs with a negligible probability. The predominant process is the annihilation of the positron-electron pair emitting two γ-rays. The annihilation into three γ-rays is also possible but the spin-averaged cross section of this process is more than two orders of magnitude smaller than that for the two γ-annihilation [24]. As equation (2.3) shows, the positron lifetime τ in a defect-free crystal is indirectly proportional to the electron density and is thus a material specific parameter, typically ranging from 100 ps to 300 ps for defect-free metals (see for example ref. [25]).

2.1.2 Trapping model

If a crystal includes open volume defects such as pores, vacancies or dislocations, positrons experience an attractive potential at these sites due to the lack of a positively charged, repulsive ion core and eventually get trapped with a trapping rate κ_d. Since also the electron density in open volume defects is reduced, positrons not only get trapped but also exhibit a decreased annihilation rate λ and thus an increased lifetime τ compared to the lifetime corresponding to annihilation in the defect-free bulk. A phenomenological description of positron trapping at defects, referred to as trapping model was first given in 1970 [26] and has later on been generalized (see, e.g., refs. [27, 28].

Figure 2.3 shows a schematic sketch of the simplest trapping model for the presence of only one defect type. Positrons emitted by a radioactive source enter the solid where they thermalize and either annihilate in the defect-free bulk with a corresponding annihilation
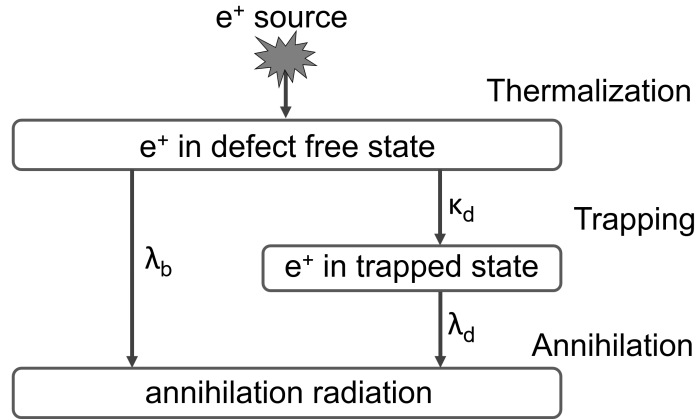
Figure 2.1: Schematic sketch of the trapping model with one defect type. After positrons penetrate into the solid and thermalize, they can either annihilate in the defect free bulk with the annihilation rate λ_b or they get trapped by a defect with the trapping rate κ_d and annihilate with a smaller annihilation rate λ_d. Picture redrawn after [29].

rate λ_b or get trapped by a defect with a trapping rate κ_d. For this two-state trapping model the possibility of positron detrapping from a defect is not taken into consideration. This means that the thermal escape of a positron from the bound state in the attractive potential of a defect is excluded, which is usually the case for trapping at vacancies. From the trapped state in a defect positrons annihilate with a corresponding annihilation rate λ_d, which is in general smaller than the bulk annihilation rate λ_b due to a reduced electron density. This situation can be described by the following rate equations

$$
\begin{aligned}
\frac{\mathrm{d}n_b(t)}{\mathrm{d}t} &= -(\lambda_b + \kappa_d)n_b(t), \\
\frac{\mathrm{d}n_d(t)}{\mathrm{d}t} &= -\lambda_d n_d(t) + \kappa_d n_b(t).
\end{aligned}
\tag{2.4}
$$

The number of positrons in the bulk and in the defect state at the time t are given by n_b and n_d, respectively. With the starting conditions $n_b(0) = N_0$ and $n_d(0) = 0$, which refer to the situation that there shall be a number of N_0 positrons in the bulk at a time $t = 0$ and that no trapping occurs at $t = 0$, before thermal energies are reached, the system of equations (2.4) can be solved. The solution of equation (2.4) is given by the total number

of positrons at a time t with

$$n(t) = I_1 \exp\left\{-\frac{t}{\tau_1}\right\} + I_2 \exp\left\{-\frac{t}{\tau_2}\right\} \tag{2.5}$$

with

$$n(t) = n_{\mathrm{b}}(t) + n_{\mathrm{d}}(t),$$

$$\tau_1^{-1} = \lambda_{\mathrm{b}} + \kappa_{\mathrm{d}}, \ \ \tau_2^{-1} = \lambda_{\mathrm{d}}, \tag{2.6}$$

$$I_1 = 1 - I_2, \ \ I_2 = \frac{\kappa_{\mathrm{d}}}{\lambda_{\mathrm{b}} - \lambda_{\mathrm{d}} + \kappa_{\mathrm{d}}}$$

In positron annihilation lifetime spectroscopy, the total annihilation probability given by the absolute value of the time derivative of $n(t)$ (equation (2.5)) is determined experimentally:

$$\left|P(t)\right| = \left|\frac{\mathrm{d}n(t)}{\mathrm{d}t}\right| = \frac{I_1}{\tau_1} \exp\left\{-\frac{t}{\tau_1}\right\} + \frac{I_2}{\tau_2} \exp\left\{-\frac{t}{\tau_2}\right\} \tag{2.7}$$

Equation (2.7) shows that for a material including one defect type, the experimentally observed positron lifetime spectrum consists of two individual exponential decays, corresponding to the lifetimes τ_1 and τ_2 with intensities I_1 and I_2.

From equation (2.6) it is obvious that τ_1, I_1 and I_2 depend on the trapping rate κ_{d}. For very small values of κ_{d} the intensity component I_2 goes to zero and no trapping of positrons at defects occurs. In this case the lifetime spectrum consists of only one exponential decay and positrons annihilate only from the free state within the bulk which means that τ_1 equals the positron lifetime τ_{bulk} corresponding to positron annihilation in the bulk of the material. Note that this is not generally valid, in all other cases the lifetime corresponding to annihilations in the bulk τ_{bulk} has to be calculated according to:

$$\tau_{\mathrm{bulk}} = \left(\frac{I_1}{\tau_1} + \frac{I_2}{\tau_2}\right)^{-1}. \tag{2.8}$$

If on the other hand, the trapping rate κ_{d} is very large, the intensity I_2 of the second lifetime component τ_2 approaches one, which means that all positrons are trapped in defects, i.e.,

saturation trapping at defects occurs. The trapping rate κ_d is directly related to the defect concentration C in the sample and can be calculated from the values I_i and τ_i as follows:

$$\kappa_d = \sigma C = I_2\left(\frac{1}{\tau_1} - \frac{1}{\tau_2}\right), \tag{2.9}$$

where σ is the specific trapping rate. If typical values for single vacancies of σ in the range of 10^{14} s^{-1} - 10^{15} s^{-1} [1, 25] and bulk lifetimes of around 100 ps [22] are assumed, it can be concluded that the sensitivity of positron annihilation spectroscopy to defects ranges from $C=10^{-7}$ - 10^{-4}. Another important variable in positron spectroscopy is the mean positron lifetime τ_{mean}, which can include information about the relative changes of the defect concentration. The mean positron lifetime τ_{mean} is rather insensitive to the applied fitting procedure and is given by

$$\tau_{mean} = \int_0^\infty tP(t)\ dt = \sum_{i=1}^2 I_i\tau_i. \tag{2.10}$$

Note that this so-called simple trapping model is only valid for the case of positron capture in a single type of open-volume defects. It can, for example, be extended for the case of trapping in several independent defect types or thermal detrapping with a certain detrapping rate (see e.g. ref. [29]). While, the trapping of positrons at vacancy-type point defects can be well described by the above presented simple trapping model, diffusion limitation has to be taken into account for trapping at extended defects such as grain boundaries, interfaces, voids, clusters or precipitates.

2.1.3   Diffusion-reaction model

In fact, the trapping process of positrons does not only depend on the capture mechanism itself but also on the diffusion of positrons, i.e., the motion of positrons from the point of thermalization to the vicinity of a trap. However, if the specific trapping rate σ is sufficiently low, the rate-equation approach, i.e., the simple trapping model, is justified when the

following condition is fulfilled [28]:

$$\sigma \ll 4\pi r_0 D / V_A, \tag{2.11}$$

where r_0 is the trapping radius, D is the positron diffusivity, and V_A is the atomic volume. For the trapping of positrons at atomic defects, such as monovacancies in metals, with specific trapping rates typically of the order $4{\cdot}10^{14}$ s^{-1} [30] and positron diffusivities of D$\approx 10^{-4}$ m^{2}s^{-1} [31] and typical values of the trapping radius and the atomic volume V$_A$, this condition is usually accomplished and the simple trapping model can be applied.

When the positron trapping rate into defects is so high that the positron density is depleted around the trap, diffusion related factors become dominant. Hence, for example for extended defects, both diffusion limitation but also transition limitation of positron trapping has to be taken into account, the so-called diffusion-reaction model should be applied. One limiting case is a regime where the trapping of positrons is essentially controlled by transport factors, the diffusion-limited regime. The other one, which is called transition-limited regime, is characterized by rapid transport and low transition rates. The intermediate case, where diffusion- and reaction-limitations are taken into account is described by the diffusion-reaction model.

The diffusion of positrons before annihilation has first been modeled for the trapping of positrons at surfaces of small particles for entirely diffusion-controlled trapping [27]. However, the resulting positron diffusivities [32] turned out to be too low compared with more direct determinations [31], which suggests that the reaction-limitation associated with the trapping process at the surface of small particles or grain boundaries has also to be taken into account. A more general diffusion-reaction theory was then worked out for positron trapping at point defects by Frank and Seeger in 1974 [28]. This model was later on applied to the positron motion and trapping in the presence of voids [33], flat surfaces [34] and grain boundaries [35]. Further studies on diffusion-reaction-controlled trapping include detrapping [36–38] and trapping at grain boundaries with competitive transition-limited trapping

at point defects in crystals [37, 39–41].

Contrary to previous studies, Würschum and Seeger in 1996 [36] were the first to give closed-form expressions for the mean positron lifetime and the intensity of the annihilation component associated with the trapped state for the diffusion-reaction problem of positron trapping at grain boundaries. This model was extended to include competitive positron trapping at grain boundaries and point defects by Oberdorfer and Würschum in 2009 [40]. In section 4.3 two most recent publications are presented which further extend this approach.

2.2   Materials: State of research

In the following section the most important basics and modern research on the material classes of light weight alloys and concentrated solid-solution alloys, providing the basis for this thesis, will be given. Note that this is a summary and as such a brief overview only; more detailed information can be found in the references given.

2.2.1   Light weight alloys

Light weight alloys are widely used for industrial applications due to their outstanding mechanical and electrochemical properties in combination with very low weight. The basis of the broad applicability of light weight alloys is the process of age hardening, referring to an increase of the hardness of the material during its storage at room temperature or at elevated temperatures, which was patented by Alfred Wilm in 1909 [42]. The most relevant alloying elements in Al alloys are Cu, Mn, Si, Mg and Zn which are used in combination or together with other minor alloying elements. Different compositions result in varying, characteristic material properties of Al alloys allowing for a classification into certain groups. Furthermore, Al alloys can be discerned depending on their production procedure, in cast and wrought alloys. Among the numerous different systems of Al alloy, nowadays, especially the age hardenable wrought alloy systems Al–Mg–Si, Al–Cu–Mg, Al–Zn–Mg(–Cu) play a major role for industrial applications.

The specific light weight alloy being the subject of this thesis is a commercial AW 6060 alloy, which is a type of age-hardenable, low-alloyed Al–Mg–Si alloy (for the exact composition of the AW 6060 alloy see section 3.2.1). Al–Mg–Si alloys are used in a wide range of sectors, as for example in automotive industry [43] as car body parts or for architectural and structural applications [44]. Al–Mg–Si alloys can be discerned by the ratio of their Mg to Si content. In general alloys with a Mg/Si-ratio of 2 are referred to as balanced alloys since this is the stoichiometric composition of the equilibrium β phase (Mg_2Si) that appears after prolonged age hardening. Alloys with a Mg/Si-ratio less than 2 are referred to as excess-Si alloys and those with a Mg/Si-ratio larger than 2 as excess-Mg alloys. In practice, the Mg/Si-ratio of an excess-Si alloy is mostly less than one, which is why the commercial AW 6060 alloy can best be compared to a balanced alloy.
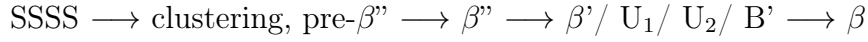
Note that the state of research presented below corresponds to Al–Mg–Si alloys, with an emphasis on the age hardening of these alloy type and the study of the resulting precipitation sequence using positron annihilation methods. For further, more detailed information on light weight alloys in general, but also on the Al–Mg–Si system see, e.g., refs. [45, 46].

Age hardening of Al–Mg–Si alloys

The industrially applied process of age-hardening is a thermally activated, diffusion-driven transformation. In this procedure, the alloy is rapidly cooled from a high temperature single-phase region to a low temperature two-phase region, according to the phase diagram, to obtain a supersaturated solid solution. The material is then stored at room temperature (where so-called 'Natural aging' occurs) or at elevated temperatures, typically around 180°C [1] (resulting in so-called 'Artificial aging'). Both temperature treatments enable the growth of a sequence of precipitates of varying characteristics in the Al matrix which can serve to harden the material by hindering dislocation movement [47]. For Al–Mg–Si alloys a generally agreed model is the following precipitation sequence [2]:

---

[1]In connection to the industrially applied process of age hardening temperatures are usually given in degrees Celsius. Therefore, this unit is also used in this thesis when the temperatures given refer to heat treatments in connection to artificial aging.

$$\text{SSSS} \longrightarrow \text{clustering, pre-}\beta\text{''} \longrightarrow \beta\text{''} \longrightarrow \beta\text{'}/ \text{ U}_1/ \text{ U}_2/ \text{ B'} \longrightarrow \beta$$

Where SSSS denotes the supersaturated solid-solution and β'' refers to the metastable fully coherent phase while β', U_1, U_2 and B' are semi-coherent phases. The final, incoherent equilibrium phase is denoted as β phase. Note that a general and exact precipitation sequence of Al–Mg–Si alloys is still under discussion and strongly varies depending on alloy compositions and different heat treatment conditions. The precipitation sequence stated above and described in more detail below, is a summary of existing studies reported in literature, and best applicable to the alloy investigated in this thesis considering its exact composition and heat treatment condition.

Clustering/ pre-β'' precipitates

Starting from a supersaturated solid-solution, clusters form already during or shortly after quenching. Clusters are defined as agglomerates of solute atoms without atomic ordering placed on substitutional lattice points of the Al lattice. While Mg is expanding the Al matrix, Si is contracting it, which leads to a strong driving force for the formation of clusters including alternating Mg and Si atoms [48]. From these clusters there seems to be a continuous transition to pre-β'' phases, which is why it remains unclear, if and how a clear distinction can be made between clustering and pre-β'' stages. One possibility would be that agglomerates without atomic ordering are denoted as clusters, and precipitates with a distinct crystal structure as pre-β'' phases. Regarding the composition and structure a wide range of cluster and pre-β'' phases can be found strongly depending on the exact alloy composition and applied aging temperatures [48–52].

The β'' phase

The subsequently formed β'' phase is of monoclinic crystal structure and as such the first phase with non-fcc structure in the precipitation sequence. The β'' precipitates are fine needle-shaped, metastable precipitates along $<100>_{Al}$ of typically $(4\times4\times50)$ nm^3 [53]. The β'' phase leads to a maximum increase in hardness, i.e., the β'' phase is pre-dominant in

the peak hardness conditions of the alloy. Concerning the composition of the β" phase various studies including techniques such as transmission electron microscopy, X-ray measurements and atom probe tomography have been conducted which came to slightly varying results [53–55]. The most recent studies applied HAADF-STEM (high-angle annular dark-field scanning transmission electron microscopy) measurements and DFT (density-functional theory) calculations, which included influences of the surrounding strain fields, and agreed on $Mg_4Al_3Si_4$ to be the most likely crystal structure of β" precipitates [56, 57].

The β'/ U_1/ U_2/ B' phase

With ongoing aging time, the fraction of coherent β" precipitates decreases again and an increasing fraction of semi-coherent β' precipitates exists, which leads to a decrease in hardness after the peak-aged state (so-called overaged regime). Contrary to an early study [58], it was found later that during this aging state more than one, in particular four different types of semi-coherent precipitates (β'-, U_1-, U_2-, B'-phase) can exist in parallel, depending on the alloy composition and the preceding heat treatment [59–61]. The β' phase is of hexagonal crystal structure and rod-shaped along $<100>_{Al}$. These rods show a length of several hundred nanometers and a diameter of approximately 10 nm [62]. The structure of the β' phase (chemical composition: Mg_9Si_5 [62]) is already very similar to that of the then following final β phase, basically only the ratio of the Mg/Si content changes.

The β phase

The final equilibrium phase of the precipitation sequence of Al–Mg–Si alloys is declared β phase and refers to incoherent Mg_2Si-precipitates [63]. The β phase is plate-shaped lying on $(100)_{Al}$ with an fcc (Ca_2F)-structure and reaches up to 10 - 20 μm in lateral dimensions [62].

It can be summarized that precipitates appearing in the overaged regime after the peak-hardening have already been well characterized. However, regarding the whole precipitation sequence open questions are still left that have been addressed in the framework of this

thesis:

- Early stages of the precipitation sequence are, in general, difficult to assess due to the smallness of the formed structures but also due to the low content of Mg and Si in the alloy. Further, the electronic structures of Al, Mg and Si are very similar as they are neighbouring elements in the periodic table. This fact results in a low elemental contrast in electron microscopy and X-ray diffraction techniques and hence weak signals from clusters enriched in Mg and Si embedded in an Al matrix [64]. However, especially these early phases heavily influence the maximum hardness response and more detailed insights into these atomistic processes are of major importance for the optimization of age-hardening.

- In general, the Al–Mg–Si precipitation sequence is a rather continuous process where multiple precipitates evolve in parallel [49, 65], making it more difficult to investigate the individual phases.

- The precipitation sequence is drastically influenced by the exact composition of the alloy which complicates a comprehensive study of the process. For example, excess-Si light weight alloys show single solute Si-clusters during the early clustering stages which do not appear in balanced or excess-Mg alloys [2, 66]. Further, only in the case of a balanced Al–Mg–Si alloy, the β' phase is the predominant phase among β', U_1, U_2 and B' precipitates, whereas for excess-Mg alloys also the U_2 phase arises in significant amounts [60].

- Other essential parameters determining the response of the alloy to age hardening are the initially applied heat treatment and the applied aging temperature. For example, artificial aging at 180°C results in a higher number density of β" precipitates and thus a higher hardness than aging at 210°C [67]. Of particular industrial importance is also the negative effect on the hardening response of natural pre-aging prior to artificial aging. For an Al-Mg-Si balance alloy it was found that storage at room temperature

reduces the number density of β'' precipitates appearing during subsequent artificial aging and thus reduces the hardening response [68]. The same effect was also found for the AA-6061 alloy and explained by the fact that quenched-in vacancies are bound with co-clusters during natural aging and hence cannot assist diffusion during subsequent artificial aging anymore [69].

Consequently, especially for the early stages in the precipitation sequence, specific, systematic and comprehensive studies are necessary to gain full understanding of each alloy system and to be able to tailor the hardening response of the material and other important properties.

Positron annihilation spectroscopy for the study of precipitation sequences in light weight alloys

Positron annihilation spectroscopy has been proven to be a highly suitable tool for the study of precipitation sequences in light weight alloys [3, 4]. Positrons are sensitive to changes in open volume defects such as vacancies, which serve as diffusion vehicles for the formation of clusters and precipitates during the whole precipitation sequence. Additionally, positrons may also get trapped by coherent clusters and precipitates, i.e., by phases completely free of defects which appear in the early precipitation stages. This behaviour is caused by the fact that typical alloying elements such as Mg and Si show higher positron affinities than the Al host matrix [4, 5, 70]. Furthermore, semi-coherent and incoherent precipitates that appear in the overaged regime of the alloy can act as positron traps as they include misfit defects with large open volumes.

Figure 2.2 schematically shows a fully coherent, a semi-coherent and an incoherent precipitate, the corresponding attractive potential $V_+(r)$ for positrons and the localization of the positron wave function $|\Psi|^2$. In the case of a coherent precipitate (see figure 2.2(a)) the positron wave function is spread over the whole precipitate. The attractive potential $V_+(r)$ of a coherent precipitate increases with the difference in positron affinities of the elements in
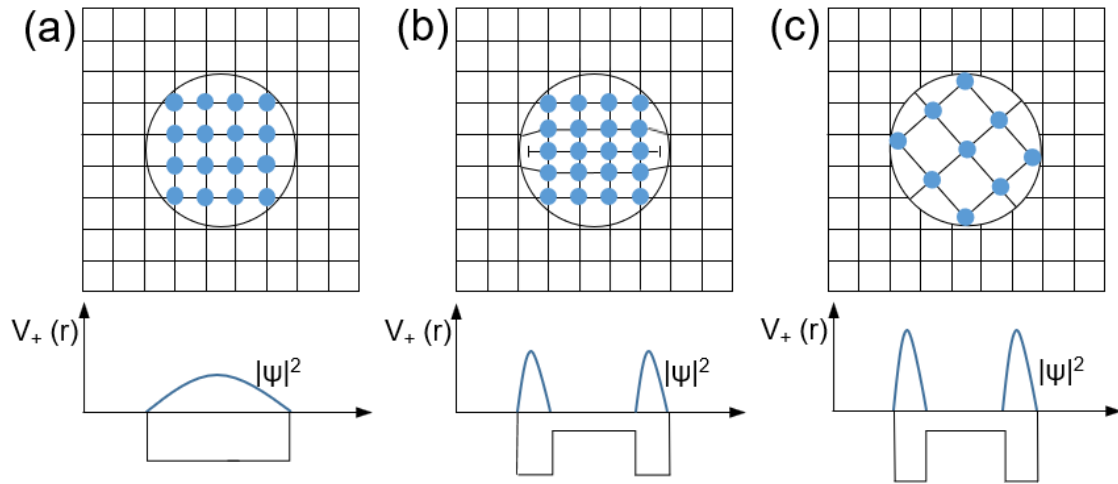
Figure 2.2: Schematic sketch of a (a) fully coherent (b) semi-coherent (c) incoherent precipitate in the host matrix and the corresponding attractive potential $V_+(r)$ and localization of the positron wave function $|\Psi|^2$. Picture redrawn after [70].

the host matrix and those in the precipitate. For small differences of the positron affinities and corresponding weak attractive potentials coherent precipitates act as so-called shallow positron traps. Shallow positron traps are defined as traps which weakly bind positrons, with binding energies E_b equal or below thermal energies. On the contrary, deep positron traps, show binding energies E_b well above thermal energies such as for example vacancies with $E_b \approx 1$ eV [29]. It is also possible that the interfaces of semi-coherent and incoherent precipitates (see figure 2.2 (b),(c)) act as deep positron traps. They always include misfit defects with higher attractive potentials $V_+(r)$ for positrons and thus cause a stronger localization of the positron wave function than the rest of the precipitates.

Extensive positron annihilation studies have been done so far on the precipitation sequence occurring during natural aging of Al–Mg–Si alloys [6, 7, 64, 71, 72]. It was found that different stages of the precipitation process occurring during natural aging can be assessed by monitoring variations of the positron lifetime during room temperature storage. Furthermore, by the application of temperature dependent positron lifetime spectroscopy, it could already be shown that solute clusters appearing in the early stages during natural aging

act as shallow positron traps with positron binding energies E_b of 55 meV [73]. During the course of natural aging these clusters agglomerate to precipitates and then show an increased positron binding energy (E_b >1 eV) acting as deep positron traps. The equilibrium β phase of an excess-Mg Al–Mg–Si alloy was studied using a positron microbeam [74] for the measurement of the Doppler broadening annihilation radiation. Furthermore, Doppler broadening spectroscopy was conducted for different states of natural aging of excess-Si Al–Mg–Si alloys [72, 75].

Concerning the artificial aging process, positron annihilation studies were previously conducted on the Al–Mg–Si alloy AW 6061 [70]. However, the AW-6061 alloy differs from the AW 6060 alloy, which was the material of interest in this thesis, by including Cu additions, and results on the precipitation sequence of those alloys can hence not directly be compared. Furthermore, several datapoints corresponding to the positron lifetime after artificial aging of a pure ternary Al–Mg–Si alloy were presented by the group of Banhart [72]. Very recently further positron annihilation lifetime studies concerning the artificial aging of a Si-excess [76] and a lean Al–Mg–Si alloy [77], which is very similar to the AW 6060 alloy investigated in this thesis, were published.

It can be concluded that the natural aging of Al alloys, especially those including Cu additions, has been extensively studied by positron annihilation spectroscopy [6,7,64,71,73]. Still, only very few positron lifetime studies concerning the artificial aging of Al–Mg–Si alloys, comparable to the here investigated commercial AW 6060 alloy, can be found in literature [72, 77]. Furthermore, these artificial aging studies mostly included only positron lifetime data measured at room temperature, which means that these results are valid for artificial aging superimposed with natural aging, which makes it very difficult to resolve the complex atomistic processes during the early stages of the precipitation sequence. To overcome these difficulties either ex-situ measurements at low temperatures to prevent secondary natural aging or in-situ measurements at high temperatures are required, these points will be presented in the publications [8–10] in section 4.1 in this thesis.

2.2.2   Equiatomic multicomponent alloys or high-entropy alloys

The design of traditional alloys is based on one or two principal metallic elements, that form the base alloy, with minor additions of other elements in order to achieve desired microstructures and properties. General knowledge on the complexity of metallurgic phase diagrams further supported the conventional alloying concept as already phase diagrams of two and three component alloys can include a wide range of equilibrium phases of intermetallic compounds and intermediate phases. Therefore, for a long time, the classical alloying concept remained untouched, even though it still restricted the possibility of covering special microstructures, properties and applications.

Then, in 2004, the concept of high-entropy alloys, which are also referred to as equiatomic multicomponent alloys or concentrated solid-solution alloys, was introduced [78, 79]. Brian Cantor and his group [79], who initiated research on equiatomic, multicomponent alloys already in 1984, were the first to show that the equiatomic CoCrFeMnNi alloy, nowadays often referred to as Cantor alloy, shows a single face-centered cubic crystal structure. In an independent publication Yeh et al., introduced the denotation 'high-entropy alloys' for these equiatomic multicomponent alloys [78]. It was suggested that the solid-solution phase in high entropy alloys is stabilized by a high entropy of mixing $\Delta S_{\mathrm{mix}} = -R \sum_i x_i \ln x_i$, with R the gas constant and x the mole fraction of constituent i.

In general, there are two ways for the definition of high-entropy alloys, which is either based on the alloys composition or on its configurational entropy [80]. Regarding its composition, an alloy is defined as high-entropy alloy if it consists of at least five principal elements, each with an atomic percentage between 5 % and 35 %, with the atomic contribution of any other element being less than 5 %:

$$n_{\mathrm{major}} \geq 5, \; 5 \; \% \leq x_i \leq 35 \; \%, \; n_{\mathrm{minor}} \geq 0, \; x_j \leq 5 \; \% \qquad (2.12)$$

with n_{major} and n_{minor} as the number of major and minor elements, respectively. x_{i} and x_{j} are the atomic percentages of major element i and minor element j.

Furthermore, high entropy alloys can be defined as alloys with a configurational entropy $\Delta S_{\mathrm{config}}$ larger than 1.5 R at a random state:

$$\Delta S_{\mathrm{config}} \geq 1.5 \; R \tag{2.13}$$

Note that the total mixing entropy ΔS_{mix} of the alloy, which should minimize Gibbs free energy and thus stabilize the solid solution according to Ref. [78] is a sum of the configurational, vibrational, magnetic dipole and electronic randomness entropy terms. However, due to the configurational entropy being dominant over the other three contributions, the mixing entropy ΔS_{mix} is often referred to as $\Delta S_{\mathrm{config}}$ [80].

Both of these definitions are meant to realize a sufficiently high entropy of mixing, ΔS_{mix}, in order to allow the formation of solid solution phases. Anyhow, there are numerous alloy systems which can be classified as high-entropy alloys due to their number of components and configurational entropy, but still do not show solid solution phases. For example Cantor et al. [79] produced a multi-component alloy consisting of 20 elements in equimolar fractions, among them Co, Cr, Fe, Mn and Ni, which showed a brittle multi-phase microstructure despite its significantly higher configurational entropy compared to the equiatomic CoCrFeMnNi alloy, which shows a single fcc phase. In a further study on a single-phase, equiatomic CoCrFeMnNi alloy [81] the individual elements were replaced one at a time by elements showing the same room temperature crystal structure and comparable sizes and electronegativities to produce five new equiatomic, quinary alloys. After three days of annealing only the original CoCrFeMnNi alloy showed a single-phase microstructure, in all other alloys multiple phases were observed. Hence, simply increasing the number of components and the entropy of mixing of an alloy does not increase the solid-solution stability of a multi-component alloy. Or in other words, the configurational entropy cannot be used to predict a-priori whether a high-entropy alloy will form a thermodynamically stable solid-

solution or not. It has been shown that other effects, such as atomic size differences and packing or formation enthalpies [82, 83], also play an important role and have to be taken into account. In the present thesis the investigated multi-component alloys (see also section 4.2) were declared as concentrated solid-solution alloys. For one thing, to clarify that all investigated samples showed a single fcc crystal structure, but further also because not all of these alloys, which consisted of three to five components, had a configurational entropy higher than 1.5 R.

One of the initially proposed core effects of high entropy alloys was the so-called 'sluggish' diffusion behaviour [78]. It was assumed that due to the random mixture of different kinds of atoms on the lattice sites there should be a greater fluctuation of lattice potential energy producing atomic traps and blocks, leading to higher activation energies for diffusion. Recent diffusion studies come to the conclusion that the diffusion behaviour strongly depends on the specific element which is diffusing, the matrix and the concentrations of the individual elements and thus the term 'sluggish diffusion' is not generally appropriate for high entropy alloys [84, 85].

Furthermore, it turned out that equiatomic multicomponent alloys can experience a variety of desired mechanical properties. They show high strength and ductility, also at high temperatures [13, 14], outstanding wear- and corrosion-resistance [86, 87] but also enhanced resistance to radiation [15, 16]. These properties make them strong candidates for the application as structural material in extreme environments, such as, for example, nuclear reactors. Knowledge about the diffusion kinetics and vacancy characteristics are of high importance for a comprehensive understanding of these effects in concentrated solid-solution alloys such as radiation tolerance or mechanical behaviour. Thus defect studies on these alloys are not only interesting for fundamental research but also for further development towards their applications.

Positron annihilation spectroscopy for the study of defects in concentrated solid-solution alloys

The formation and migration behaviour of vacancies in concentrated solid-solution alloys is not only strongly connected to their specific diffusion properties, which are still under debate, but could also be of great interest in connection to the high strength and ductility at elevated temperatures and the radiation resistance of concentrated solid-solution alloys. The method of positron annihilation spectroscopy is, of course, not only a suitable method for the study of vacancies in pure metals and conventional alloys (see, e.g., refs. [88,89]), but can also be applied for the material class of concentrated solid-solution alloys.

So far, only three positron studies on CoCrFeNi and CoCrFeMnNi concentrated solid-solution alloys with partly contradicting results have been reported [90–92]. For as-cast CoCrFeNi a single positron lifetime of 160 ps was found, which was referred to saturation trapping of positrons in dislocations associated with vacancies [90]. The positron lifetime was then measured in dependence of the annealing temperature; for temperatures of about 1200 K the lifetime showed a value of 108 ps, which was referred to annihilations in the bulk of the material. In the whole study only a single lifetime component could be observed, which may be due to the fact that a deconvolution into two components was not possible with a time resolution of 260 ps.

A second positron study on CoCrFeMnNi came to the conclusion that defects in the form of vacancies are only present in the subsurface region and originate from electro-erosion of the sample [91]. A positron lifetime component of 112 ps was related to the annihilation of positrons in the bulk of the CoCrFeMnNi sample.

Just recently, for the CoCrFeMnNi alloy, measurements of the positron lifetime in dependence of the temperature in the range from 293 K to 1423 K were conducted. At room temperature a positron lifetime of 108 ps, which was ascribed to be corresponding to annihilations in the defect-free bulk, was observed. With increasing temperature, the mean positron lifetime increased and reached a maximum value of approximately 145 ps at a tem-
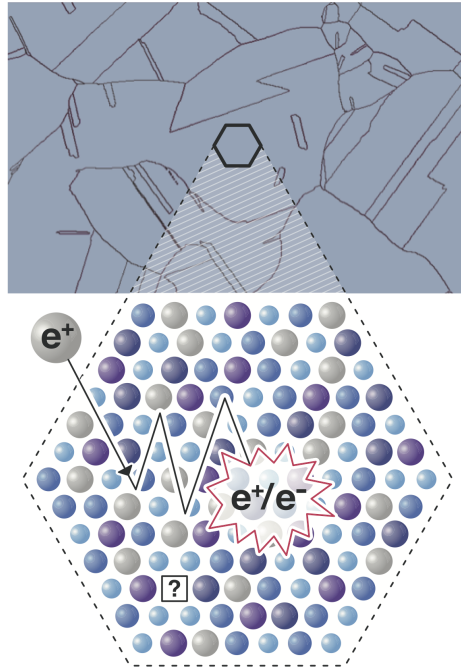
Figure 2.3: EBSD phase mapping (top, light blue, here exemplary for CrFeNi alloy) of concentrated solid-solution alloy and schematic sketch (hexagon) of the crystal lattice which is randomly populated with different elements. A positron (e^+) diffuses through the crystal lattice and annihilates with an electron of the sample.

perature of 1423 K. It was stated that a rapid increase of the mean positron lifetime at higher temperatures (1200 K-1400 K) was due to the thermal generation of vacancies. However, some details of the positron lifetime data in dependence of the temperature in this study did not seem coherent to the authors, as it will be discussed in section 4.2 and ref. [17].

From these initial studies still many questions are left open regarding the role of vacancies in fcc concentrated solid-solution alloys. It remained unclear if a defect-related lifetime component found in CoCrFeNi [90] was just due to positron annihilations in dislocations or related to annihilations in vacancies. From the recently observed [92] increase of the mean positron lifetime with temperature for the CoCrFeMnNi alloy it cannot be decided if this behavior is due to the thermal generation of vacancies or if other processes such as phase decomposition in the multicomponent matrix play a role.

<div align="center">

3 | Experimental

</div>

The key results of this thesis are obtained by applying positron annihilation lifetime spectroscopy at low temperatures around 205 K with a laboratory ^{22}Na positron source. Furthermore, also *in-situ* positron annihilation Doppler broadening spectroscopy at high temperatures ranging from approximately 453 K to 823 K ($\approx$180°C - 550°C) utilizing a high-intensity mono-energetic positron beam were conducted.

In the following chapter, both of these methods will briefly be explained. In the second section a list of samples investigated with their exact compositions and heat treatments applied prior to measurements will also be given.

3.1 Positron annihilation spectroscopy

The experimental method of positron annihilation spectroscopy can be classified into three main techniques, depending on which information concerning the annihilation γ-rays is being analysed: lifetime, Doppler line broadening and angular correlation spectroscopy. Within the following section only lifetime spectroscopy and Doppler line broadening spectroscopy will be addressed, since these methods were applied within the scope of this thesis.

3.1.1 Positron annihilation lifetime spectroscopy

In positron annihilation lifetime spectroscopy (PALS) the positron lifetime in a sample is measured as the time difference between the appearance of a so-called start γ-ray marking

the entry of the positron into the material and a stop γ-ray, corresponding to the positron annihilation in the material. In the laboratory measurements, presented in this thesis, the applied positron source is ^{22}Na, where positrons are generated by radioactive β^+-decay according to the decay reaction:

$$^{22}Na \rightarrow^{22} Ne^* + \beta^+ + \nu_e \tag{3.1}$$

$$^{22}Ne^* \rightarrow^{22} Ne + \gamma \tag{3.2}$$

where ^{22}Na decays into the excited state (^{22}Ne*) of ^{22}Ne by β^+-decay, where a proton decays into a neutron, an electroneutrino ν_e and a positron. The excited state ^{22}Ne* relaxes into the ground state emitting a γ-ray of 1275 keV. Positrons emitted by ^{22}Na exhibit a relatively broad, continuous energy spectrum up to a maximum energy of 540 keV. Besides ^{22}Na, for example also ^{58}Co or ^{64}Cu can be utilized as positron sources. However, since ^{22}Na has several advantages such as a high positron yield (90.4 %), and a convenient half life of 2.6 years, it is the most commonly used laboratory source. Furthermore, the 1275 keV γ-ray emitted in the β^+-decay of ^{22}Na can be utilized as start γ-ray, marking the "birth" of a positron. The annihilation of a positron with an electron in the material results in the emission of two collinear 511 keV γ-rays, serving as stop signals.

To detect the start- and stop-rays and record the positron lifetime spectrum a digital positron lifetime spectrometer is used. A block diagram of the whole measurement set-up can be seen in figure 3.1. The 1275 keV start and the 511 keV stop γ-rays are detected by plastic scintillator crystals (Pilot-U) connected to photomultiplier tubes, which deliver electrical pulses with intensities proportional to the energy of the incoming γ-ray. These pulses are then forwarded to the digital oscilloscope and to constant fraction differential discriminators (CFDD). In the digital oscilloscope, by implementation of a MATLAB program, start- and stop-pulses can be discerned, and by their time difference a histogram is generated, which
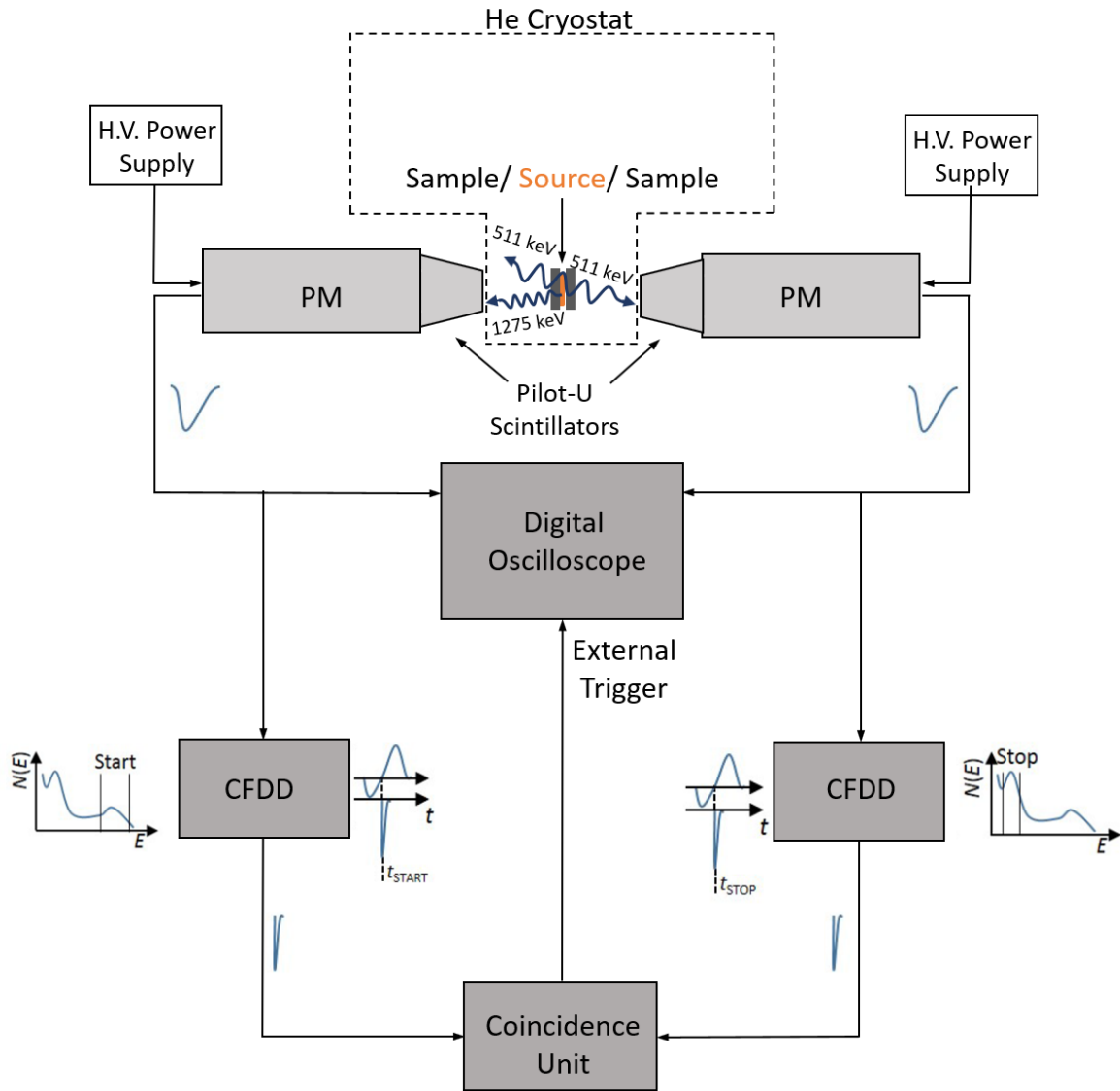
Figure 3.1 Block diagram of a digital positron lifetime spectrometer set-up
   H.V. Power Supply..Canberra 3002D
   PM..Photomultiplier tubes, Hamamatsu H2431-50
   CFDD..............................Constant fraction differential discriminator, ORTEC 583B
   Coincidence Unit..Fast Coincidence, ORTEC 414A
   He Cryostat..................closed-cycle He-cryostat and CTI-cryogenics 8300 compressor
   Digital Oscilloscope..............................LeCroy WaveRunner 625Zi, 2.5 GHz, 40 GS/s

represents the positron lifetime spectrum. To enable a better temporal resolution of the positron lifetime spectrum, the digital oscilloscope is externally triggered by two constant fraction differential discriminators and a coincidence unit. The constant fraction differential discriminators deliver a timing pulse at the arrival of the input signals irrespective of their heights if they are in certain predefined energy ranges of the start or stop signals; the coincidence unit delivers a pulse to the external trigger of the oscilloscope if the start and stop signals are in coincidence. This measurement procedure leads to a full width at half maximum of the time resolution function of the whole spectrometer set-up of typically 163 ps. The resulting positron lifetime spectra, which consists of a sum of exponential decays convolved with the spectrometer resolution function and a superimposed background, were analysed using the program PALS*fit3* [93]. The positron source, in the form of ^{22}NaCl, was used encapsulated in 2-3 layers of 5 μm thick Al foil. Thus when analyzing the positron lifetime spectra, annihilation of positrons in the dried NaCl-solution (τ_{NaCl}=420 ps [94, 95]) and in the Al foil (τ_{Al}=163 ps [96]) has to be taken into account.

For the positron lifetime measurements, the ^{22}Na source is put between a pair of identical samples to allow positrons to be injected into both samples. This so-called sample-source sandwich arrangement is then placed in the sample chamber of the measurement set-up, which is connected to a He-cryostat and a compressor pump allowing to cool down the sample pair during the measurement to minimum temperatures of around 10 K.

3.1.2 Positron annihilation Doppler broadening spectroscopy

Due to the conservation of momentum of the electron-positron pair the two 511 keV annihilation γ-rays show deviations from collinearity by the angle θ in the laboratory system. Further, also an energy shift ΔE of each annihilation photon appears, which is given by

$$\Delta E = \pm\frac{p_{\mathrm{z}}c}{2} \tag{3.3}$$

where p_{z} is the longitudinal momentum in the direction of the emitted photons and c is the speed of light. Since the thermalised positron does not contribute to the energy of the electron-positron pair, the Doppler shift ΔE can be assigned to the momentum of the electron alone. To detect the Doppler broadening of the electron-positron annihilation line high resolution detectors, such as high purity germanium detectors are used. For the evaluation of the Doppler broadening spectrum the so-called shape (S) and wing (W) parameters are introduced.
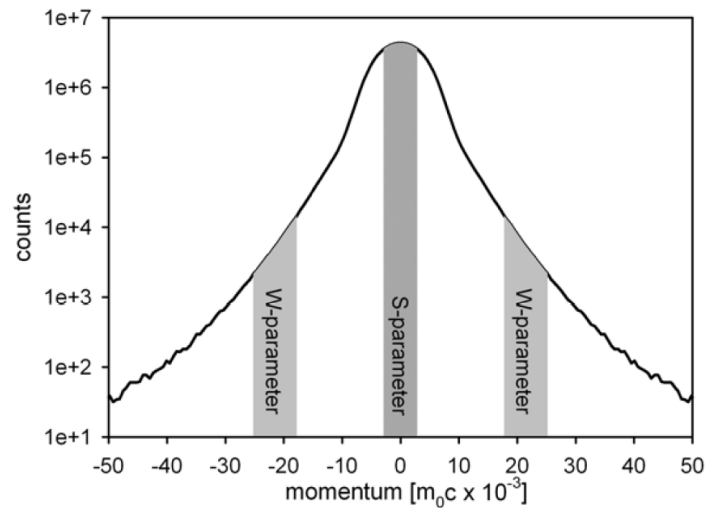

Figure 3.2: Doppler broadening spectrum of Al. The shaded areas show exemplary the areas used for the calculations of the S- and W-parameters. Picture taken from [97].

As indicated in figure 3.2 the S-parameter refers to the central area of the spectrum, close to the 511 keV main peak and is defined by:

$$S = \frac{\sum_{i=a}^{b} N_i}{\sum_i N_i} \tag{3.4}$$

where N_i is the content of channel i and a to b the interval of the sum. The S-parameter is a measure for annihilations with low momentum valence electrons and hence increases with an increasing fraction of positrons annihilating in open volume defects. As a consequence, the S-parameter can be used to monitor changes in open volume defects as for example the introduction and annealing of vacancies. Note that for the results on the Doppler broadening S-parameter presented in this thesis (see section 4.1.3) the region for the calculation of the S-parameter was chosen from 510.15 keV to 511.85 keV.

The W-parameter, on the other hand, refers to annihilations with high momentum core electrons and thus contains element specific information. It is calculated from the wings region of the spectrum (see figure 3.2) by:

$$W = \frac{\sum_{i=c}^{d} N_i + \sum_{i=-d}^{-c} N_i}{\sum_i N_i} \tag{3.5}$$

For an accurate measurement of the W-parameter a good peak to background ratio is needed. This can be achieved by so-called "coincident" Doppler broadening spectroscopy, where both γ-rays of one annihilation process are measured. This results in additional conditions that can be applied to the signals and lead to a reduction of the peak-to-background ratio. However, since the aim of the Doppler broadening measurements presented in this thesis (see section 4.1.3) was a fast temporal resolution of the precipitation processes in Al alloys the focus of the data evaluation was on the S-parameter only. For this reason, Doppler broadening data was recorded by four independent high purity Ge detectors which were not measuring in coincidence.

The NEutron induced POsitron source MUniCh (NEPOMUC)

For the Doppler broadening measurements presented in this thesis the Doppler broadening spectrometer at the NEutron induced POsitron source MUniCh (NEPOMUC) at the research neutron source Heinz Maier-Leibnitz (FRM II) of the Technical University of Munich was utilized which provides a high-intensity positron beam (10^9 moderated positrons per second) and thus enables fast spectra acquisition at short timescales [98, 99]. The NEPOMUC positron source consists of a cadmium cap and a platinum foil structure mounted in the tip of a beam tube inside the heavy water tank at FRM II. By the capture of thermal neutrons in the cadmium cap (^{113}Cd(n,γ)^{114}Cd) a γ-cascade is released, where on average 2.3 γ-rays with more than 1.5 MeV are emitted per neutron. The γ-rays are then absorbed in a converter, in the form of a structure of platinum foils, where positrons are generated by pair production. Since platinum has a negative positron work function, moderated, mono-energetic positrons are emitted from the platinum foil. The primary positron beam, with a kinetic energy of 1 keV then passes a remoderation unit for brightness enhancement and is then magnetically guided to one of the various experimental positron set-ups at the NEPOMUC facility, among them also the Doppler broadening (DB) spectrometer (see also Ref. [100]). The DB spectrometer consists of a beam guidance system realized by electrostatic and magnetic field coils, the brightness enhancement system, beam monitors, an electrostatic accelerator and a sample chamber. The final positron implantation energy can be varied up to 30 keV by biasing the sample and sample holder and electrically insulating it. For all measurements presented in this thesis the positron implantation energy was set to 28 keV (see section 4.1.3). The design of the sample chamber allows for temperature dependent *in situ* Doppler broadening spectroscopy from room temperature up to 1000 K by usage of a heatable sample holder [101]. For the variation of the temperature, the light of a 250 W halogen lamp is concentrated onto the back side of the sample by an ellipsoidal Cu reflector. The spot size of the positron beam at the sample was determined to be (253±40) μm at a beam energy of 30 keV [101]. For further information on the DB spectrometer at the NEPOMUC experiment see for example refs. [101, 102].

3.2   Samples investigated and sample preparation

3.2.1   Commercial Al–Mg–Si alloy: AW 6060

The Al–Mg–Si alloy being studied in this thesis was a commercial-grade AW 6060 alloy in a T6 condition, which means that the alloy has been subject of solution heat treatment and peak aging. The exact chemical composition has been determined by optical emission spectroscopy [103] and is shown in table 3.1. For the *ex situ* positron annihilation lifetime measurements squared sample pairs ($1.5 \times 10 \times 10$ mm^3) were cut from the AW 6060 rod and ground (grit-paper grade 1000). The individual sample pairs were prepared in well-defined heat treatment conditions prior to any lifetime measurements. To prevent them from secondary natural aging, the samples were stored in liquid nitrogen directly after heat treatment until they were mounted into the lifetime spectrometer. The helium cryostat attached to the sample chamber of the lifetime spectrometer allows to keep the samples at low temperatures (205 K) also during the time of data acquisition. For further details on the sample preparation and heat treatment prior to the *ex situ* positron lifetime measurements and the measurement procedures see also the experimental parts of the publications [8, 9] (sections 4.1.1 and 4.1.2).

For the *in situ* positron annihilation Doppler broadening measurements the ground (grit-paper grade 1000), square shaped samples ($1.5 \times 10 \times 10$ mm^3) were solution heat treated at 813 K (540°C) for 30 min. and then stored in liquid nitrogen until mounting them into the Doppler broadening spectrometer. The samples were artificially aged at 453.15 K (180°C) and 483.15 K (210°C) inside the Doppler broadening spectrometer during a continuous measurement of the S-parameter. Additionally, the S-parameter of the sample that has been age hardened at 483.15 K was recorded during solution heat treatment. For further details on the sample preparation and measurement procedure for the *in situ* Doppler broadening measurements see also the experimental part of publication [10] (section 4.1.3).

Table 3.1: Chemical composition of the AW 6060 alloy as determined by optical emission spectroscopy [103], the errors are represented by statistical deviations

element	wt.%	at.%
Mg	0.5790±0.0060	0.6430±0.0060
Si	0.5360±0.0070	0.5160±0.0070
Fe	0.2250±0.0020	0.1090±0.0010
Cu	0.0020±0.0010	0.0010±0.0003
Mn	0.0048±0.0001	0.0024±0.0001
Ti	0.0114±0.0005	0.0064±0.0002
Zn	0.0045±0.0018	0.0019±0.0007

3.2.2 Concentrated solid-solution alloys

The concentrated solid-solution alloy samples were prepared from raw materials by arc-melting (see also the experimental part of publication [17], section 4.2). For the positron annihilation lifetime measurements sample pairs of the produced alloys CrFeNi (0.3:1:0.2), CrFeNi(1:1:1), CoCrFeNi (1:1:1:1), AlCoCrFeNi (0.3:1:1:1:1) and CoCrFeMnNi (1:1:1:1:1) were cut and ground (grit-paper grade 1000). All of the samples show a face-centered cubic crystal structure, but they show an increasing mixing entropy with increasing number of constituents. The exact compositions as obtained from energy-dispersive X-ray spectroscopy (EDX) composition maps and the lattice constants as obtained from X-ray diffraction (XRD) measurements of all samples are shown in table 3.2 (see also section 4.2 and ref. [17]).

Table 3.2: Concentrated solid-solution alloy samples: Alloy compositions in at.% as obtained from EDX composition maps and lattice constants as obtained from XRD measurements. The error of the alloy composition is determined to ±0.20 at.%, the error of the lattice constant is 0.001 Å.

Alloy	Al	Co	Cr	Fe	Mn	Ni	Lattice constant a/ Å
CrFeNi (0.3:1:0.2)	-	-	19.2	68.2	-	12.6	3.581
CrFeNi (1:1:1)	-	-	34.1	33.0	-	32.9	3.560
CoCrFeNi (1:1:1:1)	-	24.9	25.5	24.9	-	24.7	3.570
AlCoCrFeNi (0.3:1:1:1:1)	6.0	23.6	23.9	23.4	-	23.1	3.588
CoCrFeMnNi (1:1:1:1:1)	-	20.2	20.5	20.1	19.5	19.7	3.596

Prior to any positron annihilation lifetime spectroscopy measurements all samples were sealed in evacuated quartz ampules and subject to high temperatures (1493 K), close to

their onset of melting for approximately 30 minutes before they were rapidly quenched in ice-water. All samples were stored in liquid nitrogen immediately after quenching until they were mounted in the lifetime spectrometer where measurements were conducted during cooling the samples to 205 K. For a more detailed explanation of the heat treatments and measurement procedures see the experimental part of publication [17] (section 4.2).

4 | Publications

Overview: The peer-reviewed published articles presented in the following constitute the main part of this thesis. The four articles given in sections 4.1 and 4.2 include experimental studies applying positron-electron annihilation techniques on the material classes of light weight alloys and concentrated solid-solution alloys. Furthermore, the two articles included in section 4.3 comprise theoretical studies on the trapping and annihilation of positrons in small extended defects such as precipitates and at interfaces between the matrix and cylindrical or spherical precipitates modeled by diffusion-reaction theory.

In article 1 (section 4.1.1, ref. [8]) the precipitation sequence occuring during artificial aging in the commercial light weight alloy AW 6060 is studied applying *ex situ* positron annihilation lifetime spectroscopy and dilatometry as a complimentary technique. It comprises results on the evolution of precipitates for different timescales, from initial clustering stages to the overaged regime, and for two different artificial aging temperatures, 180°C and 210°C.

In article 2 (section 4.1.2, ref. [9]) temperature-dependent positron annihilation lifetime spectroscopy was utilized to identify different types of positron traps occuring at different stages of the precipitation sequence of the alloy AW 6060.

In article 3 (section 4.1.3, ref. [10]) the authors presented *in-situ* measurements of the positron annihilation Doppler broadening S-parameter during artificial aging at 180°C and 210°C and during a subsequent solution heat treatment of a previously overaged sample. The obtained *in situ* results measured at high temperatures were analyzed and interpreted in comparison to the *ex situ* measurements at low temperatures as conducted in the framework

of articles 1 and 2.

In article 4 (section 4.2, ref. [17]) the authors focused on the rather new material class of concentrated solid-solution alloys, often referred to as high-entropy alloys. Applying positron annihilation lifetime spectroscopy the concentration of quenched-in thermal vacancies for a set of face-centered cubic alloys with varying entropy of mixing ΔS_{mix} was determined.

In article 5 (section 4.3, ref. [11]) the exact solution of a diffusion-reaction model for the trapping and annihilation of positrons in small extended spherical defects, such as voids, clusters and small precipitates was presented.

In article 6 (section 4.3, ref. [12]) the diffusion-reaction model was solved for trapping and annihilation of positrons at interfaces between matrix and cylindrical or spherical precipitates. In both cases, closed-form expressions are obtained for the mean positron lifetime and the intensities of the lifetime components associated with the trapped states.

In the following a short preamble is included for each publication with a clear specification of the contributions from each author, as it is required for a cumulative thesis. These preambles also serve to highlight the most important details of each work and incorporate transitions and coherences between the individual articles.

4.1 Artificial aging of the commercial Al–Mg–Si alloy AW 6060

4.1.1 Article 1: Positron annihilation lifetime spectroscopy and dilatometry for the study of the precipitation sequence on different timescales and in different temperature regimes

Preamble: The article *Precipitation processes in Al–Mg–Si extending down to initial clustering revealed by the complementary techniques of positron lifetime spectroscopy and dilatometry* was published in Journal of materials science **53** (14657-14665), June 2018 [8].

This work was done by Laura Resch and Gregor Klinser as shared first authors. They performed the experimental work, analysis and interpretation of the positron lifetime spectroscopy measurements, wrote the manuscript and edited the final version together with the co-authors. The preparation of the dilatometry samples, dilatometry measurements and data analysis were performed by Elisabeth Hengge, Robert Enzinger and Martin Luckabauer. The experimental progress and the writing process were supervised by Wolfgang Sprengel and Roland Würschum.

The presented results on the precipitation sequence during artificial aging of a commercial light weight alloy were obtained by the joint application of the complimentary techniques of positron annihilation lifetime spectroscopy and dilatometry. Each positron lifetime datapoint stems from an individual sample pair, prepared in a well-defined aging state prior to the measurement. During the data acquisition, the samples are kept at low temperatures, which allows to keep each sample in its respective aging state during the measurement. This procedure allows to analyze artificial aging explicitly, by preventing superimposed natural aging effects, without having to sacrifice for high statistics and measurement accuracies. It is thus possible to resolve the atomistic processes not only after longer aging times but also during the very early clustering stages.

Metals

CrossMark

Precipitation processes in Al–Mg–Si extending down to initial clustering revealed by the complementary techniques of positron lifetime spectroscopy and dilatometry

L. Resch[1,*] , G. Klinser[1] , E. Hengge[1] , R. Enzinger[1] , M. Luckabauer[1,2] , W. Sprengel[1] , and R. Würschum[1]

[1] *Institute of Materials Physics, Graz University of Technology, Petersgasse 16, 8010 Graz, Austria*
[2] *Institute for Materials Research, Tohoku University, 2-1-1 Katahira, Aoba-ku, Sendai 980-8577, Japan*

ABSTRACT

The design of specific material properties of aluminum alloys demands for a detailed understanding of clustering and precipitation processes occurring during heat treatments. Positron lifetime spectroscopy in combination with high-precision dilatometry measurements were taken, allowing for a comprehensive analysis of the aging mechanisms occurring on different timescales and in different temperature regimes, during artificial aging. From the results, unambiguous experimental evidence for the following three main steps of the precipitation process is obtained. In the first seconds of artificial aging, a competitive process of dissolution and growth of different cluster types occurs. Subsequently, clusters start to transform into coherent precipitates, which are mainly responsible for the hardening effect. For prolonged artificial aging, the number density of the coherent precipitates increases, while positron lifetime spectroscopy already reveals the simultaneous formation of less coherent precipitates.

Introduction

Age hardenable aluminum alloys with the main solutes being Si and Mg (6xxx series) find increasing applications within a wide range of sectors, e.g., in automotive industry [1] as car body parts as well as for architectural and structural applications [2] such as fences or flooring. Al–Mg–Si alloys obtain their maximum hardness by prolonged storage at elevated temperatures, a process referred to as artificial aging. During artificial aging, precipitates grow within the Al matrix, serving to harden the material. Although this heat treatment methods have been known for a

Springer

long time [3, 4], the details of the precipitation sequence prior to formation of the final equilibrium phase β are still point of discussions [5, 6]. A generally agreed model is the following precipitation sequence [7]:

SSSS → Si-, Mg- clusters → $\beta'' → \beta'/U_1/U_2/B' → \beta$
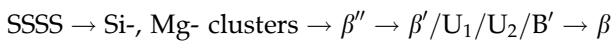
Here, SSSS denotes the supersaturated solid solution and β'', β', U_1, U_2, and B′ are metastable precipitates prior to the equilibrium phase β [7]. While β'' precipitates are coherent to the Al matrix, β', U_1 and U_2 precipitates are semi-coherent [8] and β precipitates are incoherent [9–11]. Due to their coherence, β'' precipitates give the major contribution to the age hardening of the alloy; consequently, they are predominant in the peak-aged microstructure [12]. The number density of β'' precipitates, and thus, the maximum achievable hardness is strongly influenced by the parameters of the temperature treatment and the corresponding nucleation, i.e., initial clustering stages. For example, aging at 210 °C results in lower hardness due to a reduced number density of β'' precipitates compared to aging at 180 °C [13]. Furthermore, prolonged room temperature storage before artificial aging can have a negative effect on the formation of β'' precipitates [14]. Hence, for tailoring the hardening response and further material properties of aluminum alloys, it is inevitable to obtain a detailed understanding of the initial clustering stages as well as of the further steps of the precipitation sequence.

In particular, the observation of initial clusters is challenging due to several facts. Early clusters usually only involve few atoms, and moreover, these processes take place on very short timescales. Furthermore, the distinct clustering stages are complex and often overlapping in time. Common methods for the study of precipitation processes are atom probe tomography (APT), transmission electron microscopy (TEM), or differential scanning calorimetry (DSC). However, these methods encounter several difficulties in the case of the investigation of Al alloys: Initial clustering stages, consisting of a few atoms, are on the lower limit or even below the detectability of APT [15]. The similar electronic structure of Mg, Si and Al results in a very low contrast in TEM imaging; thus, early clustering stages can hardly be resolved. The quantitative analysis of non-isothermal DSC is difficult due to the complex precipitation process [16, 17]

while for isothermal DSC the detection limit of the heat flow is easily reached.

Yet another technique namely dilatometry can monitor the length change of a sample in situ during artificial aging. The applicability of this technique for the observation of precipitation processes has been demonstrated on steels and special alloys [18–20]. Still, length changes during aging in the most aluminum alloys, especially in AW6060, are very small which can be a problem for most of today's commercially available dilatometers [21]. Our self-developed high-precision dilatometer already proved being capable of monitoring these small length changes during isothermal, in situ aging of AW6060 [13]. Nevertheless, the length change only reacts to the precipitation process after longer aging times (from ≈ 1000 s onwards), this requires a complementary technique which is suitable to monitor also very early clustering stages.

A powerful tool to investigate precipitation processes in light alloys is positron annihilation lifetime spectroscopy (PLS) [22]. Positrons are sensitive to the free volume of precipitates, allowing to register changes in microstructure as for example transitions from coherent to semi- or incoherent precipitates. The greatest benefit of this method, however, is that even small clusters and precipitates, that do not cause additional free volume, act as an attractive potential for positrons. This is due to the fact that typical alloying elements show higher positron affinities than the Al matrix [11, 23, 24]. Thus, positrons are capable of sensing the very early clustering stages after seconds of aging, but also structural changes after several hours of aging as for example the transition from β'' to β'. In recent years, several groups studied the formation of precipitates during age hardening of Al alloys by means of positron annihilation spectroscopy. The group of Banhart conducted in situ PAS measurements in combination with electrical resistivity, DSC and hardness measurements on Al–Mg–Si alloys mostly during *natural aging* [25–27]. These studies included only few e^+-lifetime data points measured at room temperature after artificial aging [28]. Therefore, the results are only valid for artificial aging effects superimposed by natural secondary aging. Furthermore, Staab et al. conducted comprehensive studies concerning lightweight alloys analyzed by PAS. The main aspect of these measurements was the *natural aging* of lightweight alloys

including copper additions studied by lifetime spectroscopy applying different temperatures during the measurement [29, 30]. The novelty in this study now is positron lifetime spectroscopy combined with high-precision dilatometry to analyze explicitly *artificial aging* of the commercial Al alloy AW6060 at 180 and 210 °C. In addition to the enormous accuracy of the applied dilatometer, the positron spectrometer setup includes the possibility to cool down the sample to temperatures far below room temperature, allowing to freeze the system in its defined aging state during the data acquisition times, which for precise data analysis are longer than the short initial clustering times. This novel and unique joint application of dilatometry and e^+ spectroscopy is the ideal technique for the experimental observation of the atomistic precipitation processes in lightweight alloys, allowing a comprehensive analysis of the precipitation sequence within different time scales and temperature regimes.

Experimental

The material of interest in this study was a commercial-grade AW6060 Al alloy, in a T6 state[1] in the as-received condition. All investigated samples were obtained from the same low-alloyed batch and were rich in magnesium (0.65 at.% Mg, 0.52 at.% Si). Prior to any aging experiments, all samples were solution heat-treated at (540 ± 1) °C for 30 min and subsequently quenched to room temperature.

A sketch of the heat treatment applied to the PLS samples is shown in Fig. 1. After solution heat treatment and quenching, the PLS samples were kept at room temperature for 4 min before artificial aging in a dry box at (180 ± 1) °C or (210 ± 1) °C for a defined period of time (between 10 and 1.14×10^6 s). To achieve a consistent heating and isothermal annealing throughout the experiment, the finely ground samples were put onto an isothermal aluminum plate ($335 \times 60 \times 10$ mm^3) inside the dry box. Consequently, it became possible to estimate the heat-up time under the assumption that the cooling effect on the aluminum plate can be neglected[2]. To

---

[1] T6 heat treatment: solution heat treatment and peak aging of the alloy.

[2] Note, that all aging times are net aging times that do not include the first 60 s, as this is the estimated heat-up time of the samples in the drying oven
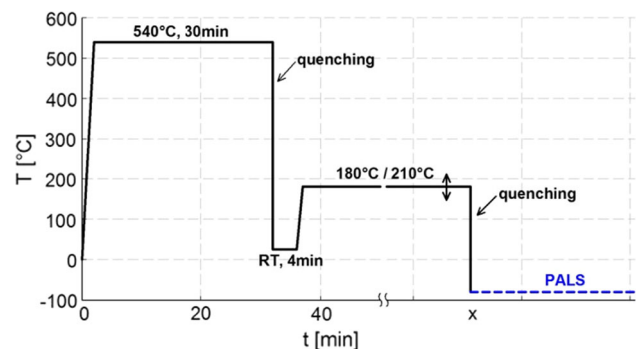
Figure 1 Schematic sketch of the heat treatment of the AW6060 samples prior to positron annihilation lifetime spectroscopy (PLS).

prevent secondary natural aging, the samples were cooled to liquid nitrogen temperatures immediately after artificial aging.

For the positron lifetime measurements, pairs of square shaped samples ($1.5 \times 10 \times 10$ mm^3) with identical heat treatment were used. These identical samples were removed from the liquid nitrogen bath, and a ^{22}Na source (encapsulated in aluminum foil) was sandwiched between them. The source-sample sandwich arrangement was transferred to a helium cryostat and cooled to − 73 °C. The sample handling time between removal from the liquid nitrogen bath until reaching subzero temperatures in the helium cryostat of the lifetime spectrometer was approximately 1 min. The positron lifetime measurements were taken using a digital positron lifetime spectrometer obtaining a full width at half maximum of the time resolution function of 163 ps. Each lifetime spectrum contained more than 10^6 counts and was analyzed after background and source correction using the program PALSFit [31]. Note that each positron lifetime data point stems from one separate pair of samples, the two platelets of each pair being treated identically. Thus, in total the present study is based on more than 70 sample pairs.

In addition to positron lifetime spectroscopy, in situ dilatometry was performed as a complementary method applying a self-developed high-stability laser dilatometer with an incremental length resolution of 20 pm [32]. The samples for dilatometry measurements were solution heat-treated and quenched inside the dilatometer. For quenching to room temperature, a He gas stream was applied. Four minutes after quenching, the samples were artificially aged at 180 and 210 °C, respectively. For a detailed description of the measurement procedure, the

reader is referred to Ref. [13]. For additional characterization, Brinell hardness was measured with an EMCO-TEST DuraJet hardness tester, using the Brinell method. The measurements were taken at room temperature immediately after the artificial aging in the dry box. Each hardness value is a mean of five measurements, obtained from one square-based sample ($4 \times 10 \times 10$ mm^3). To be consistent with e^+ annihilation measurements, samples for hardness measurements were kept at room temperature for 4 min after solution heat treatment and prior to artificial aging.

Results and discussion

Three main steps are identified in the precipitation process from the comparison of the PLS data with the relative length change and the well known hardness response during aging at 180 °C (Fig. 2a), and 210 °C (Fig. 2b). In the first step (time span A: 10–100 s for 180 °C and 10–1200 s for 210 °C), both aging temperatures reveal the same characteristics in the positron annihilation data. The positron lifetime spectra are best fitted using a two-component analysis with the components τ_0 and τ_1 and the corresponding relative intensities $I_0 = 1 - I_1$ and I_1. The shorter component τ_0 characterizes e^+ annihilation from the free state (see "Quenched sample" section) and the longer component τ_1 is due to e^+ annihilation from a defect-trapped state as specified in more detail below. τ_1 decreases from 227 ps to about 214 ps as soon as the samples are heated to the artificial aging temperatures and it stays almost constant with proceeding aging time (see Fig. 3a). While τ_1 does not vary within time span A the corresponding intensity I_1 shows a slight decrease until $\approx$ 30 s ($\approx 10^2$ s) for 180 °C (210 °C) of aging temperature and then increases again until it reaches 100% at the end of time span A (see Fig. 3c). From this point onwards (time span B plus C), the most reasonable fit of the lifetime spectra is obtained by using only one lifetime component.

Time span B is characterized by the constant mean e^+ lifetime $\tau_{mean} = I_0\tau_0 + I_1\tau_1$, which is the case for artificial aging at 180 °C up to 10^4 s (Fig. 2a). Contrary, during aging at 210 °C the value for τ_{mean} increases continuously from 1000 s onwards (Fig. 2b). The underlying precipitation processes

correspond to time span C of the sequence as outlined below.

The length change as well as the hardness continuously increases from 10^2 to 10^3 s onwards for 180 and 210 °C of aging temperature, respectively. Within interval C, the hardness and dilatometry values reach their maximum and subsequently decrease again for both aging temperatures. As soon as time span C is also reached for 180 °C of aging temperature (10^4 s, Fig. 2), PLS data show the same monotonous increase as observed for 210 °C already after 10^2 s of aging. Toward the end of time span C, the value of τ_{mean} shows no tendency of levelling off. It should be pointed out once more that each PLS data point in the measuring sequence corresponds to a different set of sample pair. Therefore, the very small scattering of the data reflects the remarkable statistical reliability and reproducibility of the experimental results.

The following discussion is separated into four parts: the analysis of the quenched sample as well as the analysis of the time spans A, B and C, corresponding to the three main precipitation steps for 180 and 210 °C.

Quenched sample

For the quenched sample, with corresponding data displayed as gray crosses in Figs. 2 and 3, the positron lifetime spectrum can be best described with two lifetime components. This is consistent with an incomplete positron trapping during the first 5 min of natural aging as also observed by Klobes et al. [29]. This is reasonable as the quenched samples were exposed to room temperature for 4 min prior to the start of the positron annihilation measurements.

The obtained shorter lifetime component $\tau_0 = 46$ ps arises from $e^+ - e^-$ annihilations within the bulk of the alloy; τ_0 is reduced due to the presence of defects [33]. It should be noted that the bulk lifetime $\tau_b = (I_0/\tau_0 + I_1/\tau_1)^{-1}$ of 179 ps (see Fig. 3b), which is calculated according to the simple two-state trapping model, is somewhat higher than that in pure Al ($\tau_{b_{Al}} = 163$ ps [34]). The longer lifetime component of the quenched sample $\tau_1 = 230$ ps (Fig. 3a) is lower than the lifetime of a positron in an Al vacancy ($\tau_{V_{Al}} = 248$ ps, even if a solute is attached to it [25]), although after 4 min of natural aging a sufficient amount of vacancies is still present in the alloy [35].

Figure 2 Mean positron lifetime τ_{mean} (**a** 180 °C, blue circles; **b** 210 °C, red circles), relative length change $\Delta L/L$ (black line) and the corresponding hardness values HBW (green triangles) during artificial aging. The gray cross represents the mean positron lifetime of the as-quenched sample (AQ).
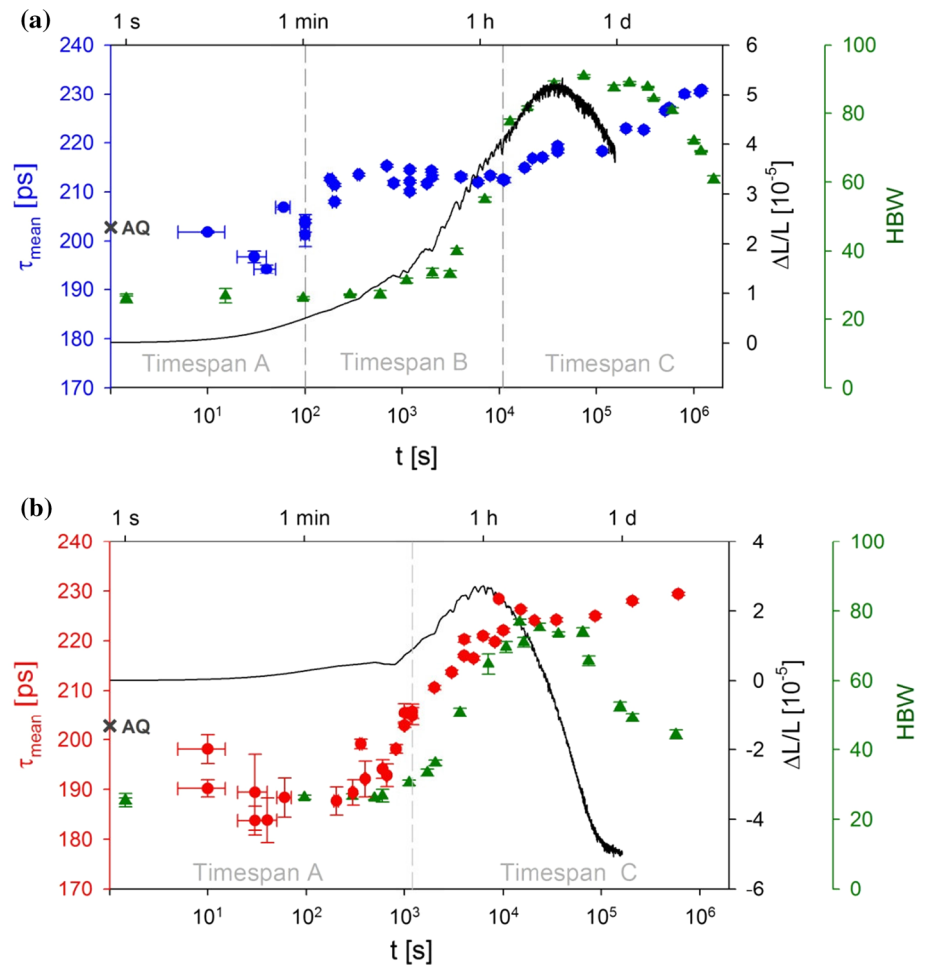
On the other hand, the value of τ_1 is higher than the positron lifetime in solute clusters (210–220 ps [26]). Such clusters already form during quenching or within the first minutes at room temperature after quenching [36, 37] and also act as an attractive potential to positrons [11, 23, 24]. The positron lifetime within clusters and within vacancies cannot be resolved separately. Therefore, τ_1 of the quenched sample is a trapping rate averaged mean value of two e^+ lifetimes, one corresponding to e^+ annihilations within vacancies, the second one corresponding to annihilation within clusters.

Time span A: dissolution of natural aging clusters and formation of artificial aging clusters

The first main step of the precipitation process upon artificial aging (time span A) is characterized by two-component fits of the corresponding lifetime spectra. The short lifetime component ($\tau_0 \leq 105$ ps, for all samples) is attributed to annihilations within the bulk of the alloy (see Fig. 3b for the calculated bulk lifetime).

The decrease of τ_1 with the onset of aging can be explained by annealing out of vacancies, as it was observed for natural aging, but on a longer timescale [35]. Although vacancies anneal out, the intensity of τ_1 increases after 10 s of artificial aging (see Fig. 3c). This indicates that new positron traps, i.e., clusters, are formed simultaneously. For aging times between 10 s and the end of time span A, the lifetime component τ_1 stays almost constant around a value of $\tau_1 = 214$ ps, which is in the range of the lifetime reported in the literature for positrons within clusters [26]. The corresponding intensity I_1, i.e., the amount of trapped positrons, shows a slight decrease until ≈ 30 s (10^2 s) for 180 °C (210 °C) of aging temperature.

A decrease in the amount of trapped positrons after the initial increase appears odd at first sight as artificial aging should result in a continuous growth
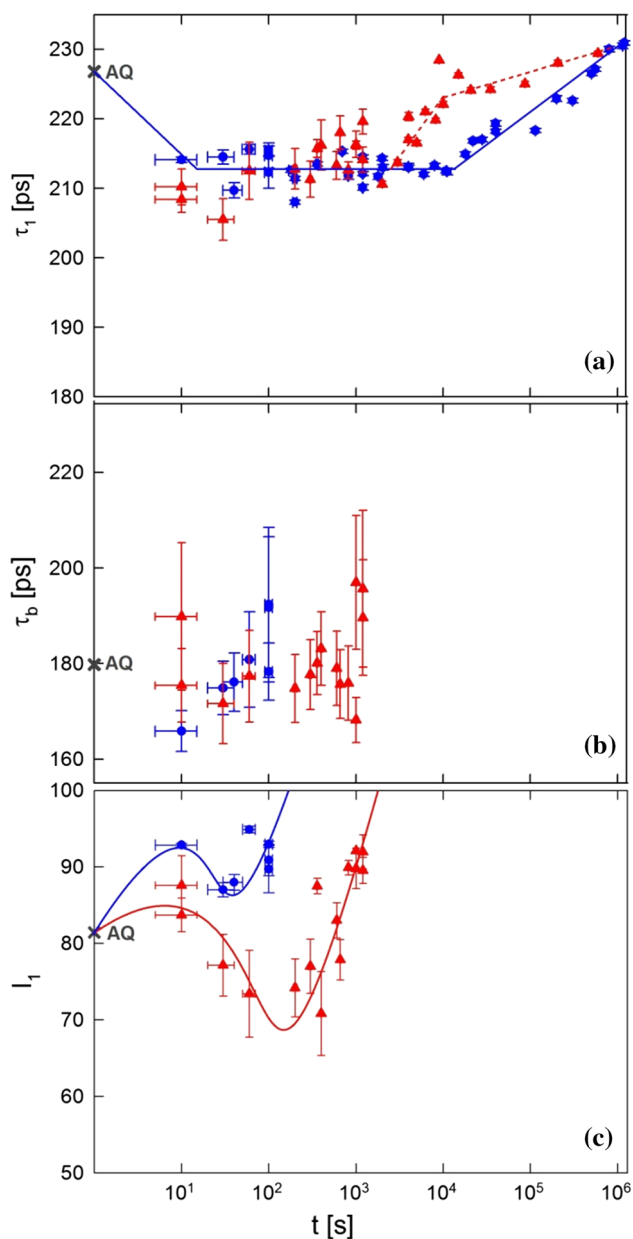
Figure 3 Results of the positron lifetime spectroscopy measured on Al–Mg–Si upon aging at 180 °C (blue circles) and 210 °C (red triangles) in dependence of the artificial aging time. **a** Long lifetime component (τ_1). Note that for time spans B and C, τ_1 is equal to τ_{mean} (see Fig. 2), **b** calculated bulk lifetime (τ_b) and **c** intensity I_1 of lifetime component τ_1. The gray crosses (AQ, left-scale axis) represent the as-quenched sample. The lines are for guiding the eyes.

of the number density of clusters. However, the samples were kept at room temperature for 4 min before artificial aging, which is a sufficient amount of time for the formation of natural aging clusters [29]. Previous studies showed that natural aging clusters differ from clusters formed by artificial aging [38]. Thus, while artificial aging clusters continue to grow in number density, smaller natural aging clusters dissolve [16, 39]. As long as the dissolution of natural aging clusters is the dominant process this leads to a decrease in the value of I_1. Consequently, more positrons annihilate in the bulk of the material, lowering the mean positron lifetime (see Fig. 2a, b).

For artificial aging times longer than 30 s (180 °C) and 100 s (210 °C), I_1 increases again, i.e., the formation of artificial aging clusters dominates over the dissolution of natural aging clusters. At the end of time span A, all positrons are trapped within solute clusters; the optimum fit of the lifetime spectra is received using only one lifetime component from this point onwards.

Even if the overall trends of the positron lifetime data are similar for both aging temperatures in time span A, a remarkable difference can be observed. The decrease of I_1 is more pronounced and shifted to higher aging times in the case of 210 °C. This reflects a lower number density of artificial aging clusters for 210 °C compared to 180 °C, owing to a reduced cluster nucleation rate at the higher aging temperatures [40]

Time span B: growth of β'' precipitates

In time span B, the positron lifetime analysis reveals a single lifetime component; saturation trapping of positrons into previously formed clusters occurs. This defines a lower limit of the cluster concentration C according to the condition $\sigma \times C \gg \frac{1}{\tau_b}$ required for e^+ saturation trapping, where σ denotes the specific trapping rate of the positrons. The cluster number density N after a comparable aging step (170 °C, 1200 s) has been determined to $N = 4.4 \times 10^{23}$ m^{-3} by atom probe characterization. In fact, this number density is compatible with saturation trapping of e^+ taking into account typical values for the specific e^+ trapping rate σ.

An ideal complementary technique in this regime of e^+ saturation trapping is dilatometry. In this time span, dilatometry shows a length increase, indicating a continuation of the precipitation process. An increase in length change corresponds to a predominant contribution of coherent β'' precipitates while a decrease would correspond to the predominant contribution of semi-coherent β' precipitates [13]. Thus,

clusters keep growing in size and eventually transform into β'' precipitates. This is also confirmed by the increase in hardness in this time span (see Fig. 2a) as it is well known that the strengthening process is mainly governed by β'' precipitates [36, 41].

Although, from dilatometry and hardness measurements, it is derived that clusters start to transform into β'' precipitates, the positron lifetime stays constant in time span B at 180 °C (see Fig. 3a). This shows that clusters and β'' precipitates have a similar defect-related free volume size which is in line with the fact that both the clusters and the β'' precipitates are coherent with the Al matrix.

For an aging temperature of 210 °C, no region of constant τ_1 can be observed. A period of continuously increasing τ_1 directly follows after time span A, as it will be discussed in the following section.

Time span C: transformation of β'' to β' precipitates

Within time span C, the single positron lifetime component τ_1 continuously increases for both artificial aging temperatures. This now indicates the onset of the formation of β' precipitates with an enhanced defect-related free volume associated with the incoherent interfaces. In fact, as an increasing fraction of coherent β'' precipitates transforms to semi-coherent β' precipitates, the lifetime component τ_1 has to be considered as an average value of the lifetime of e^+ annihilating within β'' precipitates ($\tau_{\beta''}$) and those that annihilate within β' precipitates ($\tau_{\beta'}$), i.e.,:

$$\tau_1 = \frac{\sigma_{\beta''} C_{\beta''} \tau_{\beta''} + \sigma_{\beta'} C_{\beta'} \tau_{\beta'}}{\sigma_{\beta''} C_{\beta''} + \sigma_{\beta'} C_{\beta'}}. \qquad (1)$$

Due to the semi-coherent structure of β' precipitates, the value for $\tau_{\beta'}$ is higher than for $\tau_{\beta''}$. Within time span C the concentration $C_{\beta'}$ of semi-coherent precipitates increases, which leads to an increase of the e^+ lifetime τ_1 (see Eq. 1). Even if $C_{\beta''}$ decreases, the condition for saturation trapping (here: $(\sigma_{\beta''} \times C_{\beta''} + \sigma_{\beta'} \times C_{\beta'}) \gg \frac{1}{\tau_b}$) is still valid.

The fact that for the higher aging temperature of 210 °C τ_1 increases right after time span A shows that β'' precipitates transform earlier into β' precipitates compared to 180 °C.

This difference in the temporal sequence of the precipitation process is also shown by the shift of the maximum in the $\frac{4L}{L}$-curve and hardness curve toward lower times (compare Fig. 2a, b). For both aging temperatures, the hardness and the length change continue to increase until reaching their maxima corresponding to the formation of β'' precipitates. For aging times longer than 3.7×10^4 s (1.2×10^4 s) at a temperature of 180 °C (210 °C), the hardness decreases just as the length change in the sample does indicating that the contribution of β' to the overall precipitates starts to dominate.

It is important to point out, however, that the positron lifetime monitors the formation of β' precipitates already at the beginning of time span C by its continuous increase. In this sense, positron data give more conclusive and earlier hints on the formation of β' precipitates than dilatometry and hardness. Only by the combination with dilatometry and hardness measurements, it can be decisively concluded that the processes of β'' and β' formation proceed simultaneously.

Summary and conclusion

The atomistic processes during artificial aging at distinct temperatures of a commercial Al alloy are analyzed using positron lifetime spectroscopy (PLS) and dilatometry accompanied by hardness measurements. According to the positron annihilation characteristics, the precipitation process can be divided into three time regimes, labeled as time spans A, B, C (corresponding to up to 1 min, up to 1 h, and more than 1 h for 180 °C, respectively).

Within the first period of aging (time span A), cluster number densities as well as the sizes of these clusters are below the detection limit of dilatometry or hardness. Only the sensitivity of e^+ annihilation spectroscopy enables to monitor these early stages of the precipitation process. The variations of the intensity of the positron lifetime indicate a competing process of the dissolution of natural aging clusters and the concurrent formation of artificial aging clusters. This behavior is more pronounced in the case of 210 °C due to a lower cluster nucleation rate. With preceding aging times, artificial aging clusters grow in number density and eventually transform into β'' precipitates (time span B) as evidenced by an increase in length change and hardness. The clusters and β'' precipitates are characterized, however, by a similar defect-related free volume size as shown by the constant e^+ lifetime in this regime.

For long aging times (time span C), the defect-related free volume increases for both aging temperatures supporting the results of dilatometry and hardness according to which in this regime β'' precipitates transform into semi-coherent β' precipitates.

The present study demonstrates that the information on the precipitation process is accessible only by the unique joint application of the two complementary methods of positron annihilation and dilatometry. For the analysis of the early clustering stages, only PLS is sensitive enough, while for longer aging times only by the assistance of dilatometry the final conclusive hint on the transformation of precipitates is obtained.

Acknowledgements

Compliance with ethical standards

Conflict of interest Herewith all authors certify that there is no actual or potential conflict of interest in relation to this article.

References

[1] Miller WS, Zhuang L, Bottema J, Wittebrood AJ, De Smet P, Haszler A, Vieregge A (2000) Recent development in aluminium alloys for the automotive industry. Mater Sci Eng A Struct 280(1):37–49

[2] Zhang XH, Su GC, Ju CW, Wang WC, Yan WL (2010) Effect of modification treatment on the microstructure and mechanical properties of Al–0.35%Mg–7.0%Si cast alloy. Mater Des 31(9):4408–4413

[3] Wilm A (1911) Physikalisch-metallurgische Untersuchungen über magnesiumhaltige Aluminiumlegierungen. Metallurgie: Zeitschrift für de gesamte Hüttenkunde 8:225–227

[4] Duprac OH (2005) Alfred Wilm and the beginnings of Duralumin. Z Metallkd 96(4):398–404

[5] Ringer SP, Hono K (2000) Microstructural evolution and age hardening in aluminium alloys: atom probe field-ion microscopy and transmission electron microscopy studies. Mater Charact 44(1):101–131

[6] Starink MJ (2004) Analysis of aluminium based alloys by calorimetry: quantitative analysis of reactions and reaction kinetics. Int Mater Rev 49(3–4):191–226

[7] Marioara CD, Andersen SJ, Zandbergen HW, Holmestad R (2005) The influence of alloy composition on precipitates of the Al–Mg–Si system. Metall Mater Trans A 36(3):691–702

[8] Frøseth Anders G, Høier Ragnvald, Derlet Peter M, Andersen Sigmund J, Marioara Calin D (2003) Bonding in MgSi and Al–Mg–Si compounds relevant to Al–Mg–Si alloys. Phys Rev B 67:224106-1–224106-11

[9] Ostermann Friedrich (2015) Anwendungstechnologie aluminium, 3rd edn. Springer, Berlin

[10] Andersen SJ, Marioara CD, Frøseth A, Vissers R, Zandbergen HW (2005) Crystal structure of the orthorhombic U2-$Al_4Mg_4Si_4$ precipitate in the Al–Mg–Si alloy system and its relation to the β' and β'' phases. Mater Sci Eng A Struct 390(1):127–138

[11] Staab TEM, Krause-Rehberg R, Hornauer U, Zschech E (2006) Study of artificial aging in AlMgSi (6061) and AlMgSiCu (6013) alloys by positron annihilation. J Mater Sci 41(4):1059–1066. https://doi.org/10.1007/s10853-005-3640-x

[12] Zandbergen MW, Xu Q, Cerezo A, Smith GDW (2015) Study of precipitation in Al–Mg–Si alloys by atom probe tomography I. Microstructural changes as a function of ageing temperature. Acta Mater 101(Supplement C):136–148

[13] Luckabauer M, Hengge E, Klinser G, Sprengel W, Würschum R (2017) In situ real-time monitoring of aging processes in an aluminum alloy by high-precision dilatometry. Springer, Berlin

[14] Martinsen FA, Ehlers FJH, Torsæter M, Holmestad R (2012) Reversal of the negative natural aging effect in Al–Mg–Si alloys. Acta Mater 60(17):6091–6101

[15] Torsæter M, Hasting HS, Lefebvre W, Marioara CD, Walmsley JC, Andersen SJ, Holmestad R (2010) The influence of composition and natural aging on clustering during preaging in Al–Mg–Si alloys. J Appl Phys 108(7):073527-1–073527-9

[16] Gupta AK, Lloyd DJ (1999) Study of precipitation kinetics in a super purity Al–0.8 pct Mg–0.9 pct Si alloy using

differential scanning calorimetry. Metall Mater Trans A 30(13):879–890

[17] Daoudi MI, Triki A, Redjaimia A, Yamina C (2014) The determination of the activation energy varying with the precipitated fraction of β'' metastable phase in an Al–Si–Mg alloy using non-isothermal dilatometry. Thermochim Acta 577(Supplement C):5–10

[18] Garcia-Mateo C, Caballero FG, Capdevila C, Garcia de Andres C (2009) Estimation of dislocation density in bainitic microstructures using high-resolution dilatometry. Scr Mater 61(9):855–858

[19] Grajcar A, Zalecki W, Skrzypczyk P, Kilarski A, Kowalski A, Kołodziej S (2014) Dilatometric study of phase transformations in advanced high-strength bainitic steel. J Therm Anal Calorim 118(2):739–748

[20] Recarte V, Pérez-Sáez R, No M, Juan S (1997) Dilatometric study of the precipitation kinetics in Cu–Al–Ni shape memory alloys. J Phys IV 07:C5-329–C5-334

[21] Milkereit Benjamin, Reich Michael, Kessler Olaf (2017) Detection of quench induced precipitation in Al alloys by dilatometry. Mater Sci Forum 877:147–152

[22] Dupasquier A, Kögel G, Somoza A (2004) Studies of light alloys by positron annihilation techniques. Acta Mater 52(16):4707–4726

[23] Dlubek G (1987) Positron studies of decomposition phenomena in Al alloys. Mater Sci Forum 13:11–32

[24] Puska MJ, Lanki P, Nieminen RM (1989) Positron affinities for elemental metals. J Phys Condens Mater 1(35):6081–6093

[25] Banhart J, Lay MDH, Chang CST, Hill AJ (2011) Kinetics of natural aging in Al–Mg–Si alloys studied by positron annihilation lifetime spectroscopy. Phys Rev B 83(1):014101-1–014101-13

[26] Liu M, Čížek J, Chang CST, Banhart J (2015) Early stages of solute clustering in an Al–Mg–Si alloy. Acta Mater 91:355–364

[27] Banhart J, Chang CST, Liang Z, Wanderka N, Lay MDH, Hill AJ (2010) Natural aging in Al–Mg–Si alloys—a process of unexpected complexity. Adv Eng Mater 12(7):559–571

[28] Banhart J, Liu M, Yong Y, Liang Z, Chang CST, Elsayed M, Lay MDH (2012) Study of ageing in Al–Mg–Si alloys by positron annihilation spectroscopy. Physica B 407(14):2689–2696

[29] Klobes B, Staab TEM, Haaks M, Maier K, Wieler I (2008) The role of quenched-in vacancies for the decomposition of aluminium alloys. Phys Status Solidi R 2(5):224–226

[30] Klobes B, Maier K, Staab TEM (2015) Early stage ageing effects and shallow positron traps in Al–Mg–Si alloys. Philos Mag 95(13):1414–1424

[31] Olsen JV, Kirkegaard P, Pedersen NJ, Eldrup M (2007) Palsfit: a new program for the evaluation of positron lifetime spectra. Phys Status Solidi R 4(10):4004–4006

[32] Luckabauer M, Sprengel W, Würschum R (2016) A high-stability non-contact dilatometer for low-amplitude temperature-modulated measurements. Rev Sci Instrum 87(7):075116-1–075116-7

[33] Krause-Rehberg R, Leipner HS (1999) Positron annihilation in semiconductors. Springer, Berlin

[34] Schaefer HE, ugelmeier R, chmolz M, Seeger A (1987) Positron lifetime spectroscopy and trapping at vacancies in aluminium. In: Schaefer HE, Gugelmeier R, Schmolz M, Seeger A (eds) Materials science forum, vol 15, Trans Tech Publications, pp 111–116

[35] Werinos M, Antrekowitsch H, Ebner T, Prillhofer R, Uggowitzer PJ, Pogatscher S (2016) Hardening of Al–Mg–Si alloys: effect of trace elements and prolonged natural aging. Mater Des 107:257–268

[36] Edwards GA, Stiller K, Dunlop GL, Couper MJ (1998) The precipitation sequence in Al–Mg–Si alloys. Acta Mater 46(11):3893–3904

[37] Murayama M, Hono K, Saga M, Kikuchi M (1998) Atom probe studies on the early stages of precipitation in Al–Mg–Si alloys. Mater Sci Eng A Struct 250(1):127–132

[38] Serizawa A, Hirosawa S, Sato T (2008) Three-dimensional atom probe characterization of nanoclusters responsible for multistep aging behavior of an Al–Mg–Si alloy. Metall Mater Trans A 39(2):243–251

[39] Gupta AK, Lloyd DJ, Court SA (2001) Precipitation hardening in Al–Mg–Si alloys with and without excess Si. Mater Sci Eng A Struct 316(1):11–17

[40] Pashley DW, Jacobs MH, Vietz JT (1967) The basic processes affecting two-step ageing in an Al–Mg–Si alloy. Philos Mag A J Theor Exp Appl Phys 16(139):51–76

[41] Murayama M, Hono K (1999) Pre-precipitate clusters and precipitation processes in Al–Mg–Si alloys. Acta Mater 47(5):1537–1548

4.1.2   Article 2: Temperature-dependent positron annihilation lifetime spectroscopy for the identification of different positron trapping sites during artificial aging

The article *Identification of different positron trapping sites during artificial aging of a commercial light weight alloy* was published in the Conference Proceedings of the 18th International Conference on Positron Annihilation **2182**, 050012, December 2019 [9].

This work was done by Laura Resch as first author. Laura Resch prepared the samples and performed all measurements and the corresponding data analysis. The interpretation of the data was done by Laura Resch and Gregor Klinser. The manuscript was written by Laura Resch; the final editing of the manuscript was done in collaboration with all co-authors. Wolfgang Sprengel and Roland Würschum supervised the experimental progress and the writing process.

In connection to the positron lifetime results concerning the AW 6060 alloy presented in article 1 [8], further conclusions regarding the different types of positron trapping sites in the Al matrix occuring at different states of the precipitation sequence during artificial aging are drawn. This was achieved by positron annihilation lifetime measurements of AW 6060 samples in two distinct pre-defined artificial aging states in dependence of the applied measurement temperature. By the temperature dependence of the positron lifetime in the range from 30 K to 270 K it could be distinguished whether positrons annihilate predominantly in shallow or deep traps and thus it could be analyzed which stages in the precipitation sequence act as shallow traps and which stages act as deep positron traps.

Identification of Different Positron Trapping Sites during Artificial Aging of a Commercial Light Weight Alloy

Laura Resch[1,a)], Gregor Klinser[1], Wolfgang Sprengel[1] and Roland Würschum[1]

[1]*Institute of Materials Physics, Graz University of Technology, Petersgasse 16, 8010 Graz, Austria*

[a)]Corresponding author: l.resch@tugraz.at

Abstract. Despite the great relevance of age hardenable light weight alloys, the underlying precipitate formation, especially the initial clustering stages are not fully understood yet. In a previous study, we could identify and analyze three main stages of the precipitation sequence in the commercial alloy AW6060. In the present study, additionally, we detected shallow positron traps attributed to solute clusters by temperature dependent measurements of the positron lifetime after distinct artificial aging times at 210°C. For a first sample, artificially aged for 1000 s, the existence of shallow positron traps was unambiguously proven whereas for a second sample, aged for 2 h, only the presence of a small fraction of shallow traps coexisting with a predominant fraction of β" precipitates could be concluded.

Introduction

Age-hardenable Al-Mg-Si alloys are materials of great interest for various industrial applications, e.g., as car body parts in automotive industry. The main benefits of these alloys are their low weight and high hardness, which can be tailored by the application of a process referred to as 'Artificial Aging'. Although appropriate heat treatment methods have been known for a long time [1, 2] and are industrially applied, the details of the precipitation sequence, in particular its very early stages, are still under discussion [3, 4]. A generally agreed model of the general precipitation sequence in Al-Mg-Si alloys is the following [5]:

$$\text{SSSS} \rightarrow \text{Si-, Mg-clusters} \rightarrow \beta" \rightarrow \beta'/U_1/U_2 \rightarrow \beta,$$
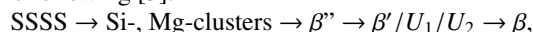
where SSSS denotes the supersaturated solid solution, β" are metastable coherent precipitates, and β', U_1 as well as U_2 are semi-coherent precipitates forming prior to the final incoherent equilibrium phase β. The peak in hardness is achieved mainly due to the coherence of the β" precipitates with the matrix and thus they are predominant in the peak-aged microstructure of the alloy.

In our previous study [6] we applied ex-situ positron annihilation lifetime spectroscopy in combination with high-precision, in-situ dilatometry to characterize the artificial aging process of a commercial grade AW6060 alloy. By a comprehensive analysis of these data, we could successfully identify and describe three stages of the precipitation sequence for two distinct aging temperatures, namely 180°C and 210°C.

The aim of the present study is to gain further information on the various types of positron traps present at certain aging states. In particular, the temperature dependence of the positron (e$^+$) lifetime gives the opportunity to distinguish whether e$^+$ annihilate within deep or shallow traps. If predominantly shallow e$^+$ traps are present in a certain aging state, the lifetime is dependent on the measurement temperature, while it is nearly temperature independent in the case of vacancies, which are deep positron traps [7]. The reason for that is the low binding energy ($\approx$55 meV [8], compared to $\approx$1 eV for deep traps) of positrons captured in shallow traps which is in the range of thermal energies even well below room temperature.

Earlier studies by Klobes et al. [8] showed a temperature dependence of the positron lifetime of the early stages of Al-Mg-Si samples naturally-aged at room temperature indicating the existence of shallow positron traps, which were attributed to solute clusters.

The present study extends the study mentioned previously [6] by the aspect of ex-situ temperature dependent measurements of the positron lifetime after distinct artificial aging times. Two samples with a well-defined artificial aging state were characterized by positron annihilation lifetime spectroscopy in a temperature range from 30 K to

205 K. In this temperature range growth or transformation of precipitates can be excluded, and consequently it gave the opportunity to decide whether the positron lifetime of a certain aging state is temperature dependent or not. This information allows an additional characterization of the e^+ traps, i.e., solute clusters and precipitates present in Al alloys at different stages of the precipitation sequence.

Experimental

A commercial-grade AW6060 Al-alloy is analyzed by means of positron-electron annihilation techniques. The samples were from the same batch and showed an excess in Mg with respect to Si (0.65 at.% Mg, 0.52 at.% Si).

Before artificial aging was applied, the samples were solution heat treated at 540°C for 30 minutes and rapidly water-quenched to room temperature to obtain a supersaturated solid solution. After this solution heat treatment all samples were kept at room temperature for 4 minutes before they were artificially aged in a drying oven at 210°C for a pre-defined time. The heat-up time of the samples in the drying oven has been measured to be 60 s and is thus not included in the aging times given below. Immediately after artificial aging the samples were kept in liquid nitrogen to prevent secondary natural aging.

For the positron lifetime measurements a ^{22}Na source was sandwiched between two identical AW6060 platelets being in a well-defined artificial aging state. The positron lifetime spectrometer used in this study is a digital fast-slow system with a time resolution of 163 ps.

The application of a cryostat allowed to acquire e^+-lifetime spectra at various temperatures ranging from 30 K to 270 K. All spectra were fitted and analyzed by the means of the program PALSFit [9].

Results and Discussion

The single positron lifetime τ of two sample pairs of distinct artificial aging states at 210°C in dependence of the measurement temperature is shown in Fig.1(a). The first sample pair (No. 1) received 1000 s and the second sample pair (No. 2) 2 hours of artificial aging at 210°C. In Fig.1(b) the lifetime values measured at 205 K are compared to our previous data (see Fig.1(b), No. 1: blue heaxgon, No. 2: blue star), showing $\bar{\tau}$ in dependence of the artificial aging time (see Fig.1(b), light red dots). Briefly summarizing, the previous study showed two distinct stages of artificial aging at 210°C. In the first stage (0-1000 s of aging time) natural aging cluster dissolve and artificial aging clusters form and grow within the Al matrix. In the subsequent stage (1000 s-10^6 s) clusters transform to coherent β'' precipitates, and with increasing aging time the formation of semi-coherent β' precipitates sets in. In the present study two samples at distinct stages (1000 s and 2 h at 210°C) of the precipitation sequence were further analyzed by the temperature dependent measurements of the e^+-lifetime shown in Fig.1(a).

For both samples, the increase of the positron lifetime with increasing measuring temperature indicates the existence of shallow positron traps, most dominantly for the sample aged at 1000 s. In fact, the total increase of $\Delta\tau_{\#1}$=15 ps or $\Delta\tau_{\#2}$=8 ps found in the present study for the two samples (#1, #2) in the temperature range between 30 K and 205 K exceeds the increase of 6 ps which is estimated to arise from thermal lattice expansion according to literature values for Al [10].

Sample pair No. 1 (1000 s, see 1(a), blue hexagons) starting from 30 K, which was the lowest measurement temperature applied shows a continuous increase of τ with increasing measurement temperature, which seems to saturate in the temperature range from 150 K to 205 K. Between 240 K and 270 K the slope increases again and τ shows no tendency of levelling off until 270 K. Since the absolute increase $\Delta\tau_{\#1}$=15 ps exceeds the increase expected due to lattice expansion, it can be attributed to the existence of shallow e^+ traps. At low measurement temperatures, e^+ predominantly annihilate in shallow traps, corresponding to lifetimes ≤190 ps. As the measurement temperature is increased an increasing fraction of positrons gathers enough thermal energy to leave the shallow traps and annihilate within deep traps corresponding to higher lifetimes. From the subsequent almost constant behaviour of the lifetime from 180 K to 205 K it can be interpreted that in this temperature range, most of the e^+ annihilate in traps of $\tau \approx$205 ps. After the data acquisition at 205 K, before heating the sample up further, a second lifetime spectrum was measured at 30 K, which resulted in a lifetime of ≈190 ps again (see 1(a), black cross). The variation of the lifetime is hence reversible in this temperature range (T≤205 K) and, as expected, no secondary natural aging appears in the samples. As the temperature is further increased secondary natural aging sets in and as a consequence the lifetime increases to 210 ps at 270 K. After data acquisition at this temperature, sample pair No. 1 was again cooled down to 30 K and another lifetime spectrum was acquired which resulted in τ=196 ps (see 1(a), black square). This is significantly
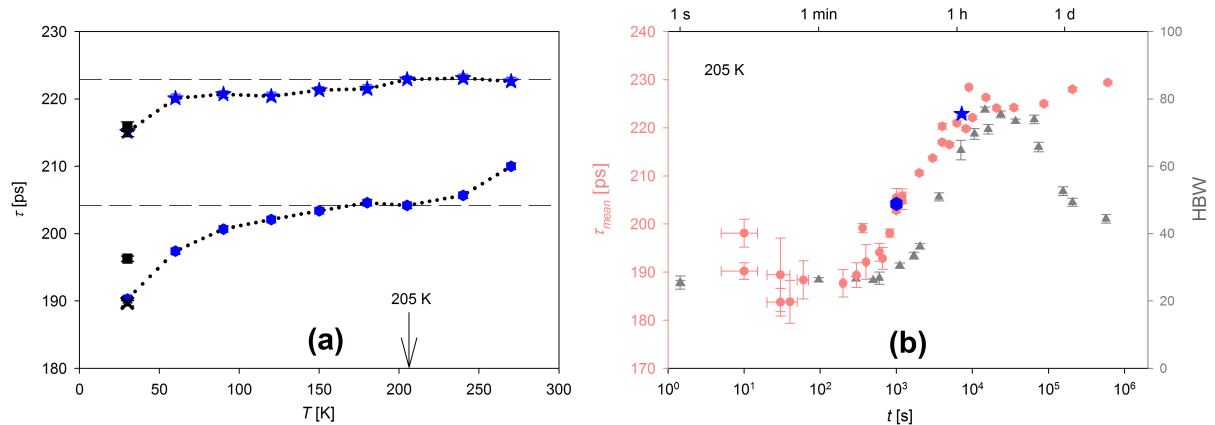
FIGURE 1. Left Panel (a): Single positron lifetime τ in dependence of the measurement temperature for both sample pairs. The blue hexagons indicate the datapoints referring to sample No. 1 (artificially aged for 1000 s at 210°C) and the blue stars indicate the datapoints referring to sample No. 2 (artificially aged for 2 h at 210°C). The dotted lines connecting the datapoints are just guides for the eyes. The dashed lines refer to the τ values measured at 205 K. Values measured at 30 K after data acquisition at 205 K (black cross) and subsequently at 240 K and 270 K (black square) are included as well. Right panel (b): Data points (blue hexagon, blue star) measured at 205 K in comparison with mean e^+ lifetime (light red dots) and hardness data (grey triangles) in dependence of the artificial aging time according to our previous study[6].

higher than both lifetime values measured at 30 K before ($\tau \approx 190$ ps) because obviously the natural aging at 240 K and 270 K applied to the sample before is not reversible.

Also in the case of sample pair No. 2, an increase of the e^+ lifetime with increasing temperature can be observed (see 1(a), blue stars). Starting from a value of ≈ 215 ps at 30 K, τ shows a continuous small increase until it stays almost constant in the temperature range from 205 K to 270 K. Differently from sample pair No. 1, the absolute difference in lifetime from 30 K to 205 K is only $\Delta\tau_{\#2}=8$ ps, a value which only slightly exceeds the lifetime increase expected due to lattice expansion. When increasing the temperature to T$\geq$240 K, in contrast to sample pair No. 1, the e^+ lifetime of No. 2 stays constant. Hence, no secondary natural aging occurs in this sample as it was already artificially aged for 2 h before the measurement. This could also be proven as the increase in τ could be reversed by cooling down the sample again after measuring at 270 K. A last measurement at 30 K (after 270 K) gave again the same lifetime value as initially ($\tau \approx 216$ ps, see 1(a), black square).

Solute clusters had already been identified as only detectable cause for shallow traps in naturally aged Al-Mg-Si as other defects, which could act as shallow traps, such as grain boundaries or dislocations could be ruled out [8]. In the present case of AW6060, after solution heat treatment, grain sizes exceed the e+ diffusion length and the number of dislocations is too low in the sample to make them play an important role. Therefore, clusters can be identified as the main reason for shallow positron trapping in the material as well.

Also our previous study (which found that the precipitation sequence is in the state of solute clustering after 1000 s of artificial aging at 210°C) supports the interpretation that solute clusters cause the temperature dependence of the e^+ lifetime of sample No. 1. On the other hand, sample pair No. 2, which received two hours of artificial aging, was found to be in the range of peak hardening and hence most solute clusters have already transformed to β" precipitates. Still, also for sample pair No. 2, a slight temperature dependence of the positron lifetime was found (see figure 1(a)). A possible explanation for this behaviour would be that, even at the peak hardened state of the alloy, there is still a small fraction of solute clusters present[11], contributing to the positron lifetime and hence giving rise to the slight temperature dependence associated with solute clusters (i.e. shallow traps) and β" precipitates. Even if the lifetime spectra here showed only one component it is possible that the two lifetimes can not be resolved independently due to their similar values.

Summary and Conclusion

Two samples, which had received different artificial aging times at 210°C were analyzed regarding the existence of shallow e^+ traps by temperature dependent e^+ annihilation lifetime spectroscopy. Both samples showed an increase of the e^+ lifetime with increasing measurement temperature from 30 K to 205 K, hence the existence of shallow traps could be concluded.

The absolute difference in lifetime between 30 K and 205 K was with a value of $\Delta\tau_{\#1} \approx 15$ ps for sample pair No. 1, remarkably higher than for No. 2 with $\Delta\tau_{\#2} \approx 8$ ps. From our previous study, it is known that for No. 1 (1000 s at 210°C) e^+ are predominantly trapped within solute clusters. Hence solute clusters could be identified as shallow e^+ traps in this case. Sample No. 2 (2 h at 210°C) is known to be nearly in the state of peak-hardening, and thus mainly β" precipitates trap e^+. A small fraction of clusters, coexisting with β" precipitates could be the reason for τ being slightly temperature dependent.

ACKNOWLEDGMENTS

REFERENCES

[1]   A. Wilm, Metallurgie: Zeitschrift für die gesamte Hüttenkunde **8**, 225–227 (1911).

[2]   O. Duprac, Z. Metallkd. **96**, 398–404 (2005).

[3]   S. Ringer and K. Hono, Mater. Charact. **44**, 101 – 131 (2000).

[4]   M. Starink, Int. Mater. Rev. **49**, 191–226 (2004).

[5]   C. D. Marioara, S. J. Andersen, H. W. Zandbergen, and R. Holmestad, Metall. Mater. Trans. A **36**, 691–702Mar (2005).

[6]   L. Resch, G. Klinser, E. Hengge, R. Enzinger, M. Luckabauer, W. Sprengel, and R. Würschum, J. Mater. Sci. Jun (2018), 10.1007/s10853-018-2612-x.

[7]   R. Krause-Rehberg and H. S. Leipner, *Positron annihilation in semiconductors: defect studies*, Vol. 127 (Springer, 1999).

[8]   B. Klobes, K. Maier,   and T. Staab, Philos. Mag. **95**, 1414–1424 (2015), https://doi.org/10.1080/14786435.2015.1031848 .

[9]   J. V. Olsen, P. Kirkegaard, N. J. Pedersen, and M. Eldrup, Phys. status solidi C **4**, 4004–4006 (2007).

[10]   H. E. Schaefer, R. Gugelmeier, M. Schmolz, and A. Seeger, Mater. Sci. Forum **15**, 111–116 (1987).

[11]   F. Ostermann, *Anwendungstechnologie Aluminium* (Springer, 2015).

[12]   P. J. Schultz, A. Vehanen, W. Thomlinson, K. Lynn, and I. MacKenzie, J. Phys. F: Met. Phys. **13**, p. L265 (1983).

4.1.3 Article 3: *In situ* Doppler broadening spectroscopy during artificial aging and subsequent solution heat treatment of the overaged state

The article *In situ monitoring of artificial aging and solution heat treatment of a commercial Al–Mg–Si alloy with a high intensity positron beam* was published in Journal of Physics: Condensed Matter **32**,08705, November 2019 [10].

This work was done by Laura Resch as first author. Laura Resch planned and organised all measurements and prepared the samples. The Doppler broadening spectroscopy measurements and parts of the data analysis were carried out by Thomas Gigl and supervised by Christoph Hugenschmidt at the NEPOMUC experiment at FRM II. Laura Resch performed further data analysis and interpreted the data together with Gregor Klinser. The manuscript was written by Laura Resch. The final editing of the manuscript was done in collaboration with all co-authors. The experimental work and the manuscript writing was supervised by Wolfgang Sprengel and Roland Würschum.

This study complements the previous *ex situ* positron lifetime studies (articles 1 and 2, refs. [8, 9]) by *in situ* measurements of the positron annihilation Doppler broadening S-parameter during artificial aging. In addition to previous measurements, in this study, not only the formation of precipitates was monitored but also their dissolution during solution heat treatment. The advantage of *in situ* measurements is a higher accuracy which can be obtained by measuring only one sample throughout the whole precipitation process instead of a series of individual samples. Thus, slight variations between individual sample preparation procedures and in the exact sample compositions can be avoided. Furthermore, an *in situ* measurement at high temperatures adds another aspect regarding the trapping behaviour of positrons, which might be different than at low temperatures because thermal detrapping plays a more important role.

In situ monitoring of artificial aging and solution heat treatment of a commercial Al–Mg–Si alloy with a high intensity positron beam

L Resch[1] , **T Gigl**[2], **G Klinser**[1], **C Hugenschmidt**[2], **W Sprengel**[1] **and R Würschum**[1]

[1] Institute of Materials Physics, Graz University of Technology, Petersgasse 16, 8010 Graz, Austria
[2] Physics Department E 21 and FRM II, Technical University Munich, D-85747 Garching, Germany

E-mail: l.resch@tugraz.at

Abstract
Microstructural changes of a commercial Al–Mg–Si alloy were studied during artificial aging by *in situ* Doppler broadening spectroscopy using a high-intensity positron beam. The *in situ* positron annihilation characteristics at high temperatures differ considerably from the conventionally applied *ex situ* measurements at low temperatures. Therefore, a more comprehensive view of precipitation processes in Al–Mg–Si alloys is obtained. Further, *in situ* positron–electron annihilation techniques allow for an investigation of aging processes with increased sensitivity. For the artificial aging temperatures of 180 °C and 210 °C pronounced variations of the Doppler broadening S-parameter reveal (i) the evolution of clusters into larger precipitates and (ii) the time of the formation of β'' precipitates and the role of vacancies in connection to this. Towards higher aging times, the transformation from coherent β'' to semi-coherent β' precipitates could be verified. Additional insights are gained by *in situ* measurements of the S-parameter during the solution heat treatment of the previously overaged sample. Here, the S-parameter reveals both the dissolution of precipitates starting from temperatures of 364 °C and the thermal generation of vacancies.

Keywords: positron–electron annihilation, Al alloys, positron beam

(Some figures may appear in colour only in the online journal)

1. Introduction

Age-hardenable aluminium alloys have the advantage of low weight and good resistance to corrosion and hence are being used in an increasingly wide range of industrial applications [1, 2]. These alloys achieve their maximum hardness after heat treatment at elevated temperatures due to the growth of precipitates within the Al matrix, which harden the material by hindering dislocation movement. This process is referred to as artificial aging. Although Al–Mg–Si alloys were developed in the 1920s and appropriate heat treatment methods have been known for a long time [3, 4], the detailed processes controlling the change in hardness during artificial aging are still not fully understood. When the technique of age hardening is applied, the first step is to quench the alloy from the high temperature single-phase region to room temperature producing a supersaturated solid solution (SSSS). In a second step at elevated temperatures, the system transitions from the SSSS state through a series of intermediates with meta-stable precipitates, of different crystal structure and chemical

composition, towards its equilibrium phase. An approximate, generally agreed model is the following precipitation sequence [5]:

$$\text{SSSS} \rightarrow \text{Si-, Mg- clusters} \rightarrow \beta'' \rightarrow \beta'/\text{U}_1/\text{U}_2/\text{B'} \rightarrow \beta.$$
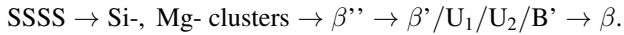
From the supersaturated solid solution Si- and Mg-clusters and co-clusters are formed during the first minutes of aging. They evolve into metastable β'' precipitates, which are coherent to the Al matrix. Due to their coherence β'' precipitates make a major contribution to the hardness of the alloy. They are found to be the dominant type of precipitate in samples exhibiting maximum hardness [6]. The crystal structure of β'' precipitates was determined to be monoclinic using transmission electron microscopy (TEM) and quantitative electron diffraction refinements [7]. Their composition most likely, is $\text{Mg}_4\text{Al}_3\text{Si}_4$ as revealed by scanning transmission electron microscopy [8]. After longer aging times the β'' precipitates transform into β', U_1, U_2 and B' precipitates, which can coexist in the alloy and are semi-coherent to the Al matrix [9]. The β' phase is predominant among those phases and therefore best known. It has been determined by electron diffraction measurements and first principles calculations that β' precipitates are of hexagonal crystal structure and do not contain Al (composition of β': Mg_9Si_5) [10]). On the other hand, the U_1, U_2 and B' precipitates contain varying amounts of Al and differ in their crystal structures [6, 11, 12]. Whether and to what extent U_1, U_2 and B' precipitates are formed during aging is strongly dependent on the exact composition of the alloy and the previous heat treatment. The final stage in the precipitation sequence is the equilibrium phase β (Mg_2Si). The β precipitates appear after several days of artificial aging. They are incoherent to the Al matrix and have a face centered cubic crystal structure [13].

Apart from the above mentioned methods, the sequence and compositions of precipitates following the β'' phase can be observed experimentally by various other techniques such as differential scanning calorimetry (DSC) [14] or atom probe tomography [11]. Initial clustering of few atoms, which proceeds on very short timescales, as well as transitions between different precipitation stages are difficult to resolve by established techniques. However, due to their strong influence on artificial aging, a detailed understanding of these processes is of fundamental importance for tailoring the hardness of the material.

Positron annihilation spectroscopy is a very suitable technique to observe the aging behaviour of Al alloys [15]. Positrons are highly sensitive to open volume defects such as vacancies, which play an important role in the initial clustering stages. Further, transitions from coherent to semi- or incoherent precipitates can be monitored due to changes in the associated free volume. An additional benefit for the particular case of Al–Mg–Si alloys is, that positrons are captured by the precipitates, even if they do not include open volume defects. This is due to the increased positron affinity towards Mg and Si compared to Al [16–18].

In the past, positron annihilation spectroscopy has been successfully applied in studies of the microstructural changes in Al–Mg–Si alloys during age hardening [19, 20]. These include *in situ* studies in which changes in the precipitation process occured at room temperature (natural aging), and on a time scale that enabled monitoring by positron annihilation lifetime spectroscopy.

Here, we present the first *in situ* study at elevated temperatures of artificial aging (at 180 °C and 210 °C) as well as the dissolution of precipitates (>360 °C, i.e. solution heat treatment) for a commercial light weight alloy. This is achieved by *in situ* monitoring the S-parameter of the Doppler broadened positron–electron annihilation spectrum. The so-called S-parameter is used for the quantitative evaluation of the Doppler broadening spectrum of the positron–electron annihilation. It is defined as the area of the central low-momentum part of the spectrum divided by the area below the whole curve after background subtraction. The S-parameter is related to the annihilation of positrons with valence electrons of the sample. As the density of open volume defects in the sample increases, the S-parameter increases [21]. The high intensity of the positron beam at the NEPOMUC facility at FRM II enables fast spectra acquisition in order to resolve precipitation processes on very short timescales [22, 23].

The advantage of this kind of *in situ* studies compared to *ex situ* measurements is obvious. For *ex situ* studies it is necessary to measure a series of individual samples, which may vary in their composition and thus increase the uncertainty of the measurement. Further, for *ex situ* studies, each sample has to be quenched individually and kept in its particular aging state until and during the spectra acquisition. Slight variations of this procedure between different samples are unavoidable. However, by continuously *in situ* monitoring the S-parameter of only one sample during artificial aging the above mentioned uncertainties can be eliminated and the accuracy of the measurement can be increased drastically. Moreover, secondary natural aging during the spectra acquisition can be excluded, which was not the case for previous studies where the positron lifetime spectra were acquired *ex situ* at room temperature after the samples had undergone artificial aging [19]. Also the trapping behaviour might be different at low and high temperatures depending on the nature of the trapping sites. Therefore, recording positron–electron annihilation parameters at different temperatures as presented here provides more detailed insights to atomic processes.

2. Experimental

In this study a commercial-grade AW6060 Al-alloy was used in a T6 state (solution heat treatment and peak aging of the alloy) in the as-received condition. Both samples investigated were obtained from the same low-alloyed batch and were rich in magnesium (0.65at% Mg, 0.52at% Si) as revealed by optical emission spectroscopy.

In situ positron annihilation experiments were performed at the NEPOMUC high-intensity positron beamline. This positron beam provides $>10^9$ moderated positrons per second at an energy of 1 keV enabling a temporal resolution of the precipitation process in the alloy. All Doppler broadening spectra and corresponding S-parameter data presented here
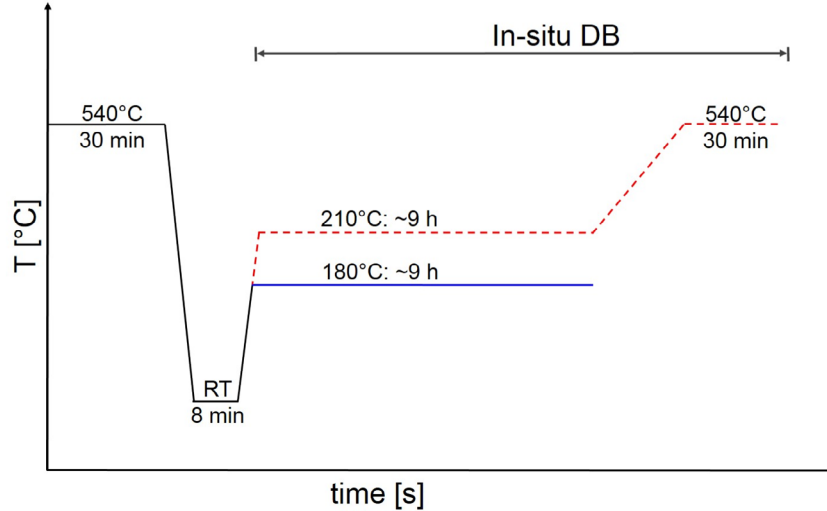
Figure 1. Sketch of the heat treatment applied to the AW6060 samples prior to and during *in situ* Doppler broadening (DB) spectroscopy.

were acquired using the Doppler broadening (DB) spectrometer [24] at the NEPOMUC beamline using four high-purity Ge detectors. The central region for calculation of the S-parameter was chosen symmetrically around the 511 keV annihilation peak from 510.15 to 511.85 keV.

The temperature program which was applied to the samples before and during the measurements is sketched in figure 1. Prior to any aging experiments, the samples were solution heat treated at (540 ± 1)°C for 30 min and subsequently water quenched to room temperature. In order to prevent natural aging, the quenched samples were stored in liquid nitrogen until mounting them into the DB spectrometer. It took approximately 8 min to reach the predefined artificial aging temperatures of 180 °C and 210 °C after removal from the liquid nitrogen bath.

In the case of artificial aging at 180 °C (210 °C) the S-parameter was first recorded for 19 min (47 min) with an integration time (time of spectra acquisition) of 15 s and a minimum of 1.3×10^5 counts per spectrum, at a fixed positron implantation energy of $E = 28$ keV. Within the following 9 hours of artificial aging (the temperature was continuously kept at 180 °C and 210 °C) for both samples the implantation energy E of the positron beam was repeatedly ramped from 0.5 keV to 28 keV within 30 min. Doppler broadening spectra were acquired with an integration time of 60 s and a minimum of 5×10^5 counts per spectrum.

Additionally for the sample aged at 210 °C, the S-parameter was recorded *in situ* during solution heat treatment directly after aging. Here the temperature was raised from 210 °C to 540 °C with a rate of approximately 8 °C min^{-1} (integration time: 60 s).

3. Results and discussion

### 3.1. Variation of the in situ Doppler broadening S-parameter during artificial aging at 180 °C and 210 °C

The *in situ* beamline measurements of the S-parameter are given in figures 2 and 3 for the artificial aging temperatures

of 180 °C and 210 °C, respectively. They are compared to the *ex situ* measurements of the mean positron lifetime τ_m, which were previously obtained from a laboratory set-up, and *in situ* dilatometric measurements of the length change $\Delta L/L$ [25].

A combined interpretation of $\Delta L/L$ and τ_m in a previous study led to the identification of three main steps in the precipitation sequence [25]. For an artificial aging temperature of 180 °C, in a first timespan A (10 s–100 s) natural aging clusters dissolve and artificial aging clusters form in the Al matrix. Next, during timespan B (100 s–11 000 s) solute clusters grow and are eventually transformed into coherent β'' precipitates. The exact time of this transformation could, however, not be verified. For proceeding artificial aging, β'' precipitates are finally transformed into semi-coherent β' precipitates (timespan C).

Also for an aging temperature of 210 °C, timespan A is attributed to the dissolution of natural aging clusters and the subsequent formation of artificial aging clusters. Contrary to the case of artificial aging at 180 °C, timespan B is skipped in this case. Due to elevated temperatures the transformation from β'' to β' precipitates sets in earlier and timespan C proceeds directly after timespan A.

In the present study, in timespan B, where no significant change of τ_m could be observed for an aging temperature of 180 °C, the S-parameter first increases significantly until it reaches an apparent maximum value at about 10^3 s. It should be noted that the next S-parameter datapoint following the maximum value at about 10^3 s is recorded 29 min later. Therefore, the position of the maximum of the S-parameter can only be estimated to be in the timespan between 10^3 s and 1.8×10^3 s. The maximum of the S-parameter is followed by a rapid decrease of the S-parameter until ca. 10^4 s which marks the end of timespan B. For aging times longer than 10^4 s the S-parameter increases again. For artificial aging at 210 °C the S-parameter shows very similar characteristics as for 180 °C. It reaches a maximum at ca. 700 s (several minutes before the end of timespan A), followed by a rapid decrease until about 2.5×10^3 s and a subsequent increase with no tendency of levelling off until 3.7×10^4 s.
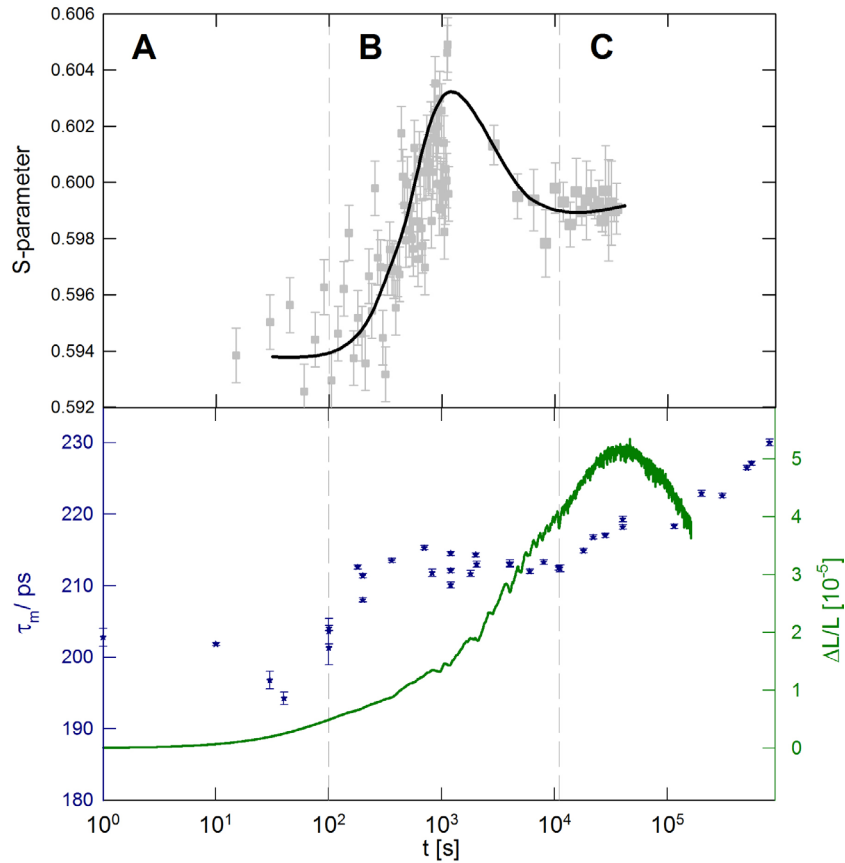
Figure 2. S-parameter (grey squares), mean positron lifetime (blue stars) and length change (solid green line) of the AW6060 sample in dependence of the artificial aging time at 180 °C. The solid black line is a guide for the eyes. The lower panel is reproduced from [25] for comparison.

Interestingly, for both artificial aging temperatures, the variations of τ_m and the S-parameter do not coincide, which is initially unexpected, since both parameters are sensitive to the mean free volume of defects in the alloy in similar way. However, the measurement temperatures of the *ex situ* (−70 °C) and the *in situ* (180 °C/210 °C) experiments are different. Due to the high measurement temperatures during the *in situ* experiment, the variation of the S-parameter is only affected by the annihilation of positrons in deep traps, where thermal detrapping is very unlikely. On the other hand, the *ex situ* positron lifetime spectra were acquired at measurement temperatures of −70 °C, where positrons are also captured by shallow traps. Previous studies demonstrated that both trap types are present in Al-alloys during the course of aging [26]. Vacancies and larger precipitates in alloys act as deep positron traps with binding energies of about 1 eV. Shallow positron traps are clusters and small coherent precipitates which bind positrons only weakly (binding energies of about 55 meV) [26].

From previous *ex situ* positron lifetime measurements a transformation of precipitates from shallow to deep positron traps was verified. The measurements showed that after 10^3 s there are shallow traps present while after 10^4 s most of the positron traps are deep traps [27]. On the other hand, the *in situ* S-parameter includes only information about deep traps and does not give further information, neither about shallow traps nor about the ratio of shallow to deep traps. From the

initial increase of the S-parameter it can be concluded that the number of deep traps increases. At the time where the maximum S-parameter is observed this transformation of shallow to deep traps is being overshadowed by the subsequent process (the β'' transformation), but it cannot be concluded that the transformation to deep traps is finished yet.

For aging at a higher temperature (210 °C), the maximum of the S-parameter is shifted to lower aging times compared to aging at 180 °C. For both temperatures, the decrease of the S-parameter following this maximum occurs simultaneously with an increase of $\Delta L/L$. The increase of $\Delta L/L$ corresponds to an increasing number of β'' precipitates in the alloy. Thus, the maximum of the S-parameter marks the time at which the pre-β'' to β'' transformation occurs. It is likely, that remanent vacancies serving as diffusion vehicles anneal out at this point. It has to be noted that previous studies suggest that vacancies are trapped in pre-β'' precipitates, which might anneal out due to the transformation to β'' precipitates [14, 28]. In this case only a minor fraction of pre-β'' precipitates can include vacancies. If the fraction of the pre-β'' precipitates containing vacancies were pre-dominant their annealing would be visible by a decrease of τ_m, which is not the case.

Similarly, a nearly opposite behaviour of the S-parameter and τ_m was previously also observed for isochronal annealing of Al-1.9at% Cu [29]. Here, the variations of the S-parameter were caused by an agglomeration of Cu in the surroundings of the positron annihilation site. In analogy, the increase and
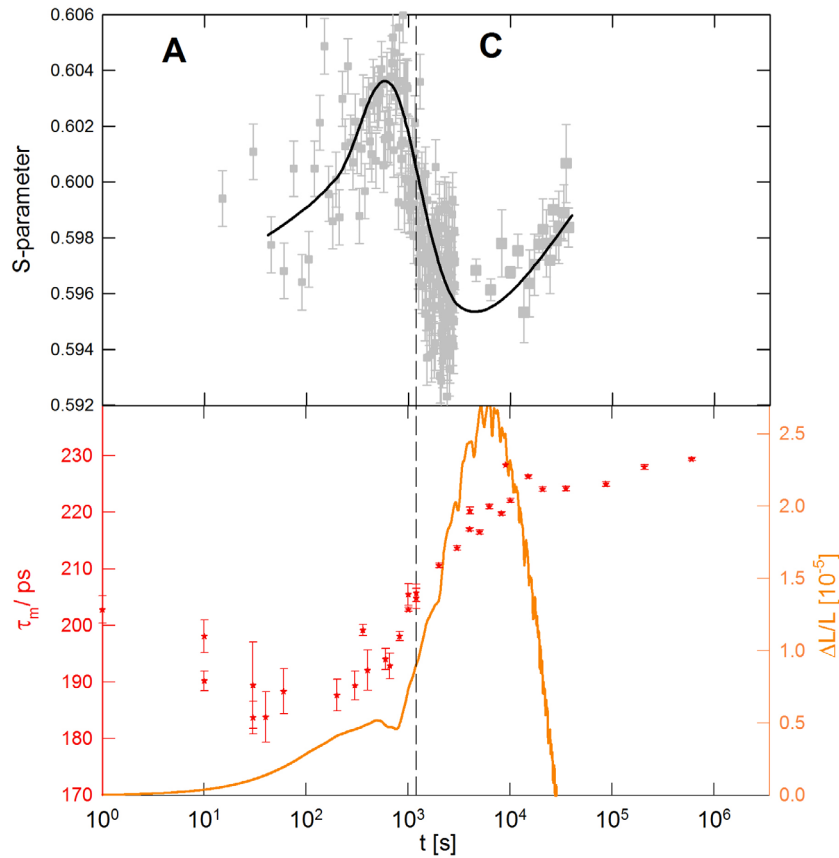
Figure 3. S-parameter (grey squares), mean positron lifetime (red stars) and length change $\Delta L/L$ (solid orange line) of the AW6060 sample in dependence of the artificial aging time at 210 °C. The lower panel is reproduced from [25] for comparison. CC BY 4.0.

subsequent decrease of the S-parameter might therefore also be interpreted as follows: For the Al–Mg–Si alloy AW6060, the formation of pre-β" precipitates, which are initially rich in Mg, can cause an increase of the S-parameter compared to Al due to a lower valence electron density [19, 30]. The subsequent decrease of the S-parameter, on the other hand, indicates an enrichment of precipitates with Si atoms upon β"-formation, which leads to an electron density increase. Indeed, indication for initially Mg-enriched pre-β" precipitates are reported for Al–Mg–Si [14]. However, in the case of AW6060, the exact composition of pre-β" precipitates is not clear yet [31, 32]. Therefore the above described, alternative interpretation is reasonable but still speculative.

The increase of the S-parameter from 2.5×10^3 s onwards at 210 °C is attributed to the transformation of β" to β' precipitates. The β' precipitates are semi-coherent and thus include a higher open volume than the coherent β" precipitates. This is also confirmed by dilatometry, where the maximum of $\Delta L/L$, corresponding to the onset of the transformation to β', occurs simultaneously to the increase of the S-parameter [33].

Again, this increase of the S-parameter can also be caused by a change of the valence electron density n_{val} as the β" precipitates transform into β' precipitates. In contrast to the situation for the pre-β"—β" transformation (see above), here it is clear that n_{val} decreases for a transformation from β"(monoclinic, $Mg_4Al_3Si_4$ [8]) to β' (hexagonal, Mg_9Si_5 [10]) precipitates. As the S-parameter varies inversely with n_{val} [30],

the observed increase of the S-parameter is consistent with a decrease of n_{val}.

For artificial aging at 180 °C and times between 10^4 s and 3×10^4 s only a slight increase of the S-parameter could be observed (see figure 2) which is, however, within the error bars of this data. Obviously, due to a slower proceeding precipitation sequence at 180 °C compared to 210 °C, the β" to β' transformation starts beyond the measuring time (which is limited to 3×10^4 s).

3.2. In situ solution heat treatment after over-aging at 210 °C

In figure 4 the temperature dependence of the S-parameter, for two nominally similar AW6060 samples, is shown during, and subsequent to, the solution heat treatment after over-aging at 210 °C. Both show a very similar behaviour of the S-parameter in dependence of the temperature demonstrating the high reproducability of the experiment. The S-parameter stays almost constant from 227 °C to 364 °C followed by a significant decrease up to 422 °C. Above 422 °C, the S-parameter increases again and shows a tendency of levelling off towards the last recorded datapoints at temperatures of 527 °C.

The decrease of the S-parameter in the temperature range from 364 °C to 422 °C can be assigned to the dissolution of the previously formed artificial aging precipitates. DSC measurements in an Al alloy, with similar Mg-to-Si ratio
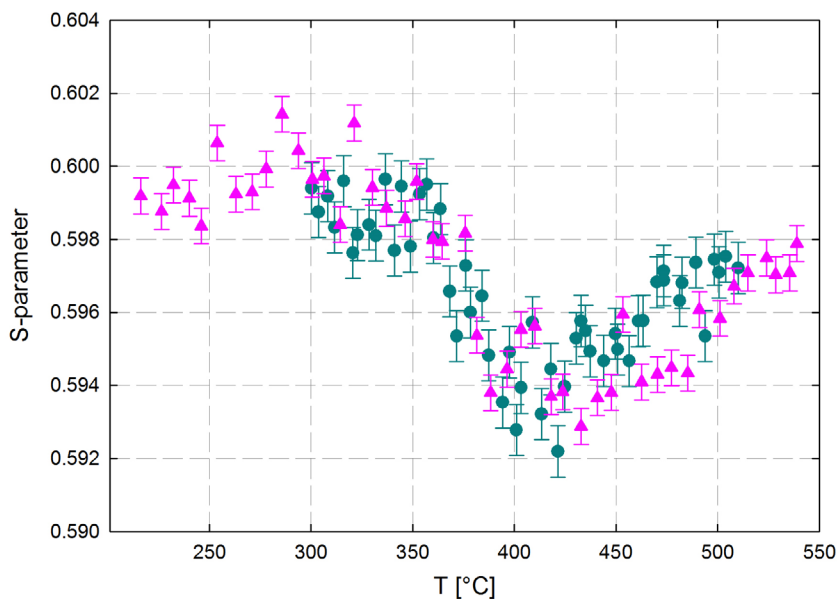
Figure 4. S-parameter of two distinct samples (sample 1: cyan dots, sample 2: pink triangles) in dependence of temperature after artificial aging at 210 °C. Note that the absolute values of sample 1 have been shifted on the vertical axis for comparison.

(AW6082) revealed the dissolution of precipitates from 397 °C to 497 °C [34].

The subsequent increase of the S-parameter above 422 °C is attributed to the generation of vacancies in the sample due to elevated temperatures. Comparing these $S(T)$ data-points to the increase of the S-parameter in dependence of the temperature for pure Al [35], in both cases similar slopes of $S(T)$ in the temperature range from 422 °C to 527 °C are observed.

4. Summary and conclusion

In this study the Doppler broadening S-parameter of an Al–Mg–Si alloy was measured *in situ* during artificial aging at 180 °C and 210 °C. In addition, the solution heat treatment after artificial aging at 210 °C was also monitored.

From an initial increase of the S-parameter until about 10^3 s (700 s) during artificial aging at 180 °C (210 °C) it can be concluded, that an increasing number of clusters, which are shallow positron traps, evolve into larger precipitates serving as deep positron traps. The subsequent decrease of the S-parameter can be attributed to a small fraction of remanent vacancies annealing out of the precipitates during the formation of β" precipitates. An alternative explanation for the initial increase and subsequent decrease of the S-parameter might be the varying Mg and Si content upon pre-β" to β"-transformation. This could, however, not be finally verified since the exact composition of pre-β" precipitates remains unclear. The recovery of the S-parameter values for times greater than 2.5×10^4 s for an artificial aging temperature of 210 °C corresponds to the transformation from β" to β' precipitates.

The S-parameter in dependence of the temperature $S(T)$, recorded during solution heat treatment, shows a decrease caused by the dissolution of precipitates from

364 °C to 422 °C. A subsequent increase of $S(T)$ from 422 °C onwards is due to thermal vacancy generation in the alloy.

ORCID iDs

L Resch ⦿ https://orcid.org/0000-0001-5812-2869

References

[1] Miller W S, Zhuang L, Bottema J, Wittebrood A J, De Smet P, Haszler A and Vieregge A 2000 Recent development in aluminium alloys for the automotive industry *Mat. Sci. Eng.* A **280** 37–49
[2] Zhang X H, Su G, Ju G C, Wang C W and Yan W L 2010 Effect of modification treatment on the microstructure and mechanical properties of Al-0.35%Mg-7.0%Si cast alloy *Mater. Des.* **31** 4408–13
[3] Wilm A 1911 Physikalisch-metallurgische Untersuchungen über magnesiumhaltige Aluminiumlegierungen *Metall.: Z. Gesamte Hüttenkunde* **8** 225–7
[4] Duprac O H 2005 Alfred Wilm and the beginnings of Duralumin *Z. Metall.* **96** 398–404
[5] Marioara C D, Andersen S J, Zandbergen H W and Holmestad R 2005 The influence of alloy composition on precipitates of the Al–Mg–Si system *Metall. Mater. Trans.* A **36** 691–702
[6] Zandbergen M W, Xu Q, Cerezo A and Smith G D W 2015 Study of precipitation in Al–Mg–Si alloys by atom probe

tomography I. Microstructural changes as a function of ageing temperature *Acta Mater.* **101** 136–48

[7] Andersen S J, Zandbergen H W, Jansen J, Traeholt C, Tundal U and Reiso O 1998 The crystal structure of the β'' phase in Al–Mg–Si alloys *Acta Mater.* **46** 3283–98

[8] Ninive P H, Strandlie A, Gulbrandsen-Dahl S, Lefebvre W, Marioara C D, Andersen S J, Friis J, Holmestad R and Løvvik O M 2014 Detailed atomistic insight into the β'' phase in Al–Mg–Si alloys *Acta Mater.* **69** 126–34

[9] Frøseth A G, Høier R, Derlet P M, Andersen S J and Marioara C D 2003 Bonding in MgSi and Al–Mg–Si compounds relevant to Al–Mg–Si alloys *Phys. Rev.* B **67** 224106

[10] Vissers R, van Huis M A, Jansen J, Zandbergen H W, Marioara C D and Andersen S J 2007 The crystal structure of the β' phase in Al–Mg–Si alloys *Acta Mater.* **55** 3815–23

[11] Andersen S J, Marioara C D, Frøseth A, Vissers R and Zandbergen H W 2005 Crystal structure of the orthorhombic U2-Al$_4$Mg$_4$Si$_4$ precipitate in the Al–Mg–Si alloy system and its relation to the β' and β'' phases *Mat. Sci. Eng.* A **390** 127–38

[12] Andersen S J, Marioara C D, Vissers R, Frøseth A and Zandbergen H W 2007 The structural relation between precipitates in Al–Mg–Si alloys, the Al-matrix and diamond silicon, with emphasis on the trigonal phase U1-MgAl2Si2 *Mat. Sci. Eng.* A **444** 157–69

[13] Geisler A H and Hill J K 1948 Analyses and interpretations of x-ray diffraction effects in patterns of aged alloys *Acta Crystallogr.* **1** 238–52

[14] Edwards G A, Stiller K, Dunlop G L and Couper M J 1998 The precipitation sequence in Al–Mg–Si alloys *Acta Mater.* **46** 3893–904

[15] Dupasquier A, Kögel G and Somoza A 2004 Studies of light alloys by positron annihilation techniques *Acta Mater.* **52** 4707–26

[16] Staab T E M, Krause-Rehberg R, Hornauer U and Zschech E 2006 Study of artificial aging in AlMgSi (6061) and AlMgSiCu (6013) alloys by positron annihilation *J. Mater. Sci.* **41** 1059–66

[17] Dlubek G 1987 Positron studies of decomposition phenomena in Al alloys *Mater. Sci. Forum* **13** 11–32

[18] Puska M J, Lanki P and Nieminen R M 1989 Positron affinities for elemental metals *J. Phys.: Condens. Matter* **1** 6081

[19] Banhart J, Liu M, Yong Y, Liang Z, Chang C S T, Elsayed M and Lay M D 2012 Study of ageing in Al–Mg–Si alloys by positron annihilation spectroscopy *Physica* B **407** 2689–96

[20] Klobes B, Korff B, Balarisi O, Eich P, Haaks M, Maier K, Sottong R, Hühne S M, Mader W and Staab T E M 2010 Probing the defect state of individual precipitates grown in an Al–Mg–Si alloy *Phys. Rev.* B **82** 054113

[21] Krause-Rehberg R and Leipner H S 1999 *Positron Annihilation in Semiconductors* (New York: Springer)

[22] Hugenschmidt C, Löwe B, Mayer J, Piochacz C, Pikart P, Repper R, Stadlbauer M and Schreckenbach K 2008 Unprecedented intensity of a low-energy positron beam *Nucl. Instrum. Methods* A **593** 616–8

[23] Hugenschmidt C, Ceeh H, Gigl T, Lippert F, Piochacz C, Reiner M, Schreckenbach K, Vohburger S, Weber J and Zimnik S 2014 Positron beam characteristics at nepomuc upgrade *J. Phys.: Conf. Ser.* **505** 012029

[24] Gigl T, Beddrich L, Dickmann M, Rienäcker B, Thalmayr M, Vohburger S and Hugenschmidt C 2017 Defect imaging and detection of precipitates using a new scanning positron microbeam *New J. Phys.* **19** 123007

[25] Resch L, Klinser G, Hengge E, Enzinger R, Luckabauer M, Sprengel W and Würschum R 2018 Precipitation processes in Al–Mg–Si extending down to initial clustering revealed by the complementary techniques of positron lifetime spectroscopy and dilatometry *J. Mater. Sci.* **53** 14657–65

[26] Klobes B, Maier K and Staab T E M 2015 Early stage ageing effects and shallow positron traps in Al–Mg–Si alloys *Phil. Mag.* **95** 1414–24

[27] Resch L, Klinser G, Sprengel W and Würschum accepted R 2018 Identification of different positron trapping sites during artificial aging of a commercial light weight alloy *AIP Conf. Proc.* accepted

[28] Kelly A and Nicholson R B 1963 Precipitation hardening *Prog. Mater. Sci.* **10** 151

[29] Gläser U H, Dlubek G and Krause R 1991 Vacancies and precipitates in Al-1.9 at% Cu studied by positrons *Phys. Status Solidi* b **163** 337–43

[30] Dannefaer S, Puff W and Kerr D 1997 Positron line-shape parameters and lifetimes for semiconductors: systematics and temperature effects *Phys. Rev.* B **55** 2182

[31] Van Huis M A, Chen J H, Zandbergen H W and Sluiter M H F 2006 Phase stability and structural relations of nanometer-sized, matrix-embedded precipitate phases in Al–Mg–Si alloys in the late stages of evolution *Acta Mater.* **54** 2945–55

[32] Marioara C D, Andersen S J, Jansen J and Zandbergen H W 2001 Atomic model for GP-zones in a 6082 Al–Mg–Si system *Acta Mater.* **49** 321–8

[33] Hengge E, Enzinger R, Luckabauer M, Sprengel W and Würschum R 2018 Quantitative volumetric identification of precipitates in dilute alloys using high-precision isothermal dilatometry *Phil. Mag. Lett.* **98** 301–9

[34] Osten J, Milkereit B, Schick C and Kessler O 2015 Dissolution and precipitation behaviour during continuous heating of Al–Mg–Si alloys in a wide range of heating rates *Materials* **8** 2830–48

[35] Schaefer H E, Gugelmeier R, Schmolz M and Seeger A 1987 Positron lifetime spectroscopy and trapping at vacancies in aluminium *Mater. Sci. Forum* **15** 111–6 (Trans Tech Publ)

4.2   Positron annihilation lifetime spectroscopy of concentrated solid-solution alloys

4.2.1   Article 4: Investigation of quenched-in thermal vacancies in concentrated solid-solution alloys

The article *Search for vacancies in concentrated solid-solution alloys with fcc crystal structure* was published as Rapid Communication in Physical Review Materials **4**, 060601(R), June 2020 [17] with an editor's suggestion.

This work was done by Laura Resch as first author. Martin Luckabauer produced and prepared all samples from raw materials supervised by Norihiko Okamoto and Tetsu Ichitsubo. The characterisation of the samples by electron backscatter diffraction and energy-dispersive X-ray spectroscopy was conducted by Martin Luckabauer and Nick Helthuis. Robert Enzinger and Laura Resch performed the sample preparation prior to the positron lifetime spectroscopy measurements. Laura Resch performed and analysed all positron lifetime spectroscopy and X-ray diffraction measurements. The manuscript was written by Laura Resch; the final editing of the manuscript was done in collaboration with all co-authors. Roland Würschum and Wolfgang Sprengel supervised the experimental progress and the manuscript writing.

In this study the authors investigate the thermal generation of vacancies in the new material class of concentrated solid-solution alloys, often referred to as high-entropy alloys, by positron annihilation lifetime spectroscopy. A set of face-centered cubic concentrated solid-solution alloys with a varying number of constituents was rapidly quenched from temperatures close to their onset of melting and cooled to liquid nitrogen temperatures immediately afterwards. In this state, the concentration of quenched-in vacancies was determined by positron annihilation lifetime spectroscopy applying low temperatures during the spectra acquisition.

Search for vacancies in concentrated solid-solution alloys with fcc crystal structure

L. Resch [1,*] M. Luckabauer [2] N. Helthuis [2] N. L. Okamoto [3] T. Ichitsubo [3] R. Enzinger [1]
W. Sprengel [1] and R. Würschum [1]

[1]*Institute of Materials Physics, Graz University of Technology, Petersgasse 16, 8010 Graz, Austria*
[2]*Faculty of Engineering Technology, University of Twente, P.O. Box 217, 7500AE Enschede, The Netherlands*
[3]*Institute for Materials Research, Tohoku University, Sendai 980-8577, Japan*

Single-phase concentrated solid-solution alloys (CSA), i.e., alloys without a principle alloying element but one randomly populated crystal structure, exhibit attractive material properties such as very high ductility at cryogenic temperatures, a gentle decrease of strength with temperature, or an unexpectedly high resistance against irradiation. For clarification of those observations assessment of atomic transport mechanisms including formation and migration of equilibrium point defects is indispensable. Positron annihilation lifetime spectroscopy measurements are performed to quantify the concentration of quenched-in thermal vacancies in fcc CSAs after quenching from temperatures close to their onset of melting. For various alloy compositions the concentration of quenched-in vacancies decreases with increasing entropy of mixing ΔS_{mix}. Whereas alloys with three constituents in nonequimolar fractions (CrFeNi) exhibit vacancy concentrations in the 10^{-5} range, the studied alloys with four (CoCrFeNi) and five constituents (CoCrFeMnNi, AlCoCrFeNi) do not show a vacancy-specific positron lifetime. Therefore, the concentration of quenched-in vacancies must be in the range of 10^{-6} or less. It can be concluded that there is either only a vanishingly small fraction of vacancies present at temperatures near the onset of melting or the generated vacancies are inherently unstable.

I. INTRODUCTION

Over the last decade a new class of multicomponent single-phase alloys, often referred to as high entropy alloys, or concentrated solid-solution alloys, gained increasing attention (see, e.g., Refs. [1–4]). Contrary to conventional alloys, which consist of one base element and minor additions of other elements to achieve desired properties, these concentrated solid-solution alloys consist of multiple principal elements in equimolar fractions. Based on general knowledge on physical metallurgy, multicomponent alloys were assumed to form multiple phases and intermetallic compounds and to experience undesired properties such as brittleness. However, it turned out that a high number of different multicomponent alloys can be designed which form random solid solutions with mostly face-centered-cubic or body-centered-cubic structures. Concentrated solid-solution alloys have been reported to possess various desirable material properties such as high strength in combination with good ductility even at high temperatures [5,6], excellent wear and corrosion resistance [7,8], as well as superior radiation tolerance [9,10]. These properties make them interesting candidates for components used in extreme environments such as, for example, nuclear reactors. The enhanced radiation tolerance of concentrated solid-solution alloys has been the subject of several studies which concluded that the most probable cause is the distortion of the crystal lattice which slows down dislocation movement [10]. Concomitantly, further studies were conducted concerning the diffusion properties of these alloy types. The most recent studies among them, which applied the radiotracer method, found that there is no tendency of decreasing diffusivity with an increasing number of components, if compared on an absolute temperature scale [11].

An important aspect for a comprehensive understanding of bulk diffusion and radiation tolerance is the formation and migration behavior of vacancies in the multicomponent matrix. For this purpose, positron annihilation lifetime spectroscopy is a highly suitable technique, which is capable of detecting vacancy concentrations in the concentration range from 10^{-6} to 10^{-4} [12]. Positrons from a radioactive source are implanted into the sample, where they annihilate emitting two γ-quants. The positron lifetime in the material measured as the time difference between a start γ-quant (β-decay of ^{22}Na) and the annihilation γ-quant includes specific and sensitive information on the defect structure of the sample.

In a previous positron annihilation study [13] a high defect concentration was found in an as-cast CoCrFeNi alloy, but it could not be discerned whether these defects were dislocations or vacancies. On the other hand, for the case of as-cast CoCrFeMnNi, it has been reported that the bulk of the material does not contain any structural defects [14]. In a recent study on the CoCrFeMnNi alloy, a strong increase of the mean positron lifetime with increasing temperature was observed indicating thermal generation of vacancies [15]. However, the positron lifetime in dependence of the temperature did

*Corresponding author: l.resch@tugraz.at

not saturate, not even in the region of the highest applied temperature of 1473 K ($0.92T_{m,\text{CoCrFeMnNi}}$). Furthermore, the mean positron lifetimes measured at 293 K after the heat treatment were not significantly lower than the high temperature values which should be the case for reversible formation and removal of thermal vacancies. Hence, it remains unclear if the reported increase of the mean positron lifetime with increasing temperature is due to the thermal generation of vacancies or whether other processes in the multicomponent matrix such as phase decompositions play a role.

In the present study, positron annihilation lifetime spectroscopy is applied for the detection of thermally induced and quenched-in vacancies in a set of multicomponent concentrated solid-solution alloys. All of these alloys have a face-centered-cubic crystal structure, but exhibit an increasing number of constituents, from low to high mixing entropy. Well-defined samples of CrFeNi, CoCrFeNi, CoCrFeMnNi, and AlCoCrFeNi were subjected to an identical heat treatment under protective vacuum atmosphere, at high temperatures (1493 K), close to their onset of melting T_m ($T_{m,\text{CoCrFeNi}} = 1717$ K, $T_{m,\text{CoCrFeMnNi}} = 1607$ K [11]). Subsequently the samples were rapidly cooled to 273.15 K by quenching them in ice water. Interestingly, the positron lifetime of the quenched samples shows a decreasing trend towards a defect-free bulk positron lifetime with an increasing number of constituents, i.e., with an increase in mixing entropy.

II. EXPERIMENT

All samples were produced from raw materials with a nominal purity better or equal to 99.95 wt %. Master ingots with a mass of 20–30 g were initially produced by arc-melting in a zirconium-gettered argon atmosphere at 500 mbar absolute pressure. Every ingot was remelted six times before it was further processed. The alloys CoCrFeNi and AlCoCrFeNi were copper mold gravity cast into circular rods with a diameter of 8 mm. After casting, each rod was recrystallized in an evacuated silica tube at 1273 K for 24 h and subsequently water quenched. The other alloy samples were prepared from pieces of the master ingots which were cold-rolled to a final thickness of about 1.5 mm. The obtained sheets were heat treated in the same way as the cast rods. This process was chosen since the sheet shape facilitated the final sample preparation for the positron lifetime measurements.

Prior to any positron lifetime measurements, pairs of equivalent rectangular-shaped samples (13 mm × 5 mm × 1.5 mm) were sealed in evacuated silica tubes and kept at 1493 K for 30 min. They were then rapidly quenched to 273.15 K by fast immersion and cracking of the silica tubes in ice water. Since

all samples were still glowing bright yellow at the moment they came into direct contact with the ice water, their temperature can be estimated to be still at least 1373 K just before quenching. Using an approach as described in Ref. [16], the quenching rate for this procedure can be estimated to be at least 1200 K s^{-1}. The samples were cooled to liquid-nitrogen temperatures immediately after this quenching procedure. For the positron lifetime measurements, the sample pairs were removed from the liquid-nitrogen bath and a ^{22}Na source encapsulated in aluminum foil was sandwiched between them. The source-sample arrangement was then transferred to the helium cryostat of the lifetime spectrometer, where it was kept at 205 K during the spectra acquisition. The time between the removal of the samples from the liquid-nitrogen bath until reaching subzero degrees in the helium cryostat was approximately 1 min. The positron lifetime spectra were acquired using a digital lifetime spectrometer with a time resolution function of 174 ps (full width at half maximum). Each lifetime spectrum contained more than 10^6 counts and was analyzed after background and source correction ($\tau_{\text{source}} = 332$ ps, $I_{\text{source}} = 15\%$ [17]) using the program PALSFIT [18].

In the recrystallized state, the crystal structure of all samples was investigated by X-ray diffraction (XRD) measurements. The XRD diffraction patterns were measured in $\theta/2\theta$ geometry using a Bruker D8 Advance equipped with a Cu anode ($\lambda = 0.154$ nm). For data evaluation the software DIFFRAC.EVA was used. All samples were further characterized in the quenched state by electron backscatter diffraction (EBSD) and energy-dispersive X-ray spectroscopy (EDX). The EBSD and EDX measurements were conducted with a JEOL 7200F field-emission scanning electron microscope equipped with an Oxford Instruments EBSD/EDX system.

III. RESULTS AND DISCUSSION

The exact alloy compositions as obtained from EDX composition maps as well as the lattice constants as obtained from XRD measurements are given in Table I. Note that the compositions are further only given in the declarations of the nonequimolar alloys. Figure 1 shows the results of the EBSD and EDX mapping in the quenched state exemplary for the CoCrFeMnNi alloy. The EBSD phase mapping as shown in Fig. 1(a) clearly demonstrates the presence of only the face-centered cubic (fcc) phase in the quenched state of the alloy. It has to be noted, that the circumference of pores in the grains of the CoCrFeMnNi alloy are falsely detected as grain boundaries. The constituent distribution maps in Figs. 1(c)–1(g) show the homogeneous distribution of each element, with no evidence of any elemental segregation. Equivalent measure-

TABLE I. Alloy compositions in at. % as obtained from EDX composition maps. The error of the alloy composition is determined to ±0.20 at. %, and the error of the lattice constant is 0.001 Å.

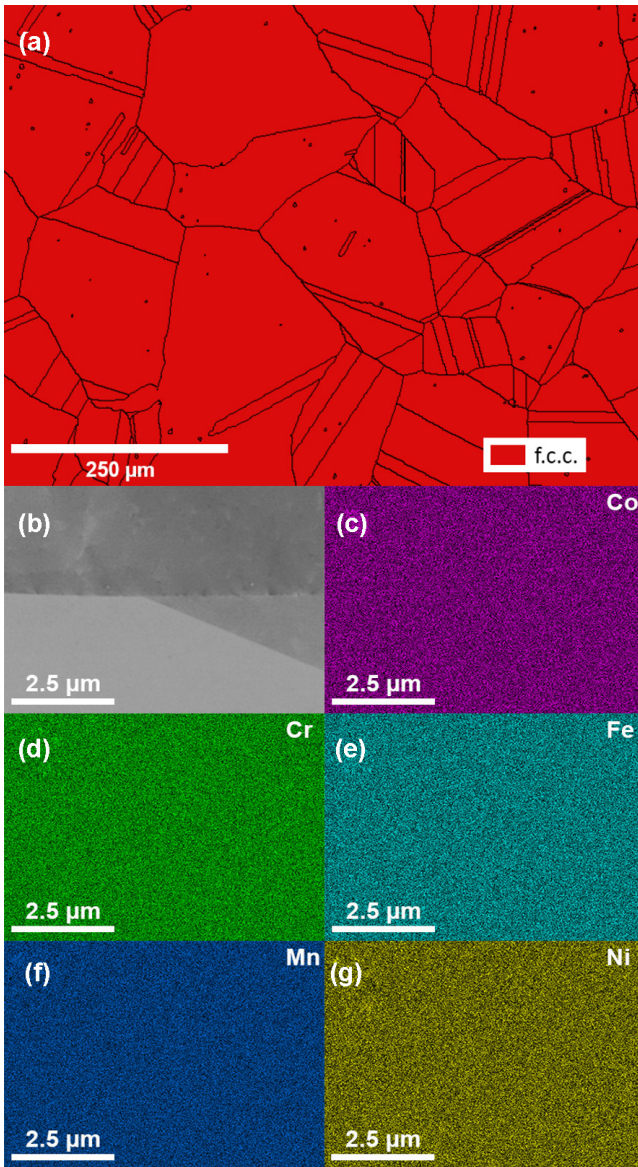| Alloy	Al	Co	Cr	Fe	Mn	Ni	Lattice constant $a/$Å
CrFeNi (0.3:1:0.2)			19.2	68.2		12.6	3.581
CrFeNi (1:1:1)			34.1	33.0		32.9	3.560
CoCrFeNi (1:1:1:1)		24.9	25.5	24.9		24.7	3.570
AlCoCrFeNi (0.3:1:1:1:1)	6.0	23.6	23.9	23.4		23.1	3.588
CoCrFeMnNi (1:1:1:1:1)		20.2	20.5	20.1	19.5	19.7	3.596

FIG. 1. EBSD and EDX measurements of the CoCrFeMnNi alloy in the quenched state. (a) EBSD phase mapping for a fcc phase with a lattice constant $a = 3.596$ Å. The circumference of pores inside the grains are falsely detected as grain boundaries. (c)–(g) Constituent distribution maps of the area shown in (b) for the alloy CoCrFeMnNi obtained by EDX mapping.

ments were conducted for all alloys investigated; in each case a single fcc phase and a homogeneous distribution of the constituents was observed (for all further EBSD and EDX results see the Supplemental Material [19]).

An analysis of the positron lifetime spectra was performed according to a two-state positron trapping model [20]. The two-state trapping model is generally valid for any type of material including one type of defect, which means that the experimentally observed positron lifetime spectrum consists of two exponential decays (after source correction). Hence, it is assumed that positrons annihilate either in a defect-free state exhibiting a lifetime τ_{bulk} or in the trapped state at a defect with a lifetime $\tau_{\text{defect}} = \tau_2$. The corresponding lifetime
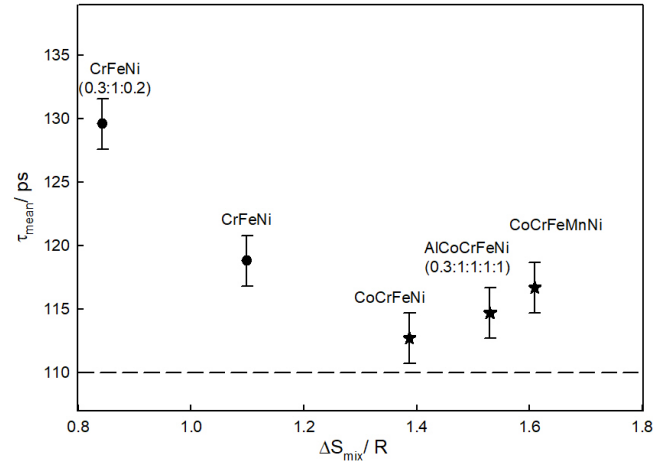

FIG. 2. Mean positron lifetime τ_{mean} as a function of the entropy of mixing ΔS_{mix}. The mean lifetime τ_{mean} is obtained from two-component analysis (black dots) or corresponds to the value from the single-component analysis (black stars). The dashed line corresponds to the defect-free bulk lifetime of pure Ni.

spectrum includes two components τ_1 and τ_2. From these the mean positron lifetime τ_{mean} is calculated according to $\tau_{\text{mean}} = \tau_1 I_1 + \tau_2 I_2$, where I_1 and I_2 are the corresponding intensities ($I_1 + I_2 = 100\%$). The bulk lifetime τ_{bulk} attributed to the annihilation of positrons in the defect-free bulk, is calculated by $\tau_{\text{bulk}} = (\frac{I_1}{\tau_1} + \frac{I_2}{\tau_2})^{-1}$. If there are no defects present only one lifetime component $\tau_1 = \tau_2 = \tau_{\text{bulk}}$ is detected.

In Fig. 2 the mean positron lifetime τ_{mean} for the set of alloys is shown as a function of their corresponding entropy of mixing ΔS_{mix} calculated according to $\Delta S_{\text{mix}} = -R \sum_i x_i \ln x_i$, with x the mole fraction of constituent i and R the gas constant. For comparison, the defect-free bulk lifetime of pure Ni is also given in Fig. 1 (dashed line, $\tau_{\text{Ni}} = 110$ ps [21]). For the alloys CrFeNi (0.3:1:0.2) and CrFeNi, the mean positron lifetime τ_{mean} is significantly higher than the expected, defect-free bulk lifetime. The mean positron lifetime decreases strongly with increasing mixing entropy ΔS_{mix} until it reaches a value slightly higher than the bulk lifetime of Ni as is the case for the alloys CoCrFeNi, AlCoCrFeNi (0.3:1:1:1:1), and CoCr-FeMnNi. The enhanced mean positron lifetime observed in CrFeNi (0.3:1:0.2) and CrFeNi indicates the existence of thermally induced, quenched-in vacancies in these alloys as is typical for metals after quenching (see, e.g., Ref. [22]). Contrarily, the low mean positron lifetime of the alloys with higher entropy of mixing CoCrFeNi, AlCoCrFeNi (0.3:1:1:1:1), and CoCrFeMnNi does not indicate the presence of a significant amount of quenched-in vacancies, which is rather unexpected.

For a closer understanding of these results, a component-wise analysis of the positron lifetime spectra is given in Table II. It includes the entropy of mixing ΔS_{mix}, the individual lifetime components τ_1 (τ_2), and the corresponding intensities I_1 (I_2) as well as the mean positron lifetime τ_{mean} and the bulk lifetime τ_{bulk} corresponding to the defect-free state. The confidence value of the best fits of the lifetime spectra as represented by the value of χ^2 in Table II is excellent for all samples; χ^2 even decreases towards higher mixing entropies. The positron lifetime spectra of the three-component alloys both contain two individual lifetime components τ_1 and τ_2

TABLE II. Mixing entropy ΔS_{mix}, individual positron lifetime components τ_1 (τ_2), corresponding intensities I_1 (I_2), and calculated mean positron lifetime τ_{mean} and bulk positron lifetime τ_{bulk} of the individual sample pairs measured after the heat treatment. The errors for the individual lifetime components are given by the numerical uncertainty $\Delta \tau_{1/2} = \pm 2$ ps and $\Delta I_{1/2} = \pm 3\%$, and the errors of the mean positron lifetime and the bulk positron lifetime are $\Delta \tau_{mean/bulk} = \pm 2$ ps.

Alloy	$\Delta S_{mix}/R$	τ_1/ps	I_1/%	τ_2/ps	I_2/%	τ_{mean}/ps	τ_{bulk}/ps	χ^2
CrFeNi (0.3:1:0.2)	0.84	104	72	195	28	130	120	1.066
CrFeNi (1:1:1)	1.10	117	97	190	3	119	118	1.169
CoCrFeNi (1:1:1:1)	1.39	113	100			113		1.131
AlCoCrFeNi (0.3:1:1:1:1)	1.53	115	100			115		1.110
CoCrFeMnNi (1:1:1:1:1)	1.61	117	100			117		1.096

with a similar bulk lifetime τ_{bulk} of 120 and 118 ps for CrFeNi (0.3:1:0.2) and CrFeNi, respectively. For the case of CrFeNi (0.3:1:0.2) the best fit resulted in a long-lifetime component $\tau_2 = 195$ ps with an intensity of $I_2 = 28\%$. For the fit of the lifetime spectrum of CrFeNi, τ_2 was held constant at a value of 190 ps, which is reasonable since both three-component alloys share the same fcc crystal structure and a very similar lattice constant (see Table I). For CrFeNi an intensity of $I_2 = 3\%$ was found for the second lifetime component τ_2. The theoretically calculated positron lifetimes in vacancies of the respective pure metals range from 184 to 201 ps [23]. Consequently, the second lifetime component τ_2 of the three-component alloys has to be attributed to the annihilation of positrons in vacancies, which confirms the existence of quenched-in vacancies within these alloys.

Applying a two-state trapping model, the concentration of vacancies c_v can be estimated from

$$\mu_d c_v = \frac{I_2}{I_1}\left(\frac{1}{\tau_{bulk}} - \frac{1}{\tau_2}\right), \qquad (1)$$

where μ_d is the positron trapping rate coefficient [20]. For the CrFeNi (0.3:1:0.2) alloy, a concentration of quenched-in vacancies of 1.3×10^{-5} can be estimated using a trapping rate coefficient $\mu_d = 1 \times 10^{14}$ s^{-1}. The equilibrium vacancy concentration $c_{v,eq}$ at a temperature T can be calculated according to

$$c_{v,eq} = \exp\left(\frac{S_f}{k_B}\right)\exp\left(-\frac{H_f}{k_B T}\right) \qquad (2)$$

with k_B the Boltzmann constant, and S_f and H_f as the vacancy formation entropy and enthalpy. This results in an equilibrium vacancy concentration of 10^{-4} at 1493 K using values for H_f and S_f as reported for γ-Fe [24,25]. These results are in line, taking into account losses of a certain amount of vacancies during quenching.

On the other hand, the positron lifetime spectra of the alloys with four and five components CoCrFeNi, AlCoCrFeNi (0.3:1:1:1:1), and CoCrFeMnNi exhibit only one single lifetime component. The obtained single lifetimes for CoCrFeNi, AlCoCrFeNi (0.3:1:1:1:1), and CoCrFeMnNi were 113, 115, and 117 ps, respectively. This slight increase of the positron lifetime τ_1 is consistent with an increasing lattice constant as derived from XRD measurements (see Table I). In previous studies similar values for the positron lifetime in the defect-free bulk of CoCrFeNi ($\tau_{bulk} = 108$ ps [13]) and CoCrFeMnNi ($\tau_{bulk} = 112$ ps [14]) were found. Furthermore, the bulk lifetimes of the four- and five-component alloys are only slightly enhanced compared to the value for pure Ni.

These deviations can also be explained due to differences in the packing densities of pure Ni and the investigated multicomponent alloys. Therefore, as already indicated by the mean positron lifetimes, also the componentwise analysis shows that no thermally generated vacancies can be detected in the alloys CoCrFeNi, AlCoCrFeNi (0.3:1:1:1:1), and CoCrFeMnNi by the means of positron annihilation spectroscopy. It seems that vacancy concentrations in these samples are exceptionally low.

The question arises whether lattice vacancies cannot be detected due to strong competitive positron trapping at defects with short positron lifetimes. Shallow traps with positron lifetimes substantially shorter than that of lattice vacancies are considered for coherent and semicoherent precipitates in Al alloys [26]. Such types of traps can safely be excluded for these concentrated solid-solution alloys due to their single-phase homogeneous structure. Above all, the value of the single short positron lifetime τ_1 observed in the four- and five-component samples (see Table II) corresponds to that expected for the free state.

Although any other interpretation of τ_1 than the free state appears unlikely, for the sake of completeness, we may hypothetically discuss scenarios where τ_1 would be associated with any kind of shallow trap. Assume, for instance, that τ_1 represents a mean value of two components, one of which arises from a shallow type of trap with a characteristic positron lifetime $\tau_{shallow} = 140$ ps and a relative intensity $I_{shallow} = 40\%$. For a mean value $\tau_1 = 115$ ps (AlCoCrFeNi sample, Table II), a value of 98 ps would follow for the other 60% component of the spectrum that is due to annihilation from the free state. These components (98 ps, 140 ps) both with substantial intensity should be clearly resolvable by numerical spectra analysis. This may no longer necessarily be the case if the intensity of $\tau_{shallow}$ is much lower and correspondingly the shorter component closer to τ_1; however, this would also mean that the trapping rate of such shallow traps are much lower and, therefore, this would hardly hinder a detection of a positron lifetime component associated with vacancies, if present.

An extreme limit in this scenario would pertain to the case that the τ_1 component arises from saturation trapping at shallow traps with $\tau_{shallow} = \tau_1$. Saturation trapping at such shallow traps indeed could mask competitive positron trapping at lattice vacancies. However, this can safely be ruled out, since there is neither a physical justification for positron traps with a lifetime as low as that of the free delocalized state, nor is there any reason for high concentration of such traps. An unambiguous proof that the absence of a vacancy-typical

positron lifetime component does not arise from the existence of other traps, may be accomplished by measuring the positron diffusion length by means of low- and monoenergetic positron beams.

It can be concluded that the only consistent explanation for the nonobservation of the long-lifetime component in the quenched CoCrFeNi, AlCoCrFeNi (0.3:1:1:1:1), and CoCrFeMnNi samples is that they exhibit vacancy concentrations lower than 10^{-6} at that point. Even under the assumption that the slightly enhanced τ_{mean} compared to the value τ_{bulk} for Ni might originate from vacancies that cannot be resolved as separate components, an upper limit for the vacancy concentration of 7×10^{-6} can be estimated. Therefore, there is either only a vanishingly small amount of vacancies being generated at temperatures close to their onset of melting, or the generated vacancies are inherently unstable and anneal out extremely fast. Both of these indications are completely unexpected for any densely packed multicomponent metallic crystal. Hence, also from this point of view, this type of ductile metallic material experiencing a very low or vanishingly small vacancy concentration can be regarded as a new class of material.

IV. CONCLUSION

In the present study, the method of positron annihilation lifetime spectroscopy is applied to show that in the concentrated solid-solution alloys CoCrFeNi, AlCoCrFeNi (0.3:1:1:1:1), and CoCrFeMnNi exhibiting a high entropy of mixing only a concentration of thermally generated vacancies smaller than 10^{-6} can be quenched-in. An identical heat treatment and quenching from temperatures close to their onset of melting was applied to a set of similar alloys with the same fcc crystal structure but with lower mixing entropy. For the latter case a vacancy concentration of 10^{-5} could be detected for CrFeNi (0.3:1:0.2). The mean positron lifetime of the samples decreases with increasing mixing entropy; furthermore, the lifetime spectra of the four- and five-component samples exhibit only one component. It can be concluded that in CoCrFeNi, CoCrFeMnNi, and AlCoCrFeNi (0.3:1:1:1:1) there is either only a vanishingly small fraction of vacancies present at temperatures near the onset of melting or the generated vacancies are inherently unstable. Since in the latter case an unreasonably small migration enthalpy for the self-diffusion process must be assumed, the former explanation seems to be more promising.

[1] B. Cantor, I. Chang, P. Knight, and A. Vincent, Mater. Sci. Eng. A **375**, 213 (2004).

[2] J.-W. Yeh, S.-K. Chen, S.-J. Lin, J.-Y. Gan, T.-S. Chin, T.-T. Shun, C.-H. Tsau, and S.-Y. Chang, Adv. Eng. Mater. **6**, 299 (2004).

[3] *High-Entropy Alloys*, edited by M. C. Gao, J.-W. Yeh, P. K. Liaw, and Y. Zhang, (Springer International Publishing, Cham, 2016).

[4] E. P. George, D. Raabe, and R. O. Ritchie, Nat. Rev. Mater. **4**, 515 (2019).

[5] Z. Li, K. G. Pradeep, Y. Deng, D. Raabe, and C. C. Tasan, Nature (London) **534**, 227 (2016).

[6] C.-Y. Hsu, C.-C. Juan, W.-R. Wang, T.-S. Sheu, J.-W. Yeh, and S.-K. Chen, Mater. Sci. Eng. A **528**, 3581 (2011).

[7] M.-H. Chuang, M.-H. Tsai, W.-R. Wang, S.-J. Lin, and J.-W. Yeh, Acta Mater. **59**, 6308 (2011).

[8] J. J. Zhang, X. L. Yin, Y. Dong, Y. P. Lu, L. Jiang, T. M. Wang, and T. J. Li, Mater. Res. Innovations **18**, S4-756 (2014).

[9] C. Lu, L. Niu, N. Chen, K. Jin, T. Yang, P. Xiu, Y. Zhang, F. Gao, H. Bei, S. Shi *et al.*, Nat. Commun. **7**, 1 (2016).

[10] F. Granberg, K. Nordlund, M. W. Ullah, K. Jin, C. Lu, H. Bei, L. M. Wang, F. Djurabekova, W. J. Weber, and Y. Zhang, Phys. Rev. Lett. **116**, 135504 (2016).

[11] M. Vaidya, K. G. Pradeep, B. S. Murty, G. Wilde, and S. V. Divinski, Acta Mater. **146**, 211 (2018).

[12] R. Krause-Rehberg and H. Leipner, *Positron Annihilation in Semiconductors* (Springer, New York, 1999).

[13] S. Abhaya, R. Rajaraman, S. Kalavathi, and G. Amarendra, J. Alloys Compd. **620**, 277 (2015).

[14] M. Elsayed, R. Krause-Rehberg, C. Eisenschmidt, N. Eißmann, and B. Kieback, Phys. Status Solidi A **215**, 1800036 (2018).

[15] K. Sugita, N. Matsuoka, M. Mizuno, and H. Araki, Scr. Mater. **176**, 32 (2020).

[16] G. Adetunji, R. Faulkner, and E. Little, J. Mater. Sci. **26**, 1847 (1991).

[17] Note that the source correction has been changed to $\tau_{source} = $ 293 ps, $I_{source} = 13\%$ for the CrFeNi (0.3:1:0.2) alloy.

[18] J. V. Olsen, P. Kirkegaard, N. J. Pedersen, and M. Eldrup, Phys. Status Solidi C **4**, 4004 (2007).

[19] See Supplemental Material at http://link.aps.org/supplemental/10.1103/PhysRevMaterials.4.060601 for EBSD, EDX, and XRD results of all investigated alloys.

[20] P. Hautojärvi, A. Dupasquier, and M. Manninen, *Positrons in Solids* (Springer, New York, 1979), Vol. 12.

[21] G. Dlubek, O. Brummer, N. Meyendorf, P. Hautojarvi, A. Vehanen, and J. Yli-Kauppila, J. Phys. F **9**, 1961 (1979).

[22] R. Cotterill, K. Petersen, G. Trumpy, and J. Traff, J. Phys. F **2**, 459 (1972).

[23] M. Puska and R. Nieminen, J. Phys. F **13**, 333 (1983).

[24] H. Matter, J. Winter, and W. Triftshäuser, Appl. Phys. **20**, 135 (1979).

[25] J. Burton, Phys. Rev. B **5**, 2948 (1972).

[26] B. Klobes, K. Maier, and T. Staab, Philos. Mag. **95**, 1414 (2015).

4.3 Diffusion-reaction model for the trapping and annihilation of positrons

4.3.1 Article 5: Positron trapping and annihilation at spherical extended defects and in precipitate-matrix composites

The article *Diffusion-reaction model for positron trapping and annihilation at spherical extended defects and in precipitate-matrix composites* was published in Physical Review B **97**, 224108 in June 2018 [11].

This work was done by Roland Würschum as first author and Laura Resch as second author. The exact solution of a diffusion-reaction model for the trapping and annihilation of positrons at small extended spherical defects was calculated by Roland Würschum. Laura Resch and Gregor Klinser did parts of the recalculation and cross-checking of the model and validated the model. Laura Resch also calculated solutions for various parameter sets and gave the graphical representations.

In this paper, the diffusion-reaction model was set up and solved for the case of positron trapping and annihilation in spherical extended defects embedded in a matrix containing point defects, where competitive reaction rate-limited trapping is taken into account. The diffusion-reaction limited trapping is mathematically handled by means of Laplace transformation, yielding closed-form expressions for the major positron annihilation parameters. In addition, the model was extended for the trapping and annihilation of positrons at larger precipitates, where not only positron trapping from the matrix into the precipitate-matrix interface but also trapping from the precipitate into the interface is considered. This solutions can be applied to the trapping and annihilation of positrons in precipitates evolving during age hardening of light weight alloys, and thus add another aspect to previous experimental studies on this topic (see also section 4.3.2, Addendum).

Diffusion-reaction model for positron trapping and annihilation at spherical extended defects and in precipitate-matrix composites

Roland Würschum,[*] Laura Resch, and Gregor Klinser

Institute of Materials Physics, Graz University of Technology, Petersgasse 16, A-8010 Graz, Austria

The exact solution of a diffusion-reaction model for the trapping and annihilation of positrons in small extended spherical defects (clusters, voids, small precipitates) with competitive rate-limited trapping in vacancy-type point defects is presented. Closed-form expressions are obtained for the mean positron lifetime and for the intensities of the two positron lifetime components associated with trapping at defects. The exact solutions can be conveniently applied for the analysis of experimental data and allow an assessment in how far the usual approach, which takes diffusion limitation into account by means of effective diffusion trapping rates, is appropriate. The model is further extended for application to larger precipitates where diffusion- and reaction-limited trapping is not only considered for the trapping from the matrix into the precipitate-matrix interface, but also for the trapping from inside the precipitates into the interfaces. This makes the model applicable to all types of composite structures where spherical objects are embedded in a matrix, irrespective of their size and their number density.

I. INTRODUCTION

The versatile technique of positron annihilation makes use of the fact that positrons (e^+) are trapped at free volume-type defects which allows their detection by a specific variation of the positron-electron annihilation characteristics [1–4]. Whereas the kinetics of e^+ trapping at vacancy-type point defects can be well described by rate theory (so-called simple trapping model), it is well known that for trapping at extended defects like grain boundaries, interfaces, voids, clusters, or precipitates, diffusion limitation of the trapping process may be an issue. Diffusion-limited positron trapping at interfaces and grain boundaries has been quantitatively modeled by several groups, ranging from entirely diffusion-controlled trapping [5], diffusion-reaction-controlled trapping including detrapping [6–9], up to diffusion-reaction-controlled trapping at grain boundaries and competitive transition-limited trapping at point defects in crystals [8,10–12].

Compared to grain boundaries, diffusion-limited e^+ trapping at voids and clusters has not been studied in such detail despite the undoubted relevance of positron annihilation for studying this important class of defects [13–15]. One approach to deal with diffusion-limited trapping is based on effective diffusion trapping rates which then allow an implementation in standard rate theory (e.g., [14]). Diffusion-limited trapping at pointlike defects was studied by Dryzek [16] for the one-dimensional case. A full treatment of e^+ trapping and annihilation in voids in the framework of diffusion-reaction theory was given by Nieminen *et al.* [17]. This treatment of Nieminen *et al.* [17] is conceptionally analogous to the subsequent work of Dupasquier *et al.* [6] for diffusion-limited e^+ trapping at grain boundaries, both of which lead to solutions exclusively in terms of infinite series.

Another treatment of the diffusion-reaction problem of e^+ trapping at grain boundaries was given by Würschum and Seeger [7] which yields closed-form expressions for the mean e^+ lifetime and the intensity of the annihilation component associated with the trapped state. This approach is applied in this work to the diffusion-reaction problem of e^+ trapping and annihilation in spherical extended defects (voids, clusters, precipitates).[1] Following our earlier further work on grain boundaries [11], now in addition competitive reaction rate-limited trapping at point defects is taken into account. The present treatment yields closed-form expressions of the major e^+ annihilation parameters for this application-relevant case of competitive e^+ trapping in voids and point defects. These closed-form expressions allow deeper insight in the physical details of e^+ annihilation characteristics as well as an assessment of the so far often used approach based on effective diffusion trapping rates. Above all, the results can be conveniently applied for the analysis of experimental data.

In a further part, the model presented here and the previous model on positron trapping at grain boundaries are merged in order to study precipitates embedded in matrix. Here, diffusion- and reaction-limited trapping is considered for both the trapping from the matrix into the precipitate-matrix interface and for the trapping from inside the precipitates into the interfaces.

II. MODEL

The model describes positron (e^+) trapping and annihilation in voids in the general case that both the e^+ diffusion and the transition reaction has to be taken into account

---

[1]For the sake of simplicity, representatively for all kinds of spherical extended defects (voids, clusters, or precipitates) the term voids is used in the following.
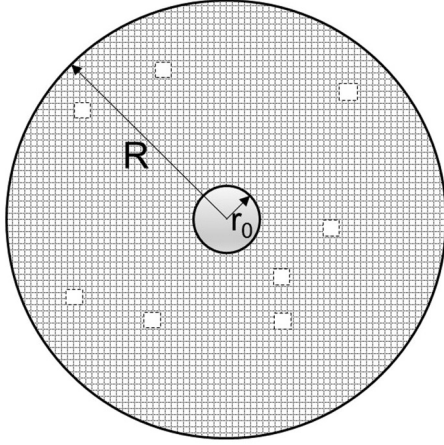
---

*wuerschum@tugraz.at

FIG. 1. Geometry of the diffusion-reaction model: spherical voids of radius r_0 are located in a lattice with homogeneously distributed vacancy-type defects (open square) in which reaction-controlled trapping occurs. The outer radius R of the diffusion sphere defines the void concentration.

(so-called diffusion-reaction-controlled trapping process). In order to cover more complex cases, competitive transition-limited trapping at vacancy-type points defects is also considered (see Fig. 1). This procedure follows our earlier study where concomitant positron trapping at grain boundaries and at point defects in crystallites has been considered [11].

The behavior of the positrons is described by their bulk (free) lifetime τ_f, by their lifetime (τ_t) in the voids, by their lifetime (τ_v) in the vacancy-type point defects in the lattice (matrix), and by their bulk diffusivity D. Trapping at the point defects of the matrix is characterized by the specific e^+ trapping rate σ_v (unit s^{-1}), as usual. The voids are considered as spherical-shaped extended defects (radius r_0) with a specific trapping rate α (unit $m\,s^{-1}$) which is related to the surface area of the void. In units of s^{-1} the specific trapping rate of voids reads as

$$\sigma_t = \frac{\alpha 4\pi r_0^2}{\Omega}, \tag{1}$$

where Ω denotes the atomic volume.

The temporal and spatial evolution of the density ρ_l of free positrons in the lattice is governed by

$$\frac{\partial \rho_l}{\partial t} = D\nabla^2 \rho_l - \rho_l\left(\frac{1}{\tau_f} + \sigma_v C_v\right), \tag{2}$$

where C_v denotes the concentration of vacancy-type point defects in the matrix. The positrons trapped in the voids are described in terms of their density ρ_t obeying the rate equation

$$\frac{d\rho_t}{dt} = \alpha\rho_l(r_0,t) - \frac{1}{\tau_t}\rho_t. \tag{3}$$

The temporal evolution of the number N_v of e^+ trapped in the point defects in the lattice is given by

$$\frac{dN_v}{dt} = -\frac{1}{\tau_v}N_v + \sigma_v C_v N_f, \tag{4}$$

where the number N_f of positrons in the free state follows from integration of ρ_l:

$$N_f = \int \rho_l dV. \tag{5}$$

The continuity of the e^+ flux at the boundary between the lattice and the void surface is expressed by[2]

$$D\nabla\rho_l\Big|_{r=r_0} - \alpha\rho_l(r_0,t) = 0. \tag{6}$$

The outer radius R of the diffusion sphere is related to the void concentration

$$C_t = \frac{3\Omega}{4\pi R^3}. \tag{7}$$

The outer boundary condition

$$\frac{\partial \rho_l}{\partial r}\Big|_{r=R} = 0 \tag{8}$$

reflects the vanishing e^+ flux through the outer border ($r = R$) of the diffusion sphere. This boundary condition is the same as applied earlier in a quite different diffusion-reaction model of ortho-para conversion of positronium at reaction centers [18].

As initial condition we adopt the picture that at $t = 0$ all thermalized positrons are in the free state and homogeneously distributed in the lattice, i.e., initial density $\rho_l = \rho_l(0)$, $\rho_t(0) = 0$, $N_v(0) = 0$. Under this initial condition, the solution of Eq. (2) exhibits spherical symmetry.

Up to this point, the above formulated diffusion-reaction problem is identical to that of Nieminen *et al.* [17] apart from the additional rate-limited trapping at vacancy-type point defects which is considered here. However, compared to [17], in the following part of this work the time dependence is handled by means of Laplace transformation which will lead to the more convenient closed-form solutions. Applying the Laplace transformation

$$\tilde{\rho}_{l,t}(p) = \int_0^\infty \exp(-pt)\rho_{l,t}(t)dt,$$

$$\tilde{N}_{v,f}(p) = \int_0^\infty \exp(-pt)N_{v,f}(t)dt \tag{9}$$

leads to the basic equations

$$\frac{d^2\tilde{\rho}_l}{dr^2} + \frac{2}{r}\frac{d\tilde{\rho}_l}{dr} - \gamma^2\tilde{\rho}_l = -\frac{\rho_l(0)}{D} \tag{10}$$

with

$$\gamma^2 = \gamma^2(p) = \frac{\tau_f^{-1} + \sigma_v C_v + p}{D} \tag{11}$$

_____

[2]Note the negative sign in contrast to the model of e^+ trapping at grain boundaries (e.g., [11]) where the corresponding continuity equation refers to the outer boundary.

and

$$\tilde{\rho}_t = \frac{\alpha \tilde{\rho}_l(r_0, p)}{\tau_t^{-1} + p}, \tag{12}$$

$$\tilde{N}_v = \frac{\sigma_v C_v}{\tau_v^{-1} + p} \int_{r_0}^{R} 4\pi r^2 \tilde{\rho}_l(r, p) dr, \tag{13}$$

with the boundary conditions

$$D \frac{d\tilde{\rho}_l}{dr}\bigg|_{r=r_0} - \alpha \tilde{\rho}_l(r_0, p) = 0 \tag{14}$$

and

$$\frac{d\tilde{\rho}_l}{dr}\bigg|_{r=R} = 0. \tag{15}$$

The solution of the differential equation (10) satisfying Eqs. (14) and (15) can be written as

$$\tilde{\rho}_l(r, p) = A\, i_0^{(1)}(\gamma r) + B\, i_0^{(2)}(\gamma r) + \frac{\rho_l(0)}{\tau_f^{-1} + \sigma_v C_v + p} \tag{16}$$

with

$$A := \alpha \frac{\rho_l(0)}{\tau_f^{-1} + \sigma_v C_v + p} \quad \frac{i_1^{(2)}(\gamma R)}{-D\gamma F_1 + \alpha F_2},$$

$$B := \alpha \frac{\rho_l(0)}{\tau_f^{-1} + \sigma_v C_v + p} \quad \frac{i_1^{(1)}(\gamma R)}{D\gamma F_1 - \alpha F_2} \tag{17}$$

and

$$F1 = i_1^{(2)}(\gamma r_0) i_1^{(1)}(\gamma R) - i_1^{(1)}(\gamma r_0) i_1^{(2)}(\gamma R),$$

$$F2 = i_0^{(2)}(\gamma r_0) i_1^{(1)}(\gamma R) - i_0^{(1)}(\gamma r_0) i_1^{(2)}(\gamma R). \tag{18}$$

$i_n^{(1)}$ and $i_n^{(2)}$ ($n = 0, 1$) denote the modified spherical Bessel functions of order n [19]:

$$i_n^{(1)}(z) := \left(\frac{\pi}{2z}\right)^{1/2} I_{n+1/2}(z),$$

$$i_0^{(1)} = \frac{\sinh z}{z}, \quad i_1^{(1)} = \frac{\cosh z}{z} - \frac{\sinh z}{z^2}, \tag{19}$$

$$i_n^{(2)}(z) := \left(\frac{\pi}{2z}\right)^{1/2} I_{-n-1/2}(z),$$

$$i_0^{(2)} = \frac{\cosh z}{z}, \quad i_1^{(2)} = \frac{\sinh z}{z} - \frac{\cosh z}{z^2}, \tag{20}$$

where $I_{\pm n \pm 1/2}(z)$ represents the Bessel function.

The basis for analyzing positron annihilation experiments is the total probability $n(t)$ that an e^+ implanted at $t = 0$ has not yet been annihilated at time t. Here, $n(t)$ is given by the number density of e^+ per lattice sphere at time t:

$$n(t) = \frac{1}{\frac{4}{3}\pi\left(R^3 - r_0^3\right)\rho_l(0)} \left\{ \int_{r_0}^{R} 4\pi r^2 \rho_l(r, t) dr + 4\pi r_0^2 \rho_t(t) + N_v(t) \right\}. \tag{21}$$

The Laplace transform of $n(t)$ can be calculated taking into account the solution of $\tilde{N}_v$ [Eq. (13)] and the solution of the differential equation (16) which yields

$$\tilde{n}(p) = \frac{1}{\frac{4}{3}\pi\left(R^3 - r_0^3\right)\rho_l(0)} \left\{ \left(1 + \frac{\sigma_v C_v}{\tau_v^{-1} + p}\right) \int_{r_0}^{R} 4\pi r^2 \tilde{\rho}_l(r, p) dr + 4\pi r_0^2 \tilde{\rho}_t(p) \right\}. \tag{22}$$

Solving the integral after substituting $\tilde{\rho}_t(p)$ by Eq. (12), insertion of A and B [Eq. (17)], yields after some algebra

$$\tilde{n}(p) = \frac{1}{t_{fc}^2 t_v t_t} \left\{ t_{vc} t_{fc} t_t + \frac{K(t_{fc} t_v - t_{vc} t_t)(\gamma \hat{R} - \tanh(\gamma \hat{R})[1 - \gamma^2 r_0 R])}{\gamma \hat{R} - \tanh(\gamma \hat{R})[1 - \gamma^2 r_0 R] + \frac{\alpha r_0}{D}[\gamma R - \tanh(\gamma \hat{R})]} \right\} \tag{23}$$

with

$$K = \frac{3\alpha r_0^2}{R^3 - r_0^3}, \tag{24}$$

$$\hat{R} = R - r_0, \tag{25}$$

and the abbreviations

$$t_t = \tau_t^{-1} + p; \qquad t_v = \tau_v^{-1} + p;$$

$$t_{vc} = \tau_v^{-1} + \sigma C + p; \quad t_{fc} = \tau_f^{-1} + \sigma C + p. \tag{26}$$

The Laplace transform $\tilde{n}(p)$ [Eq. (23)] represents the solution of the present diffusion and trapping model from which both the mean positron lifetime and the positron lifetime spectrum can be deduced. The mean positron lifetime $\overline{\tau}$ is obtained by

taking the Laplace transform at $p = 0$:

$$\overline{\tau} = \tilde{n}(p = 0) = \int_0^\infty n(t) dt. \tag{27}$$

The positron lifetime spectrum follows from $\tilde{n}(p)$ by means of Laplace inversion. The single poles $p = -\lambda_i$ of $\tilde{n}(p)$ in the complex p plane define the decay rates λ_i ($i = 0, 1, 2, \dots$) of the positron lifetime spectrum:

$$n(t) = \sum_{i=0}^{\infty} I_i \exp(-\lambda_i t), \tag{28}$$

where I_i denote the relative intensities.

III. ANALYSIS

At first, we consider the most important case that e^+ trapping exclusively occurs at voids, i.e., we omit e^+ trapping

at point defects in the lattice ($C_v = 0$). For this case, we present the solution of the general diffusion-reaction theory (Sec. III A) and compare it with the limiting cases of entirely reaction-controlled trapping (Sec. III B) and entirely diffusion-controlled trapping (Sec. III C). Finally, the case of competitive reaction-controlled trapping at lattice defects is considered (Sec. III D) and an extension to larger precipitates is

presented for describing precipitate-matrix composite structures (Sec. III E).

A. General case with trapping at voids, exclusively ($C_v = 0$)

For negligible trapping at vacancies within the lattice ($C_v = 0$), the diffusion-reaction model according to Eq. (23) yields for positron trapping in voids as the single type of trap

$$\tilde{n}(p) = \frac{1}{\tau_f^{-1} + p}\left\{1 + \frac{K\left(\tau_f^{-1} - \tau_t^{-1}\right)}{\left(\tau_t^{-1} + p\right)\left(\tau_f^{-1} + p\right)}\quad\frac{\gamma\hat{R} - \tanh(\gamma\hat{R})[1 - \gamma^2 r_0 R]}{\gamma\hat{R} - \tanh(\gamma\hat{R})[1 - \gamma^2 r_0 R] + \frac{\alpha r_0}{D}[\gamma R - \tanh(\gamma\hat{R})]}\right\} \quad (29)$$

and, hence, for the mean positron lifetime

$$\overline{\tau} = \tilde{n}(0) = \tau_f\left\{1 + K(\tau_t - \tau_f)\frac{\gamma_0\hat{R} - \tanh(\gamma_0\hat{R})\left[1 - \gamma_0^2 r_0 R\right]}{\gamma_0\hat{R} - \tanh(\gamma_0\hat{R})\left[1 - \gamma_0^2 r_0 R\right] + \frac{\alpha r_0}{D}[\gamma_0 R - \tanh(\gamma_0\hat{R})]}\right\}. \quad (30)$$

The pole of Eq. (29) for $p = -\tau_t^{-1}$ corresponds to the positron lifetime component τ_t of the void-trapped state for which the following intensity is obtained:

$$I_t = \frac{K}{\tau_f^{-1} - \tau_t^{-1}}\quad\frac{\gamma_t\hat{R} - \tanh(\gamma_t\hat{R})\left[1 - \gamma_t^2 r_0 R\right]}{\gamma_t\hat{R} - \tanh(\gamma_t\hat{R})\left[1 - \gamma_t^2 r_0 R\right] + \frac{\alpha r_0}{D}[\gamma_t R - \tanh(\gamma_t\hat{R})]}. \quad (31)$$

In Eqs. (29), (30), and (31),

$$\gamma^2 = \frac{\tau_f^{-1} + p}{D}; \quad \gamma_0^2 = \frac{\tau_f^{-1}}{D}; \quad \gamma_t^2 = \frac{\tau_f^{-1} - \tau_t^{-1}}{D}. \quad (32)$$

In addition to the annihilation component τ_t^{-1} of the void-trapped state, $\tilde{n}(p)$ [Eq. (29)] comprises a sequence of first-order poles $p = -\lambda_{0,j}$ for $\lambda_{0,j} > \tau_f^{-1}$. These components $\lambda_{0,j}$, which define the fast decay rates ($\lambda_{0,j} > \tau_f^{-1}$) of the e^+ lifetime spectrum, are given by the solutions of the transcendental equation

$$\tan(\gamma^\star\hat{R}) = \frac{\gamma^\star(\alpha r_0 R + D\hat{R})}{D(1 + \gamma^{\star 2} r_0 R) + \alpha r_0} \quad (33)$$

with

$$\gamma^{\star 2} = \frac{\lambda_{0,j} - \tau_f^{-1}}{D} \quad (34)$$

in agreement with the aforementioned earlier work of Nieminen et al. [17].[3,4] As usual for this kind of diffusion-reaction problem (see, e.g., [11]), the intensities of these decay rates rapidly decrease. Experimentally, only a single fast decay rate can be resolved in addition to the decay rate τ_t^{-1} of the trapped state. An experimental two-component e^+ lifetime spectrum is practically entirely defined by $\overline{\tau}$ [Eq. (30)] and by τ_t with the corresponding intensity I_t [Eq. (31)].

The appearance of a second-order pole in Eq. (29) at $p = -\tau_f^{-1}$ (i.e., $\gamma = 0$) is spurious. Closer inspection by applying Taylor expansion shows that the intensity associated with this pole cancels.

Following the consideration of Dryzek [20], in analogy to the mean e^+ lifetime [Eq. (30)] a respective relation for the mean line-shape parameter $\overline{S}$ of Doppler broadening of the positron-electron annihilation can be given:

$$\overline{S} = S_f\left\{1 + K(S_t - S_f)\frac{\gamma_0\hat{R} - \tanh(\gamma_0\hat{R})\left[1 - \gamma_0^2 r_0 R\right]}{\gamma_0\hat{R} - \tanh(\gamma_0\hat{R})\left[1 - \gamma_0^2 r_0 R\right] + \frac{\alpha r_0}{D}[\gamma_0 R - \tanh(\gamma_0\hat{R})]}\right\}, \quad (35)$$

where S_f and S_t denote the line-shape parameters of the free and trapped states, respectively.

For the sake of completeness, we quote $\tilde{n}(p)$ without derivation for the case that at time zero positrons are homogeneously distributed in the voids and the lattice, i.e., for the initial condition $\rho_t(0) = r_0\rho_l(0)/3$:

$$\tilde{n}(p) = \frac{1}{\tau_f^{-1} + p}\left\{1 + \frac{r_0^3}{R^3}\frac{\tau_f^{-1} - \tau_t^{-1}}{\tau_t^{-1} + p} + \frac{3\alpha r_0^2}{R^3}\frac{\tau_f^{-1} - \tau_t^{-1}}{\left(\tau_t^{-1} + p\right)\left(\tau_f^{-1} + p\right)}\frac{\gamma\hat{R} - \tanh(\gamma\hat{R})\left[1 - \gamma^2 r_0 R\right]}{\gamma\hat{R} - \tanh(\gamma\hat{R})[1 - \gamma^2 r_0 R] + \frac{\alpha r_0}{D}[\gamma R - \tanh(\gamma\hat{R})]}\right\}. \quad (36)$$

---

[3]Equation (33) is identical to the corresponding Eq. (15) in the work of Nieminen et al. when ν in [17] is identified with $4\pi r_0^2\alpha$.

[4]We note that the same problem was treated in the framework of a more general theoretical approach by Kögel [8]. The quoted specific function in dependence of $\gamma\hat{R}$ [Eq. (75) in [8]], which determines the mean e^+ lifetime and the intensity of the trap component, however, is not readily applicable.

Equation (36) includes in the limiting case of negligible trapping ($\alpha = 0$) as mean e^+ lifetime $\overline{\tau} = \tilde{n}(0) = [(R^3 - r_0^3)\tau_f + r_0^3 \tau_t]/R^3$ the expected volume-averaged mean value of τ_f and τ_t.

B. Limiting case of entirely reaction-limited trapping ($C_v = 0$)

If the e^+ diffusivity is high ($\gamma \hat{R} \ll 1$), the hyperbolic tangent in Eq. (29) can be expanded. Expansion up to the third order

$$\tanh(z) \approx z - \frac{z^3}{3} \qquad (37)$$

yields the mean e^+ lifetime

$$\overline{\tau} = \tau_f \frac{1 + K\tau_t}{1 + K\tau_f} \qquad (38)$$

and for the e^+ lifetime component τ_t the intensity

$$I_t = \frac{K}{\tau_f^{-1} + K - \tau_t^{-1}} \qquad (39)$$

with K according to Eq. (24). Equations (38) and (39) are the well-known solutions of the simple trapping model when we identify K for vanishing defect volume with the trapping rate $\sigma_t C_t$ [Eqs. (1) and (7)]. Note that the standard trapping model does not take into account the finite defect volume (here $4\pi r_0^3/3$) and, therefore, does not contain the subtrahend r_0^3 as in Eq. (24). With this subtrahend, Eqs. (38) and (39) correctly contain the exact values $\overline{\tau} = \tau_t$ and $I_t = 1$ as limiting case for $R = r_0$.

C. Limiting case of entirely diffusion-limited trapping ($C_v = 0$)

The present solution includes in the limiting special case $\alpha \to \infty$ the relationships for an entirely diffusion-limited trapping, i.e., for Smoluchowski-type boundary condition

$$\rho_l(r_0, t) = 0. \qquad (40)$$

In this limit one obtains from the Laplace transform [Eq. (29)] the mean e^+ lifetime

$$\overline{\tau} = \tau_f \left\{ 1 + \frac{3r_0 D}{R^3 - r_0^3}(\tau_t - \tau_f) \right.$$
$$\left. \times \frac{\gamma_0 \hat{R} - \tanh(\gamma_0 \hat{R})[1 - \gamma_0^2 r_0 R]}{\gamma_0 R - \tanh(\gamma_0 \hat{R})} \right\} \qquad (41)$$

and for the trap component τ_t the intensity

$$I_t = \frac{3r_0 D}{R^3 - r_0^3} \frac{1}{\tau_f^{-1} - \tau_t^{-1}} \frac{\gamma_t \hat{R} - \tanh(\gamma_t \hat{R})[1 - \gamma_t^2 r_0 R]}{\gamma_t R - \tanh(\gamma_t \hat{R})} \qquad (42)$$

with γ_0, γ_t according to Eq. (32).

D. General case with voids *and* lattice vacancies

The positron annihilation characteristics of diffusion-reaction-controlled trapping at voids and concomitant transition-limited trapping at point defects in the lattice is given by Eq. (23) in combination with Eqs. (27) and (28). The mean positron lifetime [Eq. (27)], obtained from Eq. (23) for $p = 0$, reads as in the general case

$$\overline{\tau} = \frac{1}{\left(\tau_f^{-1} + \sigma_v C_v\right)^2} \left\{ \left(\tau_f^{-1} + \sigma_v C_v\right)\left(\tau_v^{-1} + \sigma_v C_v\right)\tau_v + \frac{K\left(\left(\tau_f^{-1} + \sigma_v C_v\right)\tau_t - \left(\tau_v^{-1} + \sigma_v C_v\right)\tau_v\right)(\gamma_0 \hat{R} - \tanh(\gamma_0 \hat{R})[1 - \gamma^2 r_0 R])}{\gamma_0 \hat{R} - \tanh(\gamma_0 \hat{R})[1 - \gamma_0^2 r_0 R] + \frac{\alpha r_0}{D}[\gamma_0 R - \tanh(\gamma_0 \hat{R})]} \right\} \qquad (43)$$

with

$$\gamma_0^2 = \frac{\tau_f^{-1} + \sigma_v C_v}{D}. \qquad (44)$$

In addition to the pole $p = -\tau_t^{-1}$ which characterizes the void trapped state, $\tilde{n}(p)$ [Eq. (23)] contains the further defect-related pole $p = -\tau_v^{-1}$ for the vacancy-type defect in the lattice. From the residues of $\tilde{n}(p)$ [Eq. (23)], the corresponding relative intensities

$$I_t = \frac{K}{\tau_f^{-1} + \sigma_v C_v - \tau_t^{-1}} \quad \frac{\gamma_t \hat{R} - \tanh(\gamma_t \hat{R})[1 - \gamma_t^2 r_0 R]}{\gamma_t \hat{R} - \tanh(\gamma_t \hat{R})[1 - \gamma_t^2 r_0 R] + \frac{\alpha r_0}{D}[\gamma_t R - \tanh(\gamma_t \hat{R})]} \qquad (45)$$

and

$$I_v = \frac{\sigma_v C_v}{\tau_f^{-1} + \sigma_v C_v - \tau_v^{-1}} \left\{ 1 - \frac{K}{\tau_f^{-1} + \sigma_v C_v - \tau_v^{-1}} \quad \frac{\gamma_v \hat{R} - \tanh(\gamma_v \hat{R})[1 - \gamma_v^2 r_0 R]}{\gamma_v \hat{R} - \tanh(\gamma_v \hat{R})[1 - \gamma_v^2 r_0 R] + \frac{\alpha r_0}{D}(\gamma_v R - \tanh(\gamma_v \hat{R}))} \right\} \qquad (46)$$

are deduced with

$$\gamma_{t,v}^2 = \frac{\tau_f^{-1} + \sigma_v C_v - \tau_{t,v}^{-1}}{D}. \qquad (47)$$

E. Extended model for larger precipitates with e^+ trapping from both sides of precipitate-matrix interface

The model presented above describes e^+ annihilation from a trapped state (τ_t) in spherical defects. Particularly, for larger

precipitate sizes a situation may prevail where e^+ annihilation inside the precipitates occurs from a free state with a characteristic e^+ lifetime τ_p and where also from this free precipitate state positrons may get trapped into the spherical interfacial shell between the precipitate and the surrounding matrix. This means that the precipitates are characterized by two components, one corresponding to the precipitate volume (τ_p) and one corresponding to the trapped state in the matrix-precipitate interface (τ_t).

The present model can be extended in a straightforward manner to this case under the reasonable assumption that the e^+ trapping from inside the precipitates is entirely reaction controlled. This is pretty well fulfilled as long as the precipitate diameter is remarkably lower than the e^+ diffusion length in the precipitate.[5] In this case, the extension can be described by an additional rate equation for the temporal evolution of the number N_p of e^+ inside the precipitates

$$\frac{dN_p}{dt} = -\left(\frac{1}{\tau_p} + \frac{3\beta}{r_0}\right)N_p, \tag{48}$$

where β denotes the specific trapping rate (in units of m/s) at the spherical interfacial shell. This trapping from inside the precipitates, which occurs in addition to the diffusion- and reaction-limited trapping into the interfacial shell from the surrounding matrix, has to be taken into account in the rate equation for ρ_t [Eq. (3)] by the additional summand $\beta\rho_p(t)$ with the number density $\rho_p = 3N_p/(4\pi r_0^3)$ of e^+ in the precipitate.

Assuming a homogeneous distribution of e^+ at time zero in the matrix and the precipitate [$\rho_l(0) = \rho_p(0)$] without e^+ in the trapped state [$\rho_t(0) = 0$] for $t = 0$, one obtains with the Laplace transform of Eq. (48)

$$\tilde{N}_p = \frac{N_p(0)}{\tau_p^{-1} + \frac{3\beta}{r_0} + p} \tag{49}$$

the additional summand

$$\left(\frac{r_0}{R}\right)^3\left(\frac{\frac{3\beta}{r_0}}{\tau_t^{-1} + p} + 1\right)\frac{1}{\tau_p^{-1} + \frac{3\beta}{r_0} + p} \tag{50}$$

in Eq. (23) of $\tilde{n}(p)$. Moreover, in the brackets of Eq. (23) the first summand is extended by the weighting factor $[1 - (r_0/R)^3]$ and the trapping rate K [Eq. (24)] in the second summand is replaced by $3\alpha r_0^2/R^3$.

For $\underline{C_v = 0}$ this leads to the mean e^+ lifetime

$$\bar{\tau} = \tau_f\left\{\left[1 - \left(\frac{r_0}{R}\right)^3\right] + \frac{3\alpha r_0^2}{R^3}(\tau_t - \tau_f)\frac{\gamma_0\hat{R} - \tanh(\gamma_0\hat{R})[1 - \gamma_0^2 r_0 R]}{\gamma_0\hat{R} - \tanh(\gamma_0\hat{R})[1 - \gamma_0^2 r_0 R] + \frac{\alpha r_0}{D}[\gamma_0 R - \tanh(\gamma_0\hat{R})]}\right\}$$
$$+ \left(\frac{r_0}{R}\right)^3\tau_t\frac{\tau_t^{-1} + \frac{3\beta}{r_0}}{\tau_p^{-1} + \frac{3\beta}{r_0}}, \tag{51}$$

as compared to Eq. (30). Equation (51) includes in the limiting case of negligible trapping ($\alpha = \beta = 0$) as mean e^+ lifetime $\bar{\tau} = [(R^3 - r_0^3)\tau_f + r_0^3\tau_p]/R^3$ the expected volume-averaged mean value of τ_f and τ_p.

The additional pole for $p = -(\tau_p^{-1} + 3\beta/r_0)$ of $\tilde{n}(p)$ yields the intensity of the e^+ lifetime component τ_p in the precipitate:

$$I_p = \left(\frac{r_0}{R}\right)^3\left(1 - \frac{\frac{3\beta}{r_0}}{\tau_p^{-1} + \frac{3\beta}{r_0} - \tau_t^{-1}}\right). \tag{52}$$

Apart from the weighting prefactor $[(r_0/R)^3]$, I_p corresponds to the solution of the simple trapping model.[6] Without trapping ($\beta = 0$), I_p simply takes the form of the weighting prefactor $(r_0/R)^3$.

Since e^+ trapping into the precipitate-matrix interface occurs both from inside the precipitate and from the surrounding matrix, the intensity of the trap component τ_t is given by the sum

$$I_t = I_t^{\text{precip}} + I_t^{\text{matrix}} \text{ with } I_t^{\text{precip}} = \left(\frac{r_0}{R}\right)^3\frac{\frac{3\beta}{r_0}}{\tau_p^{-1} + \frac{3\beta}{r_0} - \tau_t^{-1}}, \tag{53}$$

where I_t^{matrix} corresponds to the intensity I_t according to Eq. (31) with K replaced by $3\alpha r_0^2/R^3$.[7]

We note that the two e^+ trapping processes into the precipitate-matrix interface, namely, that from inside the precipitate and that from the surrounding matrix, are completely decoupled. The trapping process from inside the precipitate can, therefore, be treated independently. This also means that the process is not restricted to the case of entirely reaction-controlled trapping as given above, but that e^+ trapping at the precipitate-matrix interface from inside the spherical precipitates can also be treated in the framework of diffusion-reaction theory. Hence, the available solutions for diffusion- and reaction-limited trapping at grain boundaries (GBs) of spherical crystallites [7,11] can be directly applied. For this purpose, the solutions for the GB model have simply to be weighted by the factor $(r_0/R)^3$ which denotes the volume fraction of the precipitates.[8]

For instance, for the mean e^+ lifetime, the last summand in Eq. (51), i.e., the rate-equation solution, has to be replaced by that calculated for diffusion- and reaction-limited trapping at

---

[5]A further model extension avoiding this constraint will be outlined below.

[6]Note that I_p characterizes the free state in the precipitate.

[7]The identical equation for I_t [Eq. (53)] follows from the root $p = -\tau_t^{-1}$ of the Laplace transform $\tilde{n}(p)$ in which the above-mentioned extensions of Eq. (23) are taken into consideration.

[8]Given the above initial condition $\rho_t(0) = \rho_p(0)$ and $\rho_t(0) = 0$.

GBs [7,11], yielding

$$\overline{\tau} = \tau_f \left\{ \left[1 - \left(\frac{r_0}{R} \right)^3 \right] + \frac{3\alpha r_0^2}{R^3}(\tau_t - \tau_f) \frac{\gamma_0 \hat{R} - \tanh(\gamma_0 \hat{R})\left[1 - \gamma_0^2 r_0 R \right]}{\gamma_0 \hat{R} - \tanh(\gamma_0 \hat{R})\left[1 - \gamma_0^2 r_0 R \right] + \frac{\alpha r_0}{D}\left[\gamma_0 R - \tanh(\gamma_0 \hat{R}) \right]} \right\}$$
$$+ \left(\frac{r_0}{R} \right)^3 \left\{ \tau_p + (\tau_t - \tau_p) \frac{3\beta L(\gamma_0' r_0)}{r_0 \gamma_0'(\beta + \gamma_0' D L(\gamma_0' r_0))} \right\}, \tag{54}$$

with $\gamma_0' = (\tau_p D)^{-1/2}$, $\gamma_0 = (\tau_f D)^{-1/2}$ and the Langevin function

$$L(z) = \coth z - \frac{1}{z}. \tag{55}$$

Likewise, the intensity component I_t^{precip} of the rate-equation solution in Eq. (53) has to be replaced by [7,11]

$$I_t^{\text{precip}} = \left(\frac{r_0}{R} \right)^3 \frac{3\beta}{r_0(\tau_p^{-1} - \tau_t^{-1})} \left\{ \frac{\gamma_t' D L(\gamma_t' r_0)}{\beta + \gamma_t' D L(\gamma_t' r_0)} \right\} \tag{56}$$

with

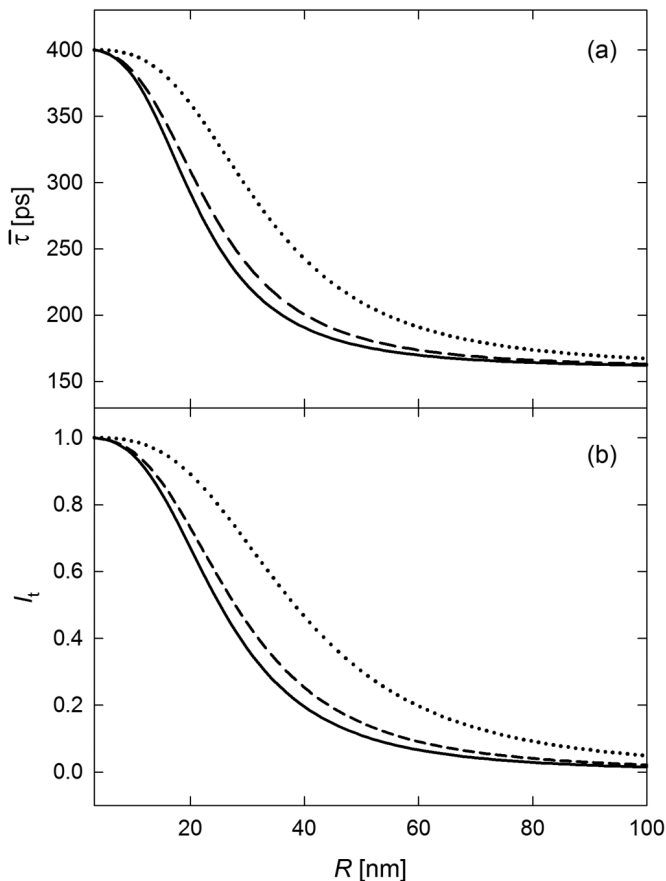$$\gamma_t'^2 = \frac{\tau_p^{-1} - \tau_t^{-1}}{D}. \tag{57}$$

FIG. 2. (a) Mean e^+ lifetime $\overline{\tau}$ and (b) relative intensity I_t of void component τ_t in dependence of diffusion radius R for diffusion-reaction model (solid line) [Eqs. (30) and (31)], for standard rate (dashed line) [Eqs. (38) and (39)], and for limiting case of entirely diffusion-limited trapping (dotted line) [Eqs. (41) and (42)]. Parameters: $\tau_f = 160$ ps, $\tau_t = 400$ ps, $D = 2 \times 10^{-5}$ m^{2}s^{-1}, $\alpha = 3 \times 10^3$ ms^{-1}, $r_0 = 3$ nm. Note that R is related to the void concentration [Eq. (7)].

For the sake of completeness, we quote the mean e^+ lifetime for reaction-controlled trapping from both inside and outside:

$$\overline{\tau} = \tau_t \left(1 - \left[\frac{r_0}{R} \right]^3 \right) \frac{\tau_t^{-1} + \frac{3\alpha r_0^2}{R^3 - r_0^3}}{\tau_f^{-1} + \frac{3\alpha r_0^2}{R^3 - r_0^3}} + \tau_t \left(\frac{r_0}{R} \right)^3 \frac{\tau_t^{-1} + \frac{3\beta}{r_0}}{\tau_p^{-1} + \frac{3\beta}{r_0}}. \tag{58}$$

A further extension for taking into account additional e^+ trapping at point defects inside the matrix (Sec. III D) and inside the precipitates (in analogy to the GB model [11]) is straightforward, so that the corresponding equations have not to be stated explicitly.

IV. DISCUSSION

A. Voids, clusters, small precipitates

The presented model with the exact solution of diffusion-reaction controlled trapping at voids (or other extended spherical defects like clusters and small precipitates) and competitive transition-limited trapping at vacancy-type defects yields closed-form expressions for the mean positron lifetime $\overline{\tau}$ [Eq. (43)] and for the relative intensities I_t [Eq. (45)] and I_v [Eq. (46)] of the e^+ lifetime components τ_t and τ_v of the void and the vacancy trapped states, respectively.

We start the discussion considering exclusively diffusion-reaction-controlled trapping at voids (Sec. III A). The model contains as limiting cases both the solution of the simple trapping model (Sec. III B) and the one of the entirely diffusion-limited trapping (Sec. III C). The mean e^+ lifetime $\overline{\tau}$ [Eq. (30)] and the intensity I_t [Eq. (31)] in dependence of the radius R of the diffusion sphere are compared in Fig. 2 with the two limiting cases. Note that R is related to the the void concentration [Eq. (7)]. For illustration, the following characteristic e^+ annihilation parameters are used: a free e^+ lifetime $\tau_f = 160$ ps as typical for aluminium, an e^+ lifetime $\tau_t = 400$ ps as typical for voids [15], an e^+ diffusion coefficient $D = 2 \times 10^{-5}$ m^{2}s^{-1}, a void radius $r = 3$ nm, and a specific e^+ trapping rate $\alpha = 3 \times 10^3$ ms^{-1} reported by Dupasquier *et al.* [6] for interfaces in Al. For surfaces of Al, a value $\alpha = 7.6 \times 10^3$ ms^{-1} was calculated by Nieminen and Lakkonen [13]. Using an atomic volume Ω for Al of $\Omega^{-1} = 6 \times 10^{28}$ m^{-3}, $\alpha = 3 \times 10^3$ ms^{-1} corresponds to a trapping rate $\sigma_t = 2 \times 10^{16}$ s^{-1} [Eq. (1)] which is similar to that deduced by Bentzon and Evans [14] for voids in Mo.[9]

---

[9]A value $\sigma_t = 4 \times 10^{16}$ s^{-1} is deduced from the trapping rate of 3.2×10^9 s^{-1} at 300 K and a void number density of 5.3×10^{21} m^{-3} quoted in [14].
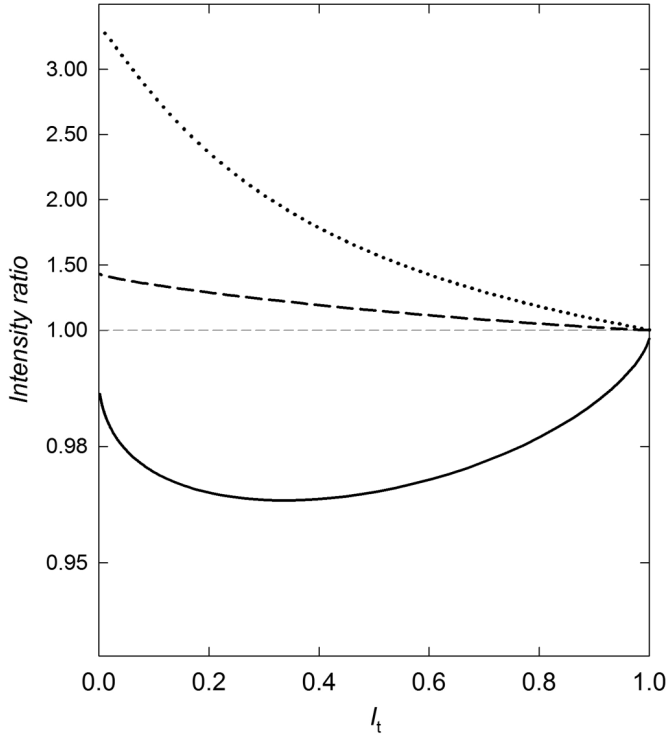
FIG. 3. Ratio of approximate intensity and exact intensity of void component τ_t in dependence of the exact intensity I_t according to Eq. (31). Approximate intensity: entirely diffusion-limited trapping (dotted line) [Eq. (42)], entirely reaction-controlled trapping (dashed line) [Eq. (39)], and simple trapping model [Eq. (39)] with effective diffusion trapping rate K_{eff} [Eq. (60)] (solid line). Note the different scales of the ratio axis for ratios <1 and >1. Parameters: $\Omega^{-1} = 6 \times 10^{28}$ m^{-3}, others as in Fig. 2.

Both $\overline{\tau}$ [Fig. 2(a)] and I_t [Fig. 2(b)] exhibit the characteristic sigmoidal increase from the free state to the saturation-trapped state with decreasing R, i.e., increasing void concentration C_t. Compared to the exact solution of the present model, the standard trapping model and the limiting case of entirely diffusion-limited trapping show qualitatively the same trend for $\overline{\tau}$ and I_t. However, both special cases systematically overestimate $\overline{\tau}$ and I_t, i.e., predict stronger trapping since either the rate-limiting effect or the diffusion-limiting effect are neglected in these approximations. For instance, if one would determine the void concentration from a typical, experimentally measured intensity I_t of 45% [21], a concentration 36% too low would be deduced from the standard trapping model compared to the exact theory for the parameter set according to Fig. 2(b).

The deviations of the two limiting cases from the exact solution become even more clear when the ratios of the trap component intensities of the limiting and exact solution is considered as shown in the upper part of Fig. 3. The deviation from the exact solution substantially increases with decreasing intensity, i.e., with decreasing void concentration. In this low-concentration regime, the deviations attain a factor of about 1.5 (reaction limit) or larger than 3 (diffusion limit) for the present set of parameters, i.e., the entirely diffusion-limiting case deviates in this example more strongly than the reaction-limited case. Diffusion limitation gets even more pronounced when e^+ diffusivity is reduced, e.g., due to scattering at lattice
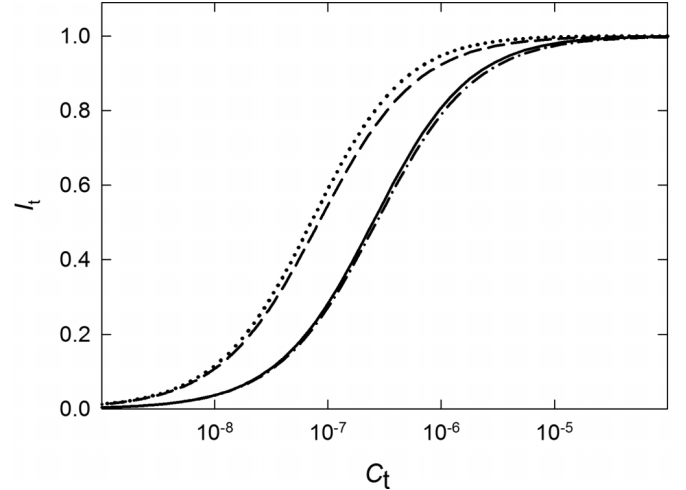

FIG. 4. Relative intensity I_t of void component τ_t in dependence of voids concentration C_t for diffusion-reaction model (solid line) [Eq. (31)], for limiting case of entirely diffusion-limited trapping (dotted line) [Eq. (42)], as well as for simple trapping model [Eq. (39)] with effective trapping rate of diffusion K_{diff} [Eq. (59)] (dashed line) or with effective diffusion- and transition-limited trapping rate K_{eff} [Eq. (60)] (dashed-dotted line). Parameters: $\Omega^{-1} = 6 \times 10^{28}$ m^{-3}, others as in Fig. 2.

imperfections. Regarding the opposite side of high-defect concentrations, Fig. 3 (upper part) nicely demonstrates that deviations from the exact theory vanish upon approaching e^+ saturation trapping since in this regime kinetic effects tends to become irrelevant.

1. Comparison with effective rate approach

Next, we compare the present model with approximations according to which diffusion limitation is taking account in the standard trapping model by means of a diffusion-limited trapping rate [14,22]:

$$K_{\mathrm{diff}} = \frac{4\pi r_0 D}{\Omega} C_t. \tag{59}$$

The case of both transition- and diffusion-limited trapping is treated in this approximation by means of the effective trapping rate [14,22]

$$K_{\mathrm{eff}} = \frac{K_{\mathrm{diff}} \sigma_t C_t}{K_{\mathrm{diff}} + \sigma_t C_t} \tag{60}$$

with σ_t and C_t according to Eqs. (1) and (7), respectively. We note that the diffusion-limited trapping rate according to Eq. (59) is also included in the present model; in fact, K_{diff} is identical to the prefactor of I_t for entirely diffusion-limited trapping [Eq. (42)] when the subtrahend r_0^3 in the nominator, which is associated with the defect volume, is omitted.

In Fig. 4 the concentration dependence of the relative intensity I_t of the e^+ lifetime component τ_t in voids is shown for the exact models of diffusion reaction [Eq. (31)] or entire diffusion limitation [Eq. (42)] in comparison with the corresponding approximations using the above-mentioned effective or diffusion trapping rates [Eqs. (59) and (60)] with the simple trapping model [Eq. (39)]. Although the effective-rate approximations of the diffusion limitation describe the

sigmoidal curve fairly well, deviations from the exact diffusion models are also apparent, e.g., for the example, $I_t = 45\%$, mentioned above the deviation in concentration is about 7 % compared to the exact diffusion-reaction theory.

The deviations become clearer once more when we consider the intensity ratio of the effective-rate model and the exact theory, as plotted in the lower part of Fig. 3. Remarkably, since the effective trapping rate K_{eff} is lower than both the reaction trapping rate $\sigma_t C_t$ and the diffusion trapping rate K_{diff}, the intensity I_t deduced from the effective trapping model is smaller than the exact value. Deviations from the full model occur throughout the entire intensity regime, although these deviations are less pronounced compared to the two limiting cases (fully reaction or diffusion limited, upper part of Fig. 3). For applications in the analysis of experimental data, the accuracy of the effective-rate approach [Eq. (60)] can be assessed by plotting the intensity ratio (lower part of Fig. 3) for the respective parameter set. Irrespectively whether deviations of the effective-rate approach are strong or minor only, the present model founded on diffusion-reaction theory is that which covers the underlying physics most accurately.

2. Competitive trapping at point defects

Now, we discuss the general case that in addition to diffusion-reaction-controlled trapping at voids, also competitive transition-limited trapping at vacancy-type defects in the lattice occurs (Sec. III D). The relative intensities of the void component I_t [Eq. (45)] and of the vacancy component I_v [Eq. (46)] are plotted in Fig. 5 in dependence of void concentration C_t (a) and vacancy concentration C_v (b), for a given fixed C_v or C_t, respectively. For the vacancy-type defect, an e^+ lifetime component $\tau_v = 250$ ps and a specific trapping rate $\sigma_v = 4 \times 10^{14}$ s^{-1} [23] are assumed; the other parameters are the same as used above. The competitive e^+ trapping at voids and vacancy-type defects becomes evident. For a given vacancy concentration, the intensity I_t of the void increases and the intensity I_v of the vacancy component decreases with increasing void concentration due to the increasing fraction of e^+ that reaches the voids [Fig. 5(a)]. Likewise, for a given void concentration, I_v increases and I_t decreases with increasing vacancy concentration [Fig. 5(b)].

3. Comparison with e^+ trapping at grain boundaries

In the end of this section (Sec. IV A), the results of the present model on diffusion-reaction-limited e^+ trapping at extended spherical defects will briefly be compared with the corresponding model of e^+ trapping at grain boundaries of spherical crystallites with radius R [7,11]. Whereas in the latter case the surface of the diffusion sphere with area $4\pi R^2$ acts as e^+ trap, in the present case with voids of radius r_0, the trapping active area $4\pi r_0^2$ is much smaller. Moreover, the trapping rate $3\alpha/R$ for grain boundary trapping [11] decreases much more slowly with increasing R compared to the trapping rate $3\alpha r_0^2/(R^3 - r_0^3)$ of spherical extended defects with radius r_0 [Eq. (24)]. This is the reason why diffusion limitation affects the kinetics of e^+ trapping at grain boundaries more strongly than in the case of voids, which is nicely demonstrated in Fig. 6 where the exact solutions are compared with those of infinite diffusivities. In Fig. 6 the mean e^+ lifetime according to the
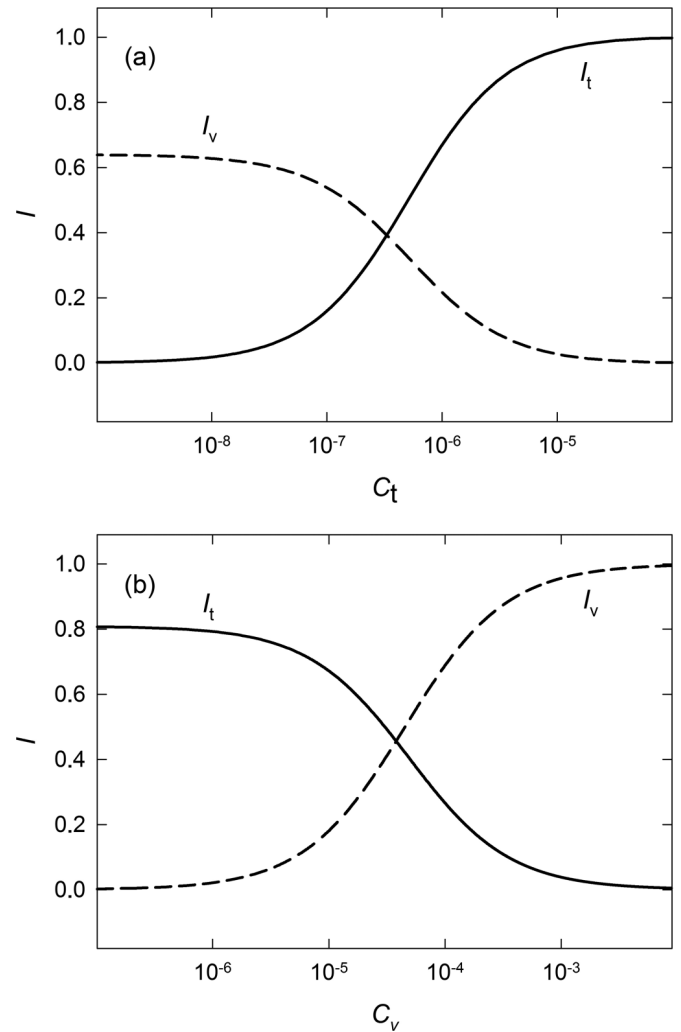

FIG. 5. Relative intensities I_t (solid line) [Eq. (45)] of void component τ_t and I_v (dashed line) [Eq. (46)] of vacancy component τ_v in dependence of (a) void concentration C_t and (b) vacancy concentration C_v. Parameters: $\tau_v = 250$ ps, $\sigma_v = 4 \times 10^{14}$ s^{-1}. $\Omega^{-1} = 6 \times 10^{28}$ m^{-3}, others as in Fig. 2. (a) $C_v = 10^{-5}$, (b) $C_t = 10^{-6}$.

exact solutions and those of the standard rate theory for the two types of extended traps are plotted. The exact solution for e^+ trapping at grain boundaries of spherical crystallites with radius R reads as [7,11]

$$\bar{\tau} = \tau_f + (\tau_t - \tau_f)\frac{3\alpha L(\gamma_0 R)}{R\gamma_0\{\alpha + \gamma_0 DL(\gamma_0 R)\}} \text{ with}$$

$$L(z) = \coth z - \frac{1}{z}. \tag{61}$$

The more stronger deviation between the exact solution and the rate theory in the case of grain boundary trapping is obvious (Fig. 6).

B. Larger precipitates: e^+ trapping from both sides of precipitate-matrix interface

In Sec. (III E) we extended the model for applying it to larger precipitates taking into account free e^+ annihilation within the precipitate. The e^+ trapping from the precipitate
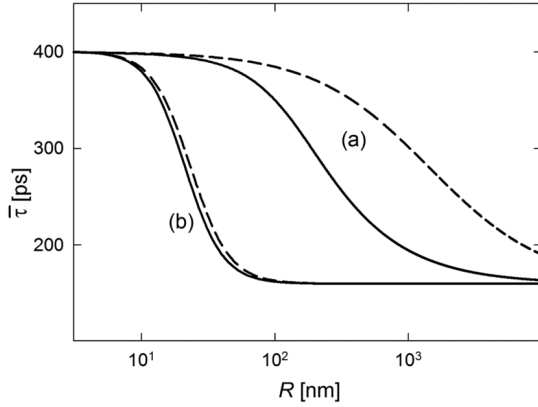
FIG. 6. Comparison of mean e^+ lifetime $\overline{\tau}$ for diffusion-reaction-limited e^+ trapping (a) at grain boundaries of spherical crystallites with radius R [7,11] and (b) at extended spherical defects (this work, Fig. 2). (a) Exact solution according to Eq. (61) [7] (solid line) and solution for standard rate theory (dashed line) [Eq. (38)] with trapping rate $K = 3\alpha/R$; (b) exact solution [Eq. (30)] (solid line) and solution for standard rate theory (dashed line) [Eq. (38)] with trapping rate $3\alpha r_0^2/(R^3 - r_0^3)$ [Eq. (24)]. Parameters as in Fig. 2.
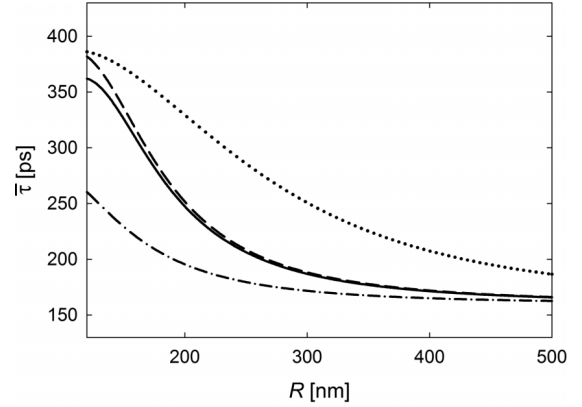

FIG. 7. Mean e^+ lifetime in dependence of radius R (i) for diffusion- and reaction-limited e^+ trapping into the precipitate-matrix interface from both the matrix and the precipitate (solid line) [Eq. (54)], (ii) for diffusion- and reaction-limited e^+ trapping from the matrix and entirely reaction-controlled trapping from the precipitate (dashed line) [Eq. (51)], (iii) for entirely reaction-controlled trapping from both the matrix and the precipitate (dotted line) [Eq. (58)], and (iv) for rate model as for (iii), but with effective diffusion-limited trapping rate [Eq. (60)] (dashed-dotted line). Precipitate radius $r_0 = 100$ nm. Other parameters: $\tau_f = \tau_c = 160$ ps, $\tau_t = 400$ ps, $D = 2 \times 10^{-5}$ m^{2}s^{-1}, $\alpha = \beta = 3 \times 10^3$ ms^{-1}. Note that R is related to the precipitate concentration [Eq. (7)].

into the precipitate-matrix interface is handled either by rate theory, for special cases where the precipitate radius is well below the e^+ diffusion length, or else by diffusion-reaction theory, for the more general case that the precipitate radius is in the range of or larger than the e^+ diffusion length. With this extension, the present model is applicable to a wide variety of structurally complex scenarios, namely, to all types of composite structures where spherical precipitates are embedded in a matrix irrespective of the size and the number density of the precipitates.

Whereas for extended defects with smaller size, which were discussed in Sec. IV A, the deviations between the exact model and the rate theory may be of less relevance since the trapping active area $4\pi r_0^2$ is small, for larger precipitates the diffusion-limitation in any case gets relevant owing to the much larger trapping active area, similar as for e^+ trapping at GBs (see Fig. 6). This is demonstrated in Fig. 7, where the variation of the mean e^+ lifetime with radius R is compared for four different solutions, namely, diffusion limitation of trapping into the precipitate-matrix interface from both the matrix and the precipitate, from the matrix only, and for entirely reaction-limited trapping from both sides with standard-trapping rate or with effective diffusion-limited trapping rate. The latter is obtained by replacing in Eq. (58) the standard-trapping rates by the effective diffusion-limited trapping rate according to Eq. (60), i.e., $3\alpha r_0^2 (R^3 - r_0^3)^{-1}$ by $3\alpha D r_0^2 R^{-3}(\alpha r_0 + D)^{-1}$ and $3\beta r_0^{-1}$ by $3\beta D r_0^{-1}(\beta r_0 + D)^{-1}$.

In contrast to the case of small extended defects (Fig. 6), for larger precipitates (example $r_0 = 100$ nm) substantial deviations between the solutions occur for the entire concentration regime if the diffusion limitation is neglected (Fig. 7). Even the rate approach with effective diffusion-limited trapping rate, which at least for small extended defects is a reasonable approximation (Sec. IV A 1, Fig. 4), turns out to be completely inadequate for the larger precipitate size. The deviations are much less if the diffusion limitation is only neglected for

the trapping from the precipitate into the interface since the precipitate size (in contrast to the precipitate distance) remains in the range of the e^+ diffusion length independent of the precipitate concentration. Anyhow, for a precise description even for such small precipitate sizes, the exact theory of diffusion- and reaction-controlled trapping has to be applied for the trapping from the interior of the precipitates.

Finally, we compare this model with that presented by Dryzek [9,24] for studying recrystallization in highly deformed metals. In that case, recrystallized grains are embedded in a highly deformed matrix. Diffusion-limited e^+ trapping occurs from the grains into the matrix, whereas within the matrix saturation trapping of e^+ prevails due to the high-defect density. In this sense, the model of Dryzek represents an extension of the diffusion-reaction theory for trapping at grain boundaries, where instead of GBs a surrounding deformed matrix is considered. The model presented here represents a further extension where diffusion- and reaction-controlled trapping also from the matrix into the interfaces is considered.

V. CONCLUSION

The present model with the exact solution of the diffusion-reaction theory for the e^+ trapping at extended spherical defects and competitive transition-limited trapping at atomic defects yields a basis for the quantitative description of the e^+ behavior in materials with complex defect structure. It could be shown that the model includes as special cases the simple trapping model and the entirely diffusion-limited trapping, but both of these limiting cases represent approximations only. For the full model, closed-form expressions were obtained for the mean positron lifetime $\overline{\tau}$ and for the intensities of the e^+ lifetime components associated with trapping. This

exact model allowed a quantitative assessment of the usual approach, which takes diffusion limitation for the trapping at voids into account by effective diffusion trapping rates. The present closed-form solutions also renders this effective-rate approach unnecessary.

The presented theory goes even much further beyond existing models since it is not only applicable to small extended defects (such as voids or clusters), but also to larger precipitates where positron trapping from the precipitates into the precipitate-matrix interface is taken into consideration. Therefore, the model presents the basis for studying all types of composite structures where spherical precipitates are embedded in a matrix irrespective of their size and their number density.

ACKNOWLEDGMENTS

[1] P. Hautojärvi, *Positrons in Solids* (Springer, Berlin, 1979).

[2] D. Keeble, U. Brossmann, W. Puff, and R. Würschum, in *Characterization of Materials*, edited by E. Kaufmann (Wiley, Hoboken, NJ, 2012), p. 1899.

[3] R. Krause-Rehberg and H. Leipner, *Positron Annihilation in Semiconductors* (Springer, Berlin, 1999).

[4] M. J. Puska and R. M. Nieminen, Rev. Mod. Phys. **66**, 841 (1994).

[5] W. Brandt and R. Paulin, Phys. Rev. B **5**, 2430 (1972).

[6] A. Dupasquier, R. Romero, and A. Somoza, Phys. Rev. B **48**, 9235 (1993).

[7] R. Würschum and A. Seeger, Philos. Mag. A **73**, 1489 (1996).

[8] G. Kögel, Appl. Phys. A **63**, 227 (1996).

[9] J. Dryzek, Acta Phys. Pol. A **95**, 539 (1999).

[10] J. Čížek, I. Procházka, M. Cieslar, R. Kuzžel, J. Kuriplach, F. Chmelík, I. Stulíková, F. Bečvář, O. Melikhova, and R. K. Islamgaliev, Phys. Rev. B **65**, 094106 (2002).

[11] B. Oberdorfer and R. Würschum, Phys. Rev. B **79**, 184103 (2009).

[12] J. Dryzek, A. Czapla, and E. Kusior, J. Phys.: Condens. Matter **10**, 10827 (1998).

[13] R. Nieminen and J. Laakkonen, Appl. Phys. **20**, 181 (1979).

[14] M. Bentzon and J. Evans, J. Phys.: Condens. Matter **2**, 10165 (1990).

[15] M. Eldrup and B. Singh, J. Nucl. Mater. **323**, 346 (2003).

[16] J. Dryzek, Phys. Status Solidi B **209**, 3 (1998).

[17] R. M. Nieminen, J. Laakkonen, P. Hautojärvi, and A. Vehanen, Phys. Rev. B **19**, 1397 (1979).

[18] R. Würschum and A. Seeger, Z. Phys. Chem. **192**, 47 (1995).

[19] F. W. Olver, *NIST Handbook of Mathematical Functions* (Cambridge University Press, Cambridge, 2010).

[20] J. Dryzek, Phys. Status Solidi B **229**, 1163 (2002).

[21] P. Nambissan, P. Sen, and B. Viswanathan, in *Positron Annihilation*, edited by L. Dorikens-Vanpraet, M. Dorikens, and D. Segers (World Scientific, Singapore, 1989), p. 434.

[22] W. Frank and A. Seeger, Appl. Phys. **3**, 61 (1974).

[23] H.-E. Schaefer, Phys. Status Solidi A **102**, 47 (1987).

[24] J. Dryzek, M. Wrobel, and E. Dryzek, Phys. Status Solidi B **253**, 2031 (2016).

4.3.2   Article 6: Positron trapping and annihilation at interfaces between matrix and cylindrical or spherical precipitates

The article *Positron trapping and annihilation at interfaces between matrix and cylindrical or spherical precipitates modeled by diffusion-reaction theory* was published in the Conference Proceedings of the 18th International Conference on Positron Annihilation **2182**, 050010 in December 2019 [12].

This work was done by Roland Würschum as first author and Laura Resch as second author. The exact analytical solution of a diffusion-reaction model for the trapping and annihilation of positrons at interfaces between matrix and cylindrical or spherical precipitates was calculated by Roland Würschum. Laura Resch and Gregor Klinser did parts of the recalculation and cross-checking of the model and validated the model. Laura Resch calculated solutions for various parameter sets and gave the graphical representations.

In this paper the authors present an exact solution of the diffusion-reaction model for the trapping and annihilation of positrons at interfaces between matrix and cylindrical or spherical precipitates and give closed-form expressions for the mean positron lifetime and for the intensity of the annihilation component associated with the trapped state. The results presented in this paper extend our previous study (see article 5 in section 4.3.1, ref. [11]) by treating the composite structure not only for spherical- but also for cylindrical-shaped precipitates. Furthermore, the model includes, as a special case, the trapping and annihilation of positrons at extended open-volume defects like spherical voids or hollow cylinders.

Positron trapping and annihilation at interfaces between matrix and cylindrical or spherical precipitates modeled by diffusion-reaction theory

Roland Würschum[1,a)], Laura Resch[1] and Gregor Klinser[1]

[1]*Institute of Materials Physics, Graz University of Technology, Petersgasse 16, A-8010 Graz, Austria*

[a)]Corresponding author: wuerschum@tugraz.at

Dedicated to Professor Alfred Seeger

Abstract. The exact solution of a diffusion−reaction model for the trapping and annihilation of positrons at interfaces of precipitate−matrix composites is presented considering both cylindrical or spherical precipitates. Diffusion-limitation is taken into account for interfacial trapping from the surrounding matrix as well as from the interior of the precipitate. Closed-form expressions are obtained for the mean positron lifetime and for the intensity of the positron lifetime component associated with the interface-trapped state. The model contains as special case also positron trapping at extended open-volume defects like spherical voids or hollow cylinders. This makes the model applicable to all types of cylindrical- and spherical-shaped extended defects irrespective of their size and their number density.

Introduction

Positron (e^+) annihilation techniques are nowadays widely applied to study structurally complex materials. Here, a composite structure consisting of a crystalline matrix with embedded precipitates is of particular application relevance. It is, however, well known that e^+ trapping at such extended defects like precipitates cannot be correctly described by standard rate theory but demands for analysis in the framework of diffusion-reaction theory. Whereas diffusion-limited e^+ trapping at grain boundaries of crystallites (or equivalently at surfaces of particles) has been quantatively modeled by several groups [1, 2, 3, 4, 5], diffusion-limited e^+ trapping at interfaces of precipitate−matrix composites is more complex and has not been treated until recently [6]. In addition to diffusion-limited interface trapping from the interior of the precipitate, in particular the interfacial trapping from the surrounding matrix has to be treated taking into account diffusion limitation.

Following our earlier publications on grain boundaries [2, 5], in the present work the diffusion-reaction limited e^+ trapping at interfaces of precipitate−matrix composites is mathematically handled by means of Laplace transformation, which yields closed-form expressions for the mean e^+ lifetime and for the intensity of the annihilation component associated with the interfacial trapped state. These solutions can be conveniently applied for the analysis of experimental data. The present work treats the composite structure both for cylindrical- and for spherical-shaped precipitates. The solutions of the spherical-symmetric model were already reported recently in a broader context including modeling of voids and small clusters [6].

Cylindrical and spherical diffusion−reaction model

The geometry of the diffusion-reaction model is schematically shown in Fig. 1. The model describes positron (e^+) trapping and annihilation in a precipitate−matrix composite with either cylindrical- or spherical-shaped precipitates of radius r_0. Positron annihilation from the free bulk state is considered both for the matrix and for the precipitate, each characterized by a specific free e^+ lifetime, denoted τ_f and τ_p, respectively. Positron trapping into the

precipitate−matrix interface is considered to be diffusion- and reaction-limited for both the trapping from the surrounding matrix and from the interior of the precipitate. Trapping from the matrix is characterized by the specific trapping rate α and the e^+ diffusion coefficient D and from the precipitate by the rate β and the same value of D. The number density N_p^{sphere} of spherical precipitates per unit volume or that of cylindrical precipitates (N_p^{cyl}) per unit area is related to the outer radius R of the surrounding matrix:

$$N_p^{sphere} = \left(\frac{3}{4\pi R^3}\right)^{1/3}, \qquad N_p^{cyl} = \left(\frac{1}{\pi R^2}\right)^{1/2}. \tag{1}$$

Since detrapping of e^+ from the interface is neglected, the two e^+ trapping processes into the precipitate−matrix interface from inside the precipitate and from the surrounding matrix are completely decoupled apart from the initial condition. Both processes can, therefore, be treated independently. This implies further that diffusion-reaction limited e^+ trapping from inside the precipitates into the interfaces can be treated completely analogous to the corresponding models of e^+ trapping at grain boundaries of spherical [2, 5] or cylindrical crystallites [3].

The temporal and spatial evolution of the density ρ_m of free e^+ in the matrix and of those in the precipitates (ρ_p) is governed each by the diffusion equation:

$$\frac{\partial \rho_{m/p}}{\partial t} = D\nabla^2 \rho_{m/p} - \frac{\rho_{m/p}}{\tau_{f/p}} \tag{2}$$

where τ_f and τ_p denote the above mentioned free e^+ lifetimes. The e^+ density ρ_t in the trapped state of the precipitate−matrix interface consists of two parts, i.e., the densities $\rho_t^{(m)}$ and $\rho_t^{(p)}$ due to trapping from the matrix and the precipitate, respectively. These densities obey the rate equations

$$\frac{d\rho_t^{(m/p)}}{dt} = \alpha/\beta\,\rho_{m/p}(r_0, t) - \frac{1}{\tau_t}\rho_t\,, \tag{3}$$

with the specific trapping rates α, β (unit ms^{-1}) defined above.

The continuity of the e$^+$ flux at the boundary between the matrix (m) and the interface or between the precipitate (p) and the interface is expressed by

$$D\nabla\rho_m\Big|_{r=r_0} - \alpha\rho_m(r_0, t) = 0, \quad D\nabla\rho_p\Big|_{r=r_0} + \beta\rho_p(r_0, t) = 0\,. \tag{4}$$

The outer boundary condition

$$\frac{\partial \rho_m}{\partial r}\Big|_{r=R} = 0 \tag{5}$$

reflects the vanishing e^+ flux through the outer border ($r = R$) of the diffusion sphere. As initial condition a homogeneous distribution of e^+ in the matrix and the precipitate ($\rho_m(0) = \rho_p(0)$) is assumed without e^+ in the trapped state ($\rho_t(0) = 0$) for $t = 0$.

In order to obtain closed-form solutions, the time dependence of the diffusion and rate equations (2, 3) is handled by means of Laplace transformation. As briefly outlined in the appendix, solving the r-dependent differential equation and subsequent volume integration, finally leads to the Laplace transform $\tilde{n}(p)$ of the total probability $n(t)$ that a e^+ implanted at $t = 0$ has not yet been annihilated at time t. $\tilde{n}(p)$ contains the entire information of the e^+ annihilation characteristics (see next section). For the cylindrical case, $\tilde{n}(p)$ reads:
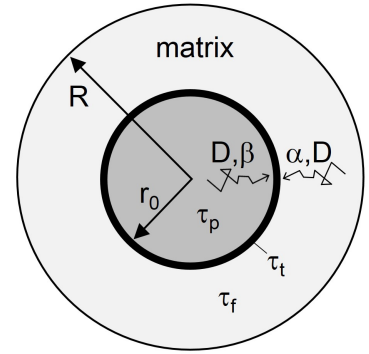
$$\tilde{n}(p) = \left(\frac{r_0}{R}\right)^2 \frac{1}{\tau_p^{-1} + p}\left\{1 + \frac{2\beta}{r_0}\frac{\tau_p^{-1} - \tau_t^{-1}}{\tau_t^{-1} + p}\frac{\Theta}{\gamma'(\Theta\gamma'D + \beta)}\right\} + \frac{1}{\tau_f^{-1} + p}\left\{1 - \left(\frac{r_0}{R}\right)^2 + \frac{2\alpha r_0}{R^2}\frac{\tau_f^{-1} - \tau_t^{-1}}{\tau_t^{-1} + p}\frac{\Lambda_1}{\gamma(\Lambda_1\gamma D - \alpha\Lambda_0)}\right\} \tag{6}$$

with

$$\Theta = \Theta(\gamma' r_0) = \frac{I_1(\gamma' r_0)}{I_0(\gamma' r_0)}, \qquad \Lambda_{0/1} = \Lambda_{0/1}(\gamma r_0, \gamma R) = I_{0/1}(\gamma r_0)K_1(\gamma R) + / - K_{0/1}(\gamma r_0)I_1(\gamma R)\,, \tag{7}$$

and

$$\gamma^2 = \frac{\tau_f^{-1} + p}{D}, \quad \gamma'^2 = \frac{\tau_p^{-1} + p}{D}\,. \tag{8}$$

FIGURE 1. Geometry of diffusion-reaction model.

050010-2

I_j, K_j ($j = 0, 1$) denote the modified Bessel functions [7]. The solution for the spherical case reads

$$\tilde{n}(p) = \left(\frac{r_0}{R}\right)^3 \frac{1}{\tau_p^{-1} + p}\left\{1 + \frac{3\beta}{r_0}\frac{\tau_p^{-1} - \tau_t^{-1}}{(\tau_t^{-1} + p)(\tau_p^{-1} + p)}\frac{\gamma' DL(\gamma' r_0)}{\gamma' DL(\gamma' r_0) + \beta}\right\} +$$

$$\frac{1}{\tau_f^{-1} + p}\left\{1 - \left(\frac{r_0}{R}\right)^3 + \frac{3\alpha r_0^2}{R^3}\frac{\tau_f^{-1} - \tau_t^{-1}}{(\tau_t^{-1} + p)(\tau_f^{-1} + p)}\frac{\gamma\hat{R} - \tanh(\gamma\hat{R})[1 - \gamma^2 r_0 R]}{\gamma\hat{R} - \tanh(\gamma\hat{R})[1 - \gamma^2 r_0 R] + \frac{\alpha r_0}{D}[\gamma R - \tanh(\gamma\hat{R})]}\right\} \qquad (9)$$

with $\hat{R} = R - r_0$ and the Langevin function $L(z) = \coth z - 1/z$.

Results for analysis of measurements

The mean positron lifetime $\bar{\tau}$ is obtained by taking the Laplace transform [Eq. (6) and (9)] at $p = 0$ ($\bar{\tau} = \tilde{n}(p = 0)$). For the precipitation−matrix composite with cylindrical symmetry the mean positron lifetime reads

$$\bar{\tau} = \left(\frac{r_0}{R}\right)^2 \tau_p\left\{1 + \frac{2\beta}{r_0}(\tau_t - \tau_p)\frac{\Theta}{(\tau_p/D)^{1/2}\beta + \Theta]}\right\} + \tau_f\left\{1 - \left(\frac{r_0}{R}\right)^2 + \frac{2\alpha r_0}{R^2}(\tau_t - \tau_f)\frac{\Lambda_1}{\Lambda_1 - (\tau_f/D)^{1/2}\alpha\Lambda_0}\right\} \qquad (10)$$

with $\Theta(\gamma_0' r_0)$ and $\Lambda_{0,1}(\gamma_0 r_0, \gamma_0 R)$ according to eq. (7) with $\gamma_0' = (\tau_p D)^{-1/2}$ and $\gamma_0 = (\tau_f D)^{-1/2}$. Likewise the solution of the spherical precipitates reads [6]

$$\bar{\tau} = \left(\frac{r_0}{R}\right)^3 \tau_p\left\{1 + \frac{2\beta}{r_0}(\tau_t - \tau_p)\frac{L(\gamma_0' r_0)}{(\tau_p/D)^{1/2}\beta + L(\gamma_0' r_0)}\right\} +$$

$$\tau_f\left\{1 - \left(\frac{r_0}{R}\right)^3 + \frac{3\alpha r_0^2}{R^3}(\tau_t - \tau_f)\frac{\gamma_0\hat{R} - \tanh(\gamma_0\hat{R})[1 - \gamma_0^2 r_0 R]}{\gamma_0\hat{R} - \tanh(\gamma_0\hat{R})[1 - \gamma_0^2 r_0 R] + \frac{\alpha r_0}{D}[\gamma_0 R - \tanh(\gamma_0\hat{R})]}\right\}. \qquad (11)$$

The positron lifetime spectrum follows from $\tilde{n}(p)$ [Eq. (6) and (9)] by means of Laplace inversion. The single poles $p = -\lambda_i$ of $\tilde{n}(p)$ in the complex p plane define the decay rates with the relative intensities I_i of the e^+ lifetime spectrum. As usual for this kind of problem, the annihilation from the free state in the matrix and the precipitates is characterized by series of fast decay rates $p = -\lambda_i(i = 0, 1, 2, \ldots)$ ($\lambda_i > \tau_{f/p}^{-1}$) which follow from the first-order roots of $n(p)$. The rates are given by the solutions of the transcendental equations which read for the precipitates with cylindrical or spherical symmetry

$$\gamma'^\star\frac{J_1(\gamma'^\star r_0)}{J_0(\gamma'^\star r_0)} = \frac{\beta}{D}, \quad \text{or} \quad \gamma'^\star r_0 \coth(\gamma'^\star r_0) = 1 - \frac{\beta r_0}{D} \qquad (12)$$

respectively, with $\gamma'^{\star 2} = (\lambda_i - \tau_p^{-1})/D$ and for the matrix in the cylinder- or sphere-symmetrical case

$$\gamma^\star\left\{Y_1(\gamma^\star r_0)J_1(\gamma^\star R) - J_1(\gamma^\star r_0)Y_1(\gamma^\star R)\right\} = -\frac{\alpha}{D}\left\{Y_0(\gamma^\star r_0)J_1(\gamma^\star R) - J_0(\gamma^\star r_0)Y_1(\gamma^\star R)\right\},$$

$$\text{or} \quad \tanh(\gamma^\star\hat{R}) = \frac{\gamma^\star(\alpha r_0 R + D\hat{R})}{D(1 + \gamma^{\star 2} r_0 R) + \alpha r_0} \qquad (13)$$

respectively, with $\gamma^{\star 2} = (\lambda_i - \tau_f^{-1})/D$ and the Bessel functions Y_j, J_j ($j = 0, 1$) [7].

For the pole $p = -\tau_t^{-1}$ characterizing the interface-trapped state, $\tilde{n}(p)$ directly yields the corresponding intensity I_t of this positron lifetime component. This intensity

$$I_t = I_t^{precip} + I_t^{matrix} \qquad (14)$$

is composed of the two parts which arise from e^+ trapping into the interface from the precipitate (I_t^{precip}) and from the matrix (I_t^{matrix}). For the cylindrical symmetry, $\tilde{n}(p)$ (eq. 6) yields for the pole $p = -\tau_t^{-1}$:

$$I_t^{matrix} = \frac{2\alpha r_0}{R^2}\frac{\Lambda_1}{(\tau_f^{-1} - \tau_t^{-1})\Lambda_1 - \gamma_t\alpha\Lambda_0}, \qquad (15)$$

$$I_t^{precip} = \left(\frac{r_0}{R}\right)^2 \frac{2\beta}{r_0} \frac{\Theta}{(\tau_p^{-1} - \tau_t^{-1})\Theta + \beta\gamma_t'} \tag{16}$$

with $\Theta = \Theta(\gamma_t' r_0)$ and $\Lambda_{0,1}(\gamma_t r_0, \gamma_t R)$ according to eq. (7) with

$$\gamma_t^2 = \frac{\tau_f^{-1} - \tau_t^{-1}}{D}, \quad \gamma_t'^2 = \frac{\tau_p^{-1} - \tau_t^{-1}}{D}. \tag{17}$$

The respective total intensities arising from free e^+ annihilation in the precipitate and in the matrix are given by the volume-weighted complementary values:

$$I_{bulk}^{precip} = \left(\frac{r_0}{R}\right)^2 (1 - I_t^{precip}), \quad I_{bulk}^{matrix} = \left[1 - \left(\frac{r_0}{R}\right)^2\right](1 - I_t^{matrix}). \tag{18}$$

The intensities for the spherical case read [6]

$$I_t^{matrix} = \frac{3\alpha r_0^2}{R^3} \frac{1}{\tau_f^{-1} - \tau_t^{-1}} \frac{\gamma_t \hat{R} - \tanh(\gamma_t \hat{R})[1 - \gamma_t^2 r_0 R]}{\gamma_t \hat{R} - \tanh(\gamma_t \hat{R})[1 - \gamma_t^2 r_0 R] + \frac{\alpha r_0}{D}[\gamma_t R - \tanh(\gamma_t \hat{R})]}, \tag{19}$$

$$I_t^{precip} = \left(\frac{r_0}{R}\right)^3 \frac{3\beta}{r_0} \frac{1}{\tau_p^{-1} - \tau_t^{-1}} \frac{\gamma_t' DL(\gamma_t' r_0)}{\beta + \gamma_t' DL(\gamma_t' r_0)}, \tag{20}$$

$$I_{bulk}^{precip} = \left(\frac{r_0}{R}\right)^3 (1 - I_t^{precip}), \quad I_{bulk}^{matrix} = \left[1 - \left(\frac{r_0}{R}\right)^3\right](1 - I_t^{matrix}). \tag{21}$$

As long as the precipitate diameter is remarkably lower than the e^+ diffusion length $[(D\tau_p)^{-1/2}]$ in the precipitate, diffusion limitation of e^+ trapping from the precipitate into the interface with the matrix can be neglected, so that this part of the e^+ trapping process can be reasonably well described by standard reaction theory. In this case, the first summand of the mean e^+ lifetime in eq. (10) and eq. (11) simplifies to

$$\left(\frac{r_0}{R}\right)^2 \tau_t \frac{\tau_t^{-1} + \frac{2\beta}{r_0}}{\tau_p^{-1} + \frac{2\beta}{r_0}}, \quad \text{or} \quad \left(\frac{r_0}{R}\right)^3 \tau_t \frac{\tau_t^{-1} + \frac{3\beta}{r_0}}{\tau_p^{-1} + \frac{3\beta}{r_0}}, \tag{22}$$

respectively. In the same manner, the intensity I_t^{precip} for the cylindrical [Eq. 16] and spherical case [Eq. 20] simply reads,

$$I_t^{precip} = \left(\frac{r_0}{R}\right)^2 \frac{2\beta}{r_0} \frac{1}{\tau_p^{-1} + \frac{2\beta}{r_0} - \tau_t^{-1}}, \quad \text{or} \quad I_t^{precip} = \left(\frac{r_0}{R}\right)^3 \frac{3\beta}{r_0} \frac{1}{\tau_p^{-1} + \frac{3\beta}{r_0} - \tau_t^{-1}}. \tag{23}$$

Discussion

The presented model with the exact solution of diffusion-reaction controlled trapping at interfaces of matrix−precipitate composites with cylindrical or spherical symmetry yields closed-form expressions for the mean positron lifetime $\bar{\tau}$ [Eq. (10), (11)] and for the relative intensity I_t [Eq. (14) with Eq. (15) and (16) or (19) and (20)] of the e^+ lifetime component τ_t of the interface-trapped state. Both $\bar{\tau}$ and I_t consist of volume-weighted parts associated with the precipitates (weighting factor: $(r_0/R)^i$, $i = 2, 3$) and the matrix (weighting factor: $[1 - (r_0/R)^i]$).[1] Apart from the weighting factor $[(r_0/R)^3]$, the precipitate part of $\bar{\tau}$ for the spherical case [Eq. (11)] is identical to that deduced earlier for e^+ trapping at grain boundaries of spherical crystallites [2]. Likewise, the precipitate parts of I_t (without $(r_0/R)^i$, $i = 2, 3$) [Eq. (16) and (20)] are identical to those obtained for e^+ trapping at grain boundaries of cylindrical [3] or spherical crystallites [2, 3].

---

[1]For instance for the cylindrical case the extraction of the weighting factor out of the bracket of the matrix term of $\bar{\tau}$ [Eq. 10] yields: $\tau_f[1 - (r_0/R)^2][1 + 2\alpha r_0/(R^2 - r_0^2)(\ldots)]$. Analogous for the matrix part of $\bar{\tau}$ in the spherical case [Eq. 11]: $\tau_f[1 - (r_0/R)^3][1 + 3\alpha r_0^2/(R^3 - r_0^3)(\ldots)]$. Likewise for the intensities of the matrix part [Eq. (15) and (19)] extraction of the weighting factor yields: $[1 - (r_0/R)^2]2\alpha r_0/(R^2 - r_0^2)$ instead of $2\alpha r_0/R^2$ [Eq. (15)]; $[1 - (r_0/R)^3]3\alpha r_0^2/(R^3 - r_0^3)$ instead of $3\alpha r_0^2/R^3$ [Eq. (19)].
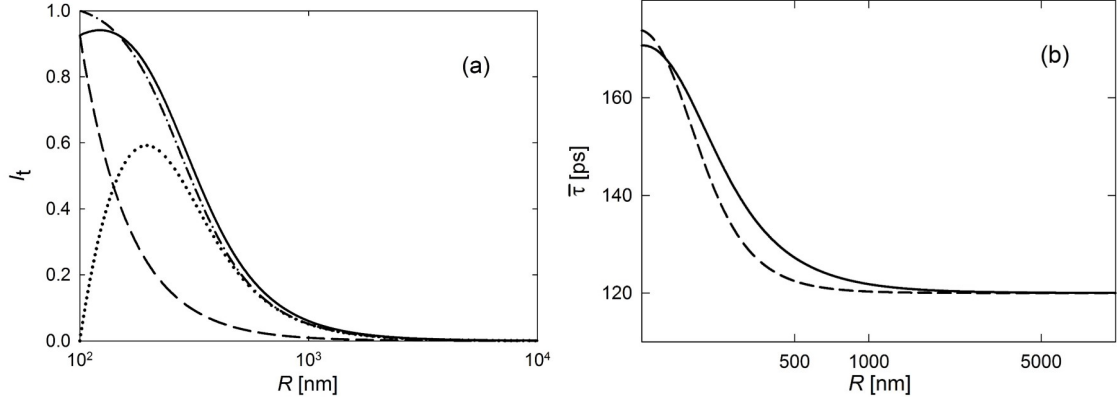
FIGURE 2. (a) Relative intensity I_t [Eq. (14), solid line] of interface-trapped component τ_t in dependence of diffusion radius R for cylindrical-shaped precipitates. The dashed and dotted line shows the part which arises from e^+ trapping from the precipitate [I_t^{precip}, Eq. (16)] and from the matrix [I_t^{matrix}, Eq. (15)], respectively. The dash-dotted line shows I_t^{matrix} [Eq. (15)] without the weighting factor [$1 - (r_0/R)^2$] [Eq. (25)]. (b) Mean e^+ lifetime $\bar{\tau}$ in dependence of diffusion radius R for precipitate−matrix composite with cylindrical [Eq. (10), solid line] or spherical symmetry [Eq. (11), dashed line]. Parameters: $\tau_f = \tau_p = 120$ ps, $\tau_t = 180$ ps, $D = 10^{-4}$ m^{2}s^{-1}, $\alpha = \beta = 3 \times 10^3$ ms^{-1}, $r_0 = 100$ nm. Note that R is related to number density of precipitates [Eq. 1].

Fig. 2.a shows the intensity I_t [Eq. (14)] in dependence of diffusion radius R for cylindrical-shaped precipitates of constant diameter r_0. With decreasing R, i.e., with increasing number of precipitates [Eq. 1], the characteristic sigmoidal-shaped increase of I_t occurs. Also plotted in Fig. 2.a are the two parts of I_t arising from the precipitate and matrix, i.e., I_t^{precip} [Eq. (16)] and I_t^{matrix} [Eq. (15)], respectively. Due to the constant precipitate size, the increase of I_t^{precip} with decreasing R exclusively reflects the variation of the weighting factor $(r_0/R)^2$. Remarkably, I_t^{matrix} shows a maximum. The increase of I_t^{matrix} with decreasing R arises from the increasing trapping due to a decrease of the maximum e^+ diffusion length necessary for e^+ for reaching the interface. For small values of R this I_t^{matrix} increase with decreasing R due to the diffusion effect is counterbalanced by the effect of the weighting factor, i.e., the decreasing relative initial fraction of e^+ in the matrix compared to that in precipitates. This is illustrated by the plot of I_t^{matrix} without the weighting factor (see Fig. 2.a) which shows the expected sigmoidal-shaped increase over the entire R regime.[2]

A comparison of cylindrical and spherical symmetry is shown in Fig. 2.b by the example of the mean positron lifetime $\bar{\tau}$. Similar to I_t, $\bar{\tau}$ exhibits the characteristic sigmoidal-shaped increase with decreasing R, i.e., increasing precipitates concentration. Over nearly the entire R-regime, the $\bar{\tau}$-increase for cylindrical precipitates is higher than for spherical ones, which means that for a given R the trapping rate at interfaces of cylindrical precipitates exceeds that of spherical precipitates. This is simply because the trapping active area for cylinders is larger than for spheres for a given R.

Finally one should mention that the model can also be applied to extended open-volume defects like spherical voids or hollow cylinders. In that case e^+ trapping occurs exclusively from the matrix outside the internal surface of the defect (rather than at the matrix−precipitate interface from both sides). The solutions for the mean positron lifetime $\bar{\tau}$ and the trap intensity I_t directly follows from the equations given above by omitting the part arising from the precipitate. Assuming as initial condition that for $t = 0$ no positrons are inside the trap, the matrix weighting factor $[1 - (r_0/R)^i](i = 2, 3)$ has to be replaced by 1. For the hollow cylinders the solutions read:[3] [cf. Eq. (10), eq. (15), and first footnote on previous page.]

$$\bar{\tau} = \tau_f \left\{ 1 + \frac{2\alpha r_0}{R^2 - r_0^2} (\tau_t - \tau_f) \frac{\Lambda_1}{\Lambda_1 - (\tau_f/D)^{1/2}\alpha\Lambda_0} \right\} \text{ with } \Lambda_{0,1} = \Lambda_{0,1}(\gamma_0 r_0, \gamma_0 R), \quad (24)$$

$$I_t = \frac{2\alpha r_0}{R^2 - r_0^2} \frac{\Lambda_1}{(\tau_f^{-1} - \tau_t^{-1})\Lambda_1 - \gamma_t \alpha \Lambda_0} \text{ with } \Lambda_{0,1} = \Lambda_{0,1}(\gamma_t r_0, \gamma_t R). \quad (25)$$

---

[2]I_t^{matrix} without the weighting factor corresponds to eq. (25); see below.

[3]The solutions for voids were reported recently.[6]

In conclusion, the model presents the basis for studying all types of cylindrical- and spherical-shaped extended defects irrespective of their size and their number density. Of particular relevance are matrix−precipitate composites for which such a model could be established in the present work. An intriguing feature of the model are the closed-form solutions which can be conveniently applied for the analysis of experimental data.

Appendix: Derivation of Laplace transform $\tilde{n}(p)$

The appendix gives a brief summary on the solution of the diffusion and rate equations (2, 3) for cylindrical precipitates resulting in the Laplace transform $\tilde{n}(p)$ [Eq. (6)] (for spherical precipitates see Ref. [6]). The time dependence of equations (2) and (3) is solved by means of Laplace transformation ($\rho_{m/p/t}(r,t) \to \tilde{\rho}_{m/p/t}(r,p)$) yielding the modified Bessel differential equation for the r-dependence of $\tilde{\rho}_{m/p}(r,p)$. Taking into account the initial conditions, the solutions of eq. (2) and (3) read

$$\tilde{\rho}_{m/p}(r,p) = A\,I_0(\gamma r) + B\,K_0(\gamma r) + \frac{\rho_{m/p}(0)}{\tau_{f/p}^{-1} + p}\,,\quad \tilde{\rho}_t^{(m)} = \frac{\alpha\tilde{\rho}_m(r_0,p)}{\tau_t^{-1} + p}\,,\quad \tilde{\rho}_t^{(p)} = \frac{\beta\tilde{\rho}_p(r_0,p)}{\tau_t^{-1} + p} \tag{26}$$

with $\gamma^2 = \gamma^2(p) = (\tau_{f/p}^{-1} + p)/D$ and the modified Bessel functions I_j, K_j [7]. The coefficients A and B as determined by the boundary conditions [Eq. (4), eq. (5)] read for the inner (p) and outer part (m):

$$A = \frac{-\beta\rho_p(0)}{\tau_p^{-1} + p}\,\frac{1}{D\gamma I_1(\gamma r_0) + \alpha I_1(\gamma r_0)}\,, B = 0 \text{ and }\quad A = \frac{\alpha\rho_m(0)}{\tau_f^{-1} + p}\,\frac{K_1(\gamma R)}{D\gamma\Lambda_1 - \alpha\Lambda_0}\,, B = \frac{\alpha\rho_m(0)}{\tau_f^{-1} + p}\,\frac{I_1(\gamma R)}{D\gamma\Lambda_1 - \alpha\Lambda_0} \tag{27}$$

respectively, with $\Lambda_{0,1}$ according to eq. (7). From the densities $\tilde{\rho}_{m/p}(r,p)$, $\tilde{\rho}_t^{(m,p)}$ [Eq. (26)] follows the Laplace transform $\tilde{n}(p)$ of the total probability $n(t)$ that a e^+ implanted at $t = 0$ has not yet been annihilated at time t. This is obtained by integration over the cylindrical volume of the precipitate and over the hollow-cylindrical matrix. For the above mentioned initial condition ($\rho_m(0) = \rho_p(0)$) $\tilde{n}(p)$ reads:

$$\tilde{n}(p) = \frac{1}{\pi R^2 \rho_m(0)} \left\{ \int_0^{r_0} 2\pi r \tilde{\rho}_p(r,p)\mathrm{d}r + \int_{r_0}^{R} 2\pi r \tilde{\rho}_m(r,p)\mathrm{d}r + 2\pi r_0\Big(\tilde{\rho}_t^{(m)}(p) + \tilde{\rho}_t^{(p)}(p)\Big) \right\} \tag{28}$$

which after solving the integral results in eq. (6).

REFERENCES

[1]   A. Dupasquier, R. Romero, and A. Somoza, Phys. Rev. B **48**, p. 9235 (1993).
[2]   R. Würschum and A. Seeger, Phil. Mag. A **73**, p. 1489 (1996).
[3]   J. Dryzek, A. Czapla, and E. Kusior, J. Phys. Condens. Matter **10**, p. 10827 (1998).
[4]   J. Dryzek, Acta Physica Polonica A **95**, 539 (1999).
[5]   B. Oberdorfer and R. Würschum, Phys. Rev. B. **79**, p. 184103 (2009).
[6]   R. Würschum, L. Resch, and G. Klinser, Phys. Rev. B. **97**, p. 224108 (2018).
[7]   F. W. Olver, *NIST Handbook of Mathematical Functions* (Cambridge University Press, 2010).

Addendum

The herewith presented solutions of the diffusion-reaction model for positron trapping and annihilation at interfaces between the matrix and precipitates can be applied for a comparison to the experimental results obtained for the positron lifetime in the Al–Mg–Si alloy AW 6060 in dependence of the artificial aging time (see section 4.1.1, ref. [8]). The intensity of the trap component for positron trapping at interfaces between spherical precipitates and the matrix is given by equation (19) in section 4.3.2. In this case only diffusion from outside the precipitate into the interface is taken into account. Equation (19) can be evaluated assuming spherical precipitates with a radius r_0 of 3 nm. For the parameters τ_t and τ_f (which are the positron lifetime components corresponding to annihilation in the trapped state and in the free state, respectively) the experimentally observed values (see section 4.1.1) are applied. For the diffusion coefficient D and the specific trapping rate α typical values of 10^{-4} m^{2}s^{-1} [31] and 3000 ms^{-1} [35], respectively are inserted. For this parameters, it can be found that more than 80% of positrons are trapped at precipitates for a precipitate concentration of $4 \cdot 10^{22}$ m^{-3} in the matrix. On the other hand, the positron lifetime data presented in section 4.1.1 showed that saturation trapping occurs after 100 s of artificial aging at 180°C. The number density of a comparable aging state (180°C, 10 min.) was determined to be also in the range of 10^{22} m^{-3} by atom probe tomography [65]. Hence, by the application of the presented diffusion-reaction model, it could be shown that the experimentally observed saturation trapping of positrons and the corresponding annihilation parameters agree with the results obtained by atom probe tomography.

5 | Summary and Discussion

In this thesis specific problems concerning fundamental processes related to atomic defects in structurally complex metallic materials could be solved by applying experimental positron annihilation techniques. Theoretical calculations were made extending the application of the diffusion-reaction model for positron trapping and annihilation. The results are summarized in the following together with a brief discussion with most recent results (Refs. [76, 77]) published during the final writing stage of this thesis.

Artificial aging of the commercial Al–Mg–Si alloy AW 6060

In a first study, the fundamental details of the precipitation sequence occurring in the Al alloy AW 6060 were elucidated by *ex situ* positron annihilation lifetime spectroscopy measurements and *in situ* dilatometry measurements. More than 70 individual sample pairs were prepared in well-defined states of artificial aging (at temperatures of 180°C and 210°C) and kept at low temperatures during the measurement. According to the positron lifetime characteristics three temporal regimes in the sequence could be identified. In the initial time window, only the method of positron annihilation spectroscopy is sensitive enough to monitor the early stages of atomic clustering. From variations of a defect-related lifetime and the corresponding intensity, the annealing of quenched-in vacancies, the dissolution of natural aging clusters and the formation of artificial aging clusters were observed. After longer aging times, in a second time window, clusters evolved into β'' precipitates, as monitored by changes in

hardness and length change of the sample. In this region, the defect-related positron lifetime component clarified that pre-β" and β" precipitates show a similar structure with regard to their defect-related free volume. In a third timespan, an increasing fraction of semi-coherent β' precipitates in the Al matrix is monitored by an increase of the defect-related lifetime component and a decrease of the length change. By comparison of the results for the two different artificial aging temperatures (180°C and 210°C), it was further established that for higher aging temperatures, the whole precipitation sequence proceeds faster, clusters and precipitates evolve in parallel to each other and certain stages in the process are skipped.

For a further characterization of the clusters and precipitates occurring during artificial aging of the same commercial Al alloy, temperature-dependent positron annihilation lifetime spectroscopy measurements have been performed. These measurements showed that, during the course of artificial aging solute clusters act as shallow traps with weak positron binding energies in the early stages of aging (1000 s) while the positron binding energy of β" precipitates appearing later (2 hrs.) in the precipitation sequence is higher, and they act as deep positron traps.

In a very recent positron annihilation lifetime study published in June 2020, the artificial aging of a lean Al–Mg-Si alloy, with a composition similar to the AW 6060 alloy, was investigated [77]. In this recent study, the trend of the mean positron lifetime during artificial aging and the interpretation of these variations are widely consistent with the measurements and the corresponding interpretation stated in this thesis.

Within the framework of this thesis, the positron annihilation lifetime spectroscopy results were compared to *in situ* measurements of the Doppler broadening S-parameter during aging at 180°C and 210°C. The S-parameter, similar to the mean positron lifetime, increases if an increasing fraction of positrons annihilates in open volume defects. However, due to the application of *in situ* measurements at high temperatures the trapping behaviour of positrons is different than for measurements at low temperatures, as they were applied for the *ex situ* positron annihilation lifetime measurements. Therefore, only in the case of the *in situ* measurements of the S-parameter a strong variation upon the formation of β" precip-

itates could be observed. It was concluded that this can be attributed either to a fraction of remanent vacancies which anneal out during the formation of the β" phase, or to a variation of the Mg and Si content upon pre-β" to β" transformation. Additionally, the S-parameter in dependence of the temperature could be monitored during *in situ* solution heat treatment of an overaged sample. In this case the S-parameter showed a decrease assigned to the dissolution of precipitates and a subsequent increase assigned to the thermal induced generation of vacancies. These results demonstrate that for a comprehensive understanding of complex defect processes only a combination of *ex situ* laboratory experiments with *in situ* high intensity positron beam experiments can yield new insights.

In another recently published paper [76] (April 2020), again, a very similar trend for the positron lifetime in dependence of the artificial aging time has been measured for an excess-Si Al–Mg–Si alloy. Based on these results, the authors suggested that a high concentration of vacancies is induced upon the formation of the β" phase, which would not be in accordance with the results presented within this thesis [9] and within ref. [77]. However, this interpretation is based on the assumption that a fairly low positron lifetime value of 227 ps is attributed to annihilation of positrons in Al vacancies. This assumption seems doubtful if compared to established literature values for positron annihilations in Al vacancies ranging from 246 ps to 260 ps [96, 104, 105]. These two recent publications also demonstrate that defect characterization during the precipitation process in Al–Mg–Si alloy is a current hot topic in materials physics.

Diffusion-reaction model for the trapping and annihilation of positrons at extended defects

The exact solution of a diffusion-reaction model for the trapping and annihilation of positrons at extended defects including competitive rate-limited trapping at vacancy-type point defects is presented in this thesis. This model was further extended and solved for the case of positron trapping and annihilation at interfaces between the matrix and cylindrical or spherical precipitates. For both cases closed-form expressions were obtained for the mean

positron lifetime and the intensity of the positron lifetime component associated with the defect-trapped state. These closed-form expressions were applied for a comparison to the experimental results obtained for the positron lifetime in the Al–Mg–Si alloy AW 6060 in dependence of the artificial aging time. It was calculated that for a concentration of precipitates of $4 \cdot 10^{22}$ more than 80% of positrons are trapped at precipitates. From the experimentally obtained positron lifetime data it was found that saturation trapping of positrons at precipitates occurs for artificial aging times longer than 100 s at temperatures of 180°C. After a comparable aging step (10 min, 180°C) the number density of precipitates was determined to be also in the range of 10^{22} by atom probe tomography [65]. Hence, by utilization of the diffusion-reaction model it could be determined that the positron lifetime data is in good agreement with the values obtained by atom probe tomography, which shows the high application relevance of this model.

Thermally induced vacancies in concentrated solid-solution alloys with fcc crystal structure

Positron annihilation lifetime spectroscopy measurements were performed to quantify for the first time the concentration of thermal vacancies in the newly established material class of fcc concentrated-solid solution alloys after quenching from high temperatures close to their onset of melting. For a set of similar alloys with the same fcc structure a decreasing trend of the mean positron lifetime and, in connection to that, also a decreasing trend of the concentration of quenched-in vacancies with increasing entropy of mixing was observed. While alloys with three constituents in non-equimolar fractions (CrFeNi) showed a vacancy concentration in the range of 10^{-5}, the studied alloys with four (CoCrFeNi) and five components (CoCrFeMnNi, AlCoCrFeNi) did not show a vacancy-specific positron lifetime. It can be concluded that only a concentration of vacancies smaller than 10^{-6} can be thermally generated and quenched-in. Hence, the vacancy concentration is either vanishingly small at temperatures close to the onset of melting or the generated vacancies are inherently unstable. In the latter case, a unreasonably small migration enthalpy for the self-diffusion process must be assumed, which

is why the former explanation seems to be more promising. These fundamental results might be the basis for explanation of some of the so far unresolved issues in this new class of alloys as for example their superior radiation tolerance.

List of Peer Reviewed Publications

done in the framework of this thesis

Resch, L.*; Klinser, G.*; Hengge, E.; Enzinger, R.; Luckabauer, M.; Sprengel, W.; Würschum, R.
* both authors contributed equally to this work.
Precipitation processes in Al–Mg–Si extending down to initial clustering revealed by the complementary techniques of positron lifetime spectroscopy and dilatometry
Springer, Journal of Materials Science, Volume 53, Issue 20, 2018, Pages 14657–14665

Resch, L.; Klinser, G.; Sprengel, W.; Würschum, R.
Identification of different positron trapping sites during artificial aging of a commercial light weight alloy
AIP Conference Proceedings, Volume 2182, Issue 1, 2019, Pages 1197-1201

Resch, L.; Gigl, T.; Klinser, G.; Hugenschmidt, C.; Sprengel, W.; Würschum, R.
In situ monitoring of artificial aging and solution heat treatment of a commercial Al–Mg–Si alloy with a high-intensity positron beam
IOP Publishing, Journal of Physics: Condensed Matter, Volume 32, Issue 8, 2019, Page 085705

Resch, L.; Luckabauer, M.; Helthuis, N.; Enzinger, R.; Okamoto, N.L.; Ichitsubo, T.; Sprengel, W.; Würschum, R.
Search for vacancies in concentrated solid-solution alloys with fcc crystal structure
Physical Review Materials, Rapid Communications, Volume 4, Issue 6, 2020, Page 060601

Würschum R.; **Resch, L.**; Klinser, G.
Diffusion-reaction model for positron trapping and annihilation at spherical extended defects and in precipitate-matrix composites
APS, Physical Review B, Volume 97, Issue 22, 2018, Page 224108

Würschum R.; **Resch, L.**; Klinser, G.
Positron trapping and annihilation at interfaces between matrix and cylindrical or spherical precipitates modeled by diffusion-reaction theory
AIP Conference Proceedings, Volume 2182, Issue 1, 2019, Pages 050010

Solodin S.; **Resch, L.**; Klinser, G.; Sprengel, W.; Nykoniuk, Ye.; Zakharuk, Z.; Panchuk, O.; Fochuk, P.; James, R.B.
Study of point defects in CdTe:Mn crystals by electrical measurements supported by positron lifetime spectroscopy IEEE Nuclear Science Symposium and Medical Imaging Conference Proceedings, 2018, Pages 1-5

Gadermeier, B.; **Resch, L.**; Pickup, D.; Hanghofer, I.; Hanzu, I.; Heitjans, P.; Sprengel, W.; Würschum, R.; Chadwick, A.; Wilkening, M.
Influence of defects on ionic transport in $LiTaO_3$ – a study using EXAFS and positron annihilation lifetime spectroscopy
Solid State Ionics, Volume 352, 2020, Page 115355

Bibliography

[1] P. Hautojärvi, A. Dupasquier, and M. J. Manninen. *Topics in Current Physics: Positrons in solids*, volume 12. Springer, 1979.

[2] G. A. Edwards, K. Stiller, G. L. Dunlop, and M. J. Couper. The precipitation sequence in Al–Mg–Si alloys. *Acta Mater.*, 46(11):3893–3904, 1998.

[3] A. Dupasquier, G. Kögel, and A. Somoza. Studies of light alloys by positron annihilation techniques. *Acta Mater.*, 52(16):4707–4726, 2004.

[4] G. Dlubek. Positron studies of decomposition phenomena in Al alloys. In *Mater. Sci. Forum*, volume 13, pages 11–32. Trans. Tech. Publ., 1987.

[5] M. J. Puska, P. Lanki, and R. M. Nieminen. Positron affinities for elemental metals. *J. Phys.: Condens. Matter*, 1(35):6081, 1989.

[6] J. Banhart, M. D. H Lay, C. S. T. Chang, and A. J. Hill. Kinetics of natural aging in Al–Mg–Si alloys studied by positron annihilation lifetime spectroscopy. *Phys. Rev. B*, 83(1):014101, 2011.

[7] M. Liu, J. Čížek, C. S. T. Chang, and J. Banhart. Early stages of solute clustering in an Al–Mg–Si alloy. *Acta Mater.*, 91:355–364, 2015.

[8] L. Resch, G. Klinser, E. Hengge, R. Enzinger, M. Luckabauer, W. Sprengel, and R. Würschum. Precipitation processes in Al–Mg–Si extending down to initial clustering revealed by the complementary techniques of positron lifetime spectroscopy and dilatometry. *J. Mater. Sci.*, 53(20):14657–14665, 2018.

[9] L. Resch, G. Klinser, W. Sprengel, and R. Würschum. Identification of different positron trapping sites during artificial aging of a commercial light weight alloy. In *AIP Conf. Proc.*, volume 2182, page 050012. AIP Publishing LLC, 2019.

[10] L. Resch, T. Gigl, G. Klinser, Ch. Hugenschmidt, W. Sprengel, and R. Würschum. In situ monitoring of artificial aging and solution heat treatment of a commercial Al–Mg–Si alloy with a high intensity positron beam. *J. Phys.: Condens. Matter*, 32(8):085705, 2019.

[11] R. Würschum, L. Resch, and G. Klinser. Diffusion-reaction model for positron trapping and annihilation at spherical extended defects and in precipitate-matrix composites. *Phys. Rev. B*, 97(22):224108, 2018.

[12] R. Würschum, L. Resch, and G. Klinser. Positron trapping and annihilation at interfaces between matrix and cylindrical or spherical precipitates modeled by diffusion-reaction theory. In *AIP Conf. Proc.*, volume 2182, page 050010. AIP Publishing LLC, 2019.

[13] Z. Li, K. G. Pradeep, Y. Deng, D. Raabe, and C. C. Tasan. Metastable high-entropy dual-phase alloys overcome the strength–ductility trade-off. *Nature*, 534(7606):227–230, 2016.

[14] C.-Y. Hsu, C.-C. Juan, W.-R. Wang, T.-S. Sheu, J.-W. Yeh, and S.-K. Chen. On the superior hot hardness and softening resistance of $AlCoCr_xFeMo_{0.5}Ni$ high-entropy alloys. *Mater. Sci. Eng., A*, 528(10-11):3581–3588, 2011.

[15] C. Lu, L. Niu, N. Chen, K. Jin, T. Yang, P. Xiu, Y. Zhang, F. Gao, H. Bei, S. Shi, et al. Enhancing radiation tolerance by controlling defect mobility and migration pathways in multicomponent single-phase alloys. *Nat. Commun.*, 7(1):1–8, 2016.

[16] F. Granberg, K. Nordlund, M. W. Ullah, K. Jin, C. Lu, H. Bei, L. M. Wang, F. Djurabekova, W. J. Weber, and Y. Zhang. Mechanism of radiation damage reduction in equiatomic multicomponent single phase alloys. *Phys. Rev. Lett.*, 116(13):135504, 2016.

[17] L. Resch, M. Luckabauer, N. Helthuis, N.L. Okamoto, T. Ichitsubo, R. Enzinger, W. Sprengel, and R. Würschum. Search for vacancies in concentrated solid-solution alloys with fcc crystal structure. *Phys. Rev. Mater.*, 4(6):060601, 2020.

[18] P. A. M. Dirac. The quantum theory of the electron. *Proc. R. Soc. London, Ser. A, Containing Papers of a Mathematical and Physical Character*, 117(778):610–624, 1928.

[19] C. D. Anderson. The apparent existence of easily deflectable positives. *Science*, 76(1967):238–239, 1932.

[20] A. Perkins and J. P. Carbotte. Effect of the positron-phonon interaction on positron motion. *Phys. Rev. B*, 1(1):101, 1970.

[21] W. Brandt and R. Paulin. Positron implantation-profile effects in solids. *Phys. rev. B*, 15(5):2511, 1977.

[22] M. J. Puska and R. M. Nieminen. Theory of positrons in solids and on solid surfaces. *Rev. Mod. Phys.*, 66(3):841, 1994.

[23] R. M. Nieminen and M. J. Manninen. Positrons in imperfect solids: theory. In *Positrons in solids*, pages 145–195. Springer, 1979.

[24] R. N. West. Positron studies of condensed matter. *Adv. Phys.*, 22(3):263–383, 1973.

[25] H.-E. Schaefer. Investigation of thermal equilibrium vacancies in metals by positron annihilation. *Phys. Status Solidi A*, 102(1):47–65, 1987.

[26] M. Bertolaccini and A. Dupasquier. Positron annihilation in solid and molten alkali chlorides. *Phys. Rev. B*, 1(7):2896, 1970.

[27] W. Brandt and R. Paulin. Positron diffusion in solids. *Phys. Rev. B*, 5(7):2430, 1972.

[28] W. Frank and A. Seeger. Theoretical foundation and extension of the trapping model. *Applied Physics*, 3(1):61–66, 1974.

[29] R. Krause-Rehberg and H. S. Leipner. *Positron annihilation in semiconductors: defect studies*, volume 127. Springer Science & Business Media, 1999.

[30] H.-E. Schaefer, R. Gugelmeier, M. Schmolz, and A. Seeger. Microstructural characterization of materials by non-microscopical techniques edited by N. Hessel Andersen et al., 1984.

[31] E. Soininen, H. Huomo, P. A. Huttunen, J. Mäkinen, A. Vehanen, and P. Hautojärvi. Temperature dependence of positron diffusion in cubic metals. *Phys. Rev. B*, 41(10):6227, 1990.

[32] R. Paulin, R. Ripon, and W. Brandt. Diffusion constant and surface states of positrons in metals. *Appl. Phys.*, 4(4):343–347, 1974.

[33] R. M. Nieminen, J. Laakkonen, P. Hautojärvi, and A. Vehanen. Temperature dependence of positron trapping at voids in metals. *Phys. Rev. B*, 19(3):1397, 1979.

[34] D. T. Britton. Time-dependent diffusion and annihilation of positrons implanted in a semi-infinite medium. *J. Phys.: Condens. Matter*, 3(6):681, 1991.

[35] A. Dupasquier, R. Romero, and A. Somoza. Positron trapping at grain boundaries. *Phys. Rev. B*, 48(13):9235, 1993.

[36] R. Würschum and A. Seeger. Diffusion-reaction model for the trapping of positrons in grain boundaries. *Philos. Mag. A*, 73(5):1489–1501, 1996.

[37] G. Kögel. Positron diffusion in solids and the reconstruction of inhomogeneous defect distributions from lifetime measurements. *Appl. Phys. A*, 63(3):227–235, 1996.

[38] J. Dryzek. Positron trapping model in fine grained sample. *Acta Phys. Pol. A*, 95(4):539–545, 1999.

[39] J. Čížek, I. Procházka, M. Cieslar, R. Kužel, J. Kuriplach, F. Chmelík, I. Stulíková, F. Bečvář, O. Melikhova, and R. K. Islamgaliev. Thermal stability of ultrafine grained copper. *Phys. Rev. B*, 65(9):094106, 2002.

[40] B. Oberdorfer and R. Würschum. Positron trapping model for point defects and grain boundaries in polycrystalline materials. *Phys. Rev. B*, 79(18):184103, 2009.

[41] J. Dryzek and A. Czapla. The trapping model for positrons diffusing inside the grain of arbitrary shape. *J. Phys.: Condens. Matter*, 10(31):L547, 1998.

[42] O. H. Duparc. Alfred Wilm and the beginnings of Duralumin. *Zeitschrift für Metallkunde*, 96(4):398–404, 2005.

[43] W. S. Miller, L. Zhuang, J. Bottema, A. J. Wittebrood, P. De Smet, A. Haszler, and A. J. M. S. Vieregge. Recent development in aluminium alloys for the automotive industry. *Mater. Sci. Eng., A*, 280(1):37–49, 2000.

[44] X. H. Zhang, G. C. Su, C. W. Ju, W. C. Wang, and W. L. Yan. Effect of modification treatment on the microstructure and mechanical properties of Al–0.35% Mg–7.0% Si cast alloy. *Mater. Des.*, 31(9):4408–4413, 2010.

[45] F. Ostermann. *Anwendungstechnologie Aluminium*. Springer-Verlag, 2015.

[46] J. Hirsch, B. Skrotzki, and G. Gottstein. *Aluminium alloys: the physical and mechanical properties*, volume 1. John Wiley & Sons, 2008.

[47] G. Gottstein. *Physikalische Grundlagen der Materialkunde*. Springer-Verlag, 2007.

[48] M. A. Van Huis, J. H. Chen, M. H. F. Sluiter, and H. W. Zandbergen. Phase stability and structural features of matrix-embedded hardening precipitates in Al–Mg–Si alloys in the early stages of evolution. *Acta Mater.*, 55(6):2183–2199, 2007.

[49] M. Murayama, K. Hono, M. Saga, and M. Kikuchi. Atom probe studies on the early stages of precipitation in Al–Mg–Si alloys. *Materials Sci. Eng., A*, 250(1):127–132, 1998.

[50] V. Fallah, B. Langelier, N. Ofori-Opoku, B. Raeisinia, N. Provatas, and S. Esmaeili. Cluster evolution mechanisms during aging in Al–Mg–Si alloys. *Acta Mater.*, 103:290–300, 2016.

[51] C. D. Marioara, S. J. Andersen, J. Jansen, and H. W. Zandbergen. Atomic model for GP-zones in a 6082 Al–Mg–Si system. *Acta Mater.*, 49(2):321–328, 2001.

[52] M. A. Van Huis, J. H. Chen, H. W. Zandbergen, and M. H. F. Sluiter. Phase stability and structural relations of nanometer-sized, matrix-embedded precipitate phases in Al–Mg–Si alloys in the late stages of evolution. *Acta Mater.*, 54(11):2945–2955, 2006.

[53] S.J. Andersen, H.W. Zandbergen, J. Jansen, C. Traeholt, U. Tundal, and O. Reiso. The crystal structure of the β'' phase in Al–Mg–Si alloys. *Acta Mater.*, 46(9):3283–3298, 1998.

[54] K. Matsuda, T. Naoi, K. Fujii, S. Ikeno, Y. Uetani, T. Sato, and A. Kamio. Crystal structure of the β'' phase in an Al-1.0mass%Mg$_2$Si-0.4mass%Si alloy. *Mater Sci. Eng., A*, 1999.

[55] H. S. Hasting, A. G. Frøseth, S. J. Andersen, R. Vissers, J. C. Walmsley, C. D. Marioara, F. Danoix, W. Lefebvre, and R. Holmestad. Composition of β'' precipitates in Al–Mg–Si alloys by atom probe tomography and first principles calculations. *J. Appl. Phys.*, 106(12):123527, 2009.

[56] P. H. Ninive, A. Strandlie, S. Gulbrandsen-Dahl, W. Lefebvre, C. D. Marioara, S. J. Andersen, J. Friis, R. Holmestad, and O. M. Løvvik. Detailed atomistic insight into the β" phase in Al–Mg–Si alloys. *Acta Mater.*, 69:126–134, 2014.

[57] F. J. H. Ehlers, S. Dumoulin, and R. Holmestad. 3d modelling of β" in Al–Mg–Si: Towards an atomistic level ab initio based examination of a full precipitate enclosed in a host lattice. *Comput. Mater. Sci.*, 91:200–210, 2014.

[58] M. H. Jacobs. The structure of the metastable precipitates formed during ageing of an Al–Mg–Si alloy. *Philos. Mag.*, 26(1):1–13, 1972.

[59] K. Matsuda, Y. Sakaguchi, Y. Miyata, Y. Uetani, T. Sato, A. Kamio, and S. Ikeno. Precipitation sequence of various kinds of metastable phases in Al-1.0 mass% Mg2Si-0.4 mass% Si alloy. *J. Mater. Sci.*, 35(1):179–189, 2000.

[60] S. J. Andersen, C. D. Marioara, A. Frøseth, R. Vissers, and H. W. Zandbergen. Crystal structure of the orthorhombic u2-Al4Mg4Si4 precipitate in the Al–Mg–Si alloy system and its relation to the β' and β" phases. *Mater. Sci. Eng., A*, 390(1-2):127–138, 2005.

[61] A. G. Frøseth, R. Høier, P. M. Derlet, S. J. Andersen, and C. D. Marioara. Bonding in MgSi and Al–Mg–Si compounds relevant to Al–Mg–Si alloys. *Phys. Rev. B*, 67(22):224106, 2003.

[62] R. Vissers, M. A. van Huis, J. Jansen, H. W. Zandbergen, C. D. Marioara, and S. J. Andersen. The crystal structure of the β' phase in al–mg–si alloys. *Acta Mater.*, 55(11):3815–3823, 2007.

[63] A. H. Geisler and J. K. Hill. Analyses and interpretations of x-ray diffraction effects in patterns of aged alloys. *Acta Crystallogr.*, 1(5):238–252, 1948.

[64] J. Banhart, C. S. T. Chang, Z. Liang, N. Wanderka, M. D. H. Lay, and A. J. Hill. Natural aging in Al–Mg–Si alloys–a process of unexpected complexity. *Adv. Eng. Mater.*, 12(7):559–571, 2010.

[65] M. W. Zandbergen, Q. Xu, A. Cerezo, and G. D. W. Smith. Study of precipitation in Al–Mg–Si alloys by atom probe tomography i. microstructural changes as a function of ageing temperature. *Acta Mater.*, 101:136–148, 2015.

[66] M. Werinos, H. Antrekowitsch, T. Ebner, R. Prillhofer, P. J. Uggowitzer, and S. Pogatscher. Hardening of Al–Mg–Si alloys: Effect of trace elements and prolonged natural aging. *Mater. Des.*, 107:257–268, 2016.

[67] M. Luckabauer, E. Hengge, G. Klinser, W. Sprengel, and R. Würschum. In situ real-time monitoring of aging processes in an aluminum alloy by high-precision dilatometry. In *Magnesium Technology 2017*, pages 669–674. Springer, 2017.

[68] M. Murayama and K. Hono. Pre-precipitate clusters and precipitation processes in Al–Mg–Si alloys. *Acta Mater.*, 47(5):1537–1548, 1999.

[69] S. Pogatscher, H. Antrekowitsch, H. Leitner, T. Ebner, and P. J. Uggowitzer. Mechanisms controlling the artificial aging of Al–Mg–Si alloys. *Acta Mater.*, 59(9):3352–3363, 2011.

[70] T. E. M. Staab, R. Krause-Rehberg, U. Hornauer, and E. Zschech. Study of artificial aging in AlMgSi (6061) and AlMgSiCu (6013) alloys by positron annihilation. *J. Mater. Sci.*, 41(4):1059–1066, 2006.

[71] B. Klobes, T. E. M. Staab, M. Haaks, K. Maier, and I. Wieler. The role of quenched-in vacancies for the decomposition of aluminium alloys. *Phys. Status Solidi RRL*, 2(5):224–226, 2008.

[72] J. Banhart, M. Liu, Y. Yong, Z. Liang, C. S. T. Chang, M. Elsayed, and M. D. H. Lay. Study of ageing in Al–Mg–Si alloys by positron annihilation spectroscopy. *Physica B*, 407(14):2689–2696, 2012.

[73] B. Klobes, K. Maier, and T. E. M. Staab. Early stage ageing effects and shallow positron traps in Al–Mg–Si alloys. *Philos. Mag.*, 95(13):1414–1424, 2015.

[74] B. Klobes, B. Korff, O. Balarisi, P. Eich, M. Haaks, K. Maier, R. Sottong, S.-M. Hühne, W. Mader, and T. E. M. Staab. Probing the defect state of individual precipitates grown in an Al–Mg–Si alloy. *Phys. Rev. B*, 82(5):054113, 2010.

[75] M. Liu, J. Čížek, C. S. T. Chang, and J. Banhart. A positron study of early clustering in Al–Mg–Si alloys. In *Mater. Sci. Forum*, volume 794, pages 33–38. Trans Tech Publ, 2014.

[76] K. Inoue, K. Takata, K. Kazumi, and Y. Shirai. High concentration of vacancies induced by β" phase formation in Al–Mg–Si alloys. *Philos. Mag. Lett.*, 100(6):260–270, 2020.

[77] M. Madanat, M. Liu, X. Zhang, Q. Guo, J. Čížek, and J. Banhart. Co-evolution of vacancies and solute clusters during artificial ageing of Al–Mg–Si alloys. *Phys. Rev. Mater.*, 4(6):063608, 2020.

[78] J.-W. Yeh, S.-K. Chen, S.-J. Lin, J.-Y. Gan, T.-S. Chin, T.-T. Shun, C.-H. Tsau, and S.-Y. Chang. Nanostructured high-entropy alloys with multiple principal elements: novel alloy design concepts and outcomes. *Adv. Eng. Mater.*, 6(5):299–303, 2004.

[79] B. Cantor, I. T. H. Chang, P. Knight, and A. J. B. Vincent. Microstructural development in equiatomic multicomponent alloys. *Mater. Sci. Eng., A*, 375:213–218, 2004.

[80] M. C. Gao, J.-W. Yeh, P. K. Liaw, Y. Zhang, et al. *High-entropy alloys*. Springer, 2016.

[81] F. Otto, Y. Yang, H. Bei, and E. P. George. Relative effects of enthalpy and entropy on the phase stability of equiatomic high-entropy alloys. *Acta Mater.*, 61(7):2628–2638, 2013.

[82] G. Sheng and C. T. Liu. Phase stability in high entropy alloys: formation of solid-solution phase or amorphous phase. *Progr. Nat. Sci.-Mater.*, 21(6):433–446, 2011.

[83] Y. F. Ye, Q. Wang, J. Lu, C. T. Liu, and Y. Yang. Design of high entropy alloys: A single-parameter thermodynamic rule. *Scr. Mater.*, 104:53–55, 2015.

[84] M. Vaidya, K. G. Pradeep, B. S. Murty, G. Wilde, and S. V. Divinski. Bulk tracer diffusion in CoCrFeNi and CoCrFeMnNi high entropy alloys. *Acta Mater.*, 146:211–224, 2018.

[85] S. Divinski, O. Lukianova, G. Wilde, A. Dash, N. Esakkiraja, and A. Paul. High-entropy alloys: Diffusion. *Encyclopedia of Materials: Science and Technology*, 2020.

[86] M.-H. Chuang, M.-H. Tsai, W.-R. Wang, S.-J. Lin, and J.-W. Yeh. Microstructure and wear behavior of $Al_xCo_{1.5}CrFeNi_{1.5}Ti_y$ high-entropy alloys. *Acta Mater.*, 59(16):6308–6317, 2011.

[87] J. J. Zhang, X. L. Yin, Y. Dong, Y. P. Lu, L. Jiang, T. M. Wang, and T. J. Li. Corrosion properties of $Al_xCoCrFeNiTi_{0.5}$ high entropy alloys in 0·5M H_2SO_4 aqueous solution. *Mater. Res. Innovations*, 18(sup4):S4–756, 2014.

[88] H.-E. Schaefer, R. Gugelmeier, M. Schmolz, and A. Seeger. Positron lifetime spectroscopy and trapping at vacancies in aluminium. In *Mater. Sci. Forum*, volume 15, pages 111–116. Trans Tech Publ, 1987.

[89] A. Somoza, M. P. Petkov, K. G. Lynn, and A. Dupasquier. Stability of vacancies during solute clustering in Al–Cu-based alloys. *Phys. Rev. B*, 65(9):094107, 2002.

[90] S. Abhaya, R. Rajaraman, S. Kalavathi, and G. Amarendra. Positron annihilation studies on fecrconi high entropy alloy. *J. Alloy Compd.*, 620:277–282, 2015.

[91] M. Elsayed, R. Krause-Rehberg, C. Eisenschmidt, N. Eißmann, and B. Kieback. Defect study in cocrfemnni high entropy alloy by positron annihilation lifetime spectroscopy. *Phys. Status Solidi A*, 215(11):1800036, 2018.

[92] K. Sugita, N. Matsuoka, M. Mizuno, and H. Araki. Vacancy formation enthalpy in CoCrFeMnNi high-entropy alloy. *Scr. Mater.*, 176:32–35, 2020.

[93] P. Kirkegaard, J. V. Olsen, and M. M. Eldrup. Palsfit3: a software package for analysing positron lifetime spectra. Technical report, Technical University of Denmark (DTU), 2017.

[94] N. Djourelov and M. Misheva. Source correction in positron annihilation lifetime spectroscopy. *J. Phys.: Condens. Matter*, 8(12):2081, 1996.

[95] S. McGuire and D. J. Keeble. Positron lifetimes of polycrystalline metals: A positron source correction study. *J. Appl. Phys.*, 100(10):103504, 2006.

[96] H.-E. Schaefer, R. Gugelmeier, M. Schmolz, and A. Seeger. Positron lifetime spectroscopy and trapping at vacancies in aluminium. In *Materials science forum*, volume 15, pages 111–116. Trans Tech Publ, 1987.

[97] P. Parz. *Vacancy-type and interface related defects in ultra fine grained alloys and oxides*. PhD thesis, Graz University of Technology, 2013.

[98] Ch. Hugenschmidt, B. Löwe, J. Mayer, C. Piochacz, P. Pikart, R. Repper, M. Stadlbauer, and K. Schreckenbach. Unprecedented intensity of a low-energy positron beam. *Nucl. Instrum. Methods Phys. Res., Sect. A*, 593(3):616–618, 2008.

[99] Ch. Hugenschmidt, H. Ceeh, T. Gigl, F. Lippert, C. Piochacz, M. Reiner, K. Schreckenbach, S. Vohburger, J. Weber, and S. Zimnik. Positron beam characteristics at NEPOMUC upgrade. In *J. Phys. Conf. Ser.*, volume 505, page 012029. IOP Publishing, 2014.

[100] Ch. Hugenschmidt. Positron beam experiments at NEPOMUC. *Nuclear Physics News*, 28(2):28–31, 2018.

[101] M. Reiner, P. Pikart, and Ch. Hugenschmidt. In-situ (C)DBS at high temperatures at the NEPOMUC positron beam line. In *J. Phys. Conf. Ser.*, volume 443, page 012071, 2013.

[102] T. Gigl, C. Piochacz, M. Reiner, and C. Hugenschmidt. Positronbeam for μm resolved coincident doppler broadening spectroscopy at NEPOMUC. In *J. Phys. Conf. Ser.*, volume 505, page 012032. IOP Publishing, 2014.

[103] E. Hengge. Real-time high-precision dilatometric study of nano-scale precipitation processes during isothermal age-hardening in en aw-6060 aluminium alloy. Master's thesis, Graz University of Technology, 2018.

[104] M. J. Puska and R. M. Nieminen. Defect spectroscopy with positrons: a general calculational method. *J. Phys. F: Met. Phys.*, 13(2):333, 1983.

[105] T. Korhonen, M. J. Puska, and R. M. Nieminen. First-principles calculation of positron annihilation characteristics at metal vacancies. *Phys. Rev. B*, 54(21):15016, 1996.

Acknowledgements

AFFIDAVIT

I declare that I have authored this thesis independently, that I have not used other than the declared sources/resources, and that I have explicitly indicated all material which has been quoted either literally or by content from the sources used. The text document uploaded to TUGRAZonline is identical to the present doctoral thesis.

Date, Signature